RIGA TECHNICAL UNIVERSITY

Adham Ahmed Awad Elsayed Elmenshawy

INVESTIGATION OF PERFORMANCE IMPROVEMENT OF GAS TURBINE ENGINE BY OPTIMIZED DESIGN OF BLADE TURBINE COOLING CHANNELS

Doctoral Thesis

RTU Press
Riga 2024

RIGA TECHNICAL UNIVERSITY

Faculty of Civil and Mechanical Engineering
Aeronautics, Space Engineering and Transport Institute

Adham Ahmed Awad Elsayed Elmenshawy

Doctoral Student of the Study Programme "Transport, Aviation Engineering"

INVESTIGATION OF PERFORMANCE IMPROVEMENT OF GAS TURBINE ENGINE BY OPTIMIZED DESIGN OF BLADE TURBINE COOLING CHANNELS

Doctoral Thesis

Scientific supervisor

Associate Professor Dr. sc. ing.
Ali Arshad

RTU Press
Riga 2024

Elmenshawy, A. Investigation of performance improvement of gas turbine engine by optimized design of blade turbine cooling channels. Doctoral Thesis. – Riga: RTU Press, 2024. – 145 p.

Published in accordance with the decision of the Promotion Council "RTU P–22" of 8 May, 2024, Minutes No. 04030-9.16.2/3.

DOCTORAL THESIS PROPOSED TO RIGA TECHNICAL UNIVERSITY FOR PROMOTION TO THE SCIENTIFIC DEGREE OF DOCTOR OF SCIENCE

To be granted the scientific degree of Doctor of Science (Ph. D.), the present Doctoral Thesis has been submitted for defence at the open meeting of RTU Promotion Council on August 30, 2024 at Zoom online meeting https://rtucloud1.zoom.us/j/94304241685.

OFFICIAL REVIEWERS

Dr. habil. sc. ing. Vitālijs Pavelko
Riga Technical University

Dr. sc. ing. Espen Oland
UiT The Arctic University of Norway, Norway

Dr. sc. ing. Iyad Alomar
Transport and Telecommunication Institute, Latvia

DECLARATION OF ACADEMIC INTEGRITY

I hereby declare that the Doctoral Thesis submitted for review to Riga Technical University for promotion to the scientific degree of Doctor of Science (Ph. D) is my own. I confirm that this Doctoral Thesis has not been submitted to any other university for promotion to a scientific degree.

Adham Ahmed Awad Elsayed Elmenshawy ……. (signature)

Date: ……

The Doctoral Thesis has been written in English. It consists of an Introduction, 4 chapters, Conclusions, 69 figures, 9 tables, and 2 appendices; the total number of pages is 145, including appendices. The Bibliography contains 106 titles.

ACKNOWLEDGEMENT

This work represents the culmination of my hard work and dedication. I would like to express my deepest gratitude to my supervisor, Prof. Ali Arshad, for his invaluable guidance and support throughout this journey. I extend my heartfelt thanks to Prof. Ilmārs Blumbergs for his support and help, and to the president of the commission, Prof. Pavelko, and all commission members for their insightful feedback and encouragement.

I am especially grateful to my dear friend, Prof. Iyad Alomar, whose unwavering support and assistance have been instrumental in the completion of this thesis.

This work is dedicated to my wife, who has endured and supported me through countless challenges. I also dedicate this achievement to my parents, my sister, and my brother, whose love and encouragement have been my constant source of strength.

ANOTĀCIJA

Šis doktora darbs koncentrējas uz kritisku izaicinājumu – gāzturbinu dzinēju turbīnas asmeņu dzesēšanu, kas darbības laikā tiek pakļauti ekstrēmām temperatūrām un termiskajām slodzēm. Galvenokārt šie asmeņi piedzīvo intensīvu siltumu degvielas sadegšanas dēļ dzinēja degšanas kamerā, nepieciešama efektīva dzesēšanas metode, lai novērstu pārkaršanu un bojājumus.Šī pētījuma galvenais aspekts bija dzesēšanas kanālu dizaina optimizācija šajos asmens. Kanāli, kas cirkulē dzesēšanas šķidrumu, ir būtiski, lai uzturētu asmeņu temperatūru drošos robežās. Pētījums uzsver dizaina apsvērumus efektīvai dzesēšanai: nepieciešamās plūsmas ātruma nodrošināšana ar pieņemamām spiediena kritumiem, kanālu ģeometrijas optimizācija efektīvai siltuma pārnesē, minimizējot profila zudumus.Tika ņemtas vērā arī turbīnas asmeņu materiālu īpašības, ieskaitot siltumvadītspēju, siltumietilpību un kušanas punktu dzesēšanas kanālu dizaina fāzē.Veikta plaša statistiskā analīze CF6 dzinējiem, kas uzstādīti B747 lidaparātos. Tas ietvēra dzinēju bojājumu, veiktspējas testu un boroskopa inspekcijas (BI) ziņojumu izpēti dažādos ekspluatācijas apstākļos. Pētījums nodrošināja detalizētu Izplūdes Gāzu Temperatūras (EGT) robežas un citu dzinēju parametru izpēti, sniedzot ieskatus par dzinēju degradāciju un veiktspējas zudumu laika gaitā. Tas sniedza svarīgu izpratni par dzesēšanas kanālu dizainu asmeņu profilam.Nākamajā solī, izmantojot datorizētas un analītiskas metodoloģijas, pētījumā tika novērtēta bāzes modeļa (sākotnējā) NASA 3CX turbīnas asmens dzesēšanas veiktspēja. Šajā analīzē tika izmantots SolidWorks un ANSYS FLUENT, atbalstīti ar MATLAB algoritmu datu salīdzināšanai ar atsauces eksperimentālajiem datiem. Pētījumā tika salīdzinātas dažādas dzesēšanas kanālu konfigurācijas, ieskaitot U-veida, Net-veida un Strūklas ietekmes tipa kanālus, īpaši izstrādātus doktora pētījumam. Projektētie kanāli atklāja nozīmīgas atšķirības vilces spēkos un termiskajā veiktspējā, pamatojoties uz to dizaina īpašībām.Secinājumi demonstrē, ka kanālu ģeometrija, konkrēti hidrauliskais diametrs, būtiski ietekmē dzesēšanas efektivitāti. Doktora pētījums atklāj, ka strūklas ietekmes tipa dzesēšanas kanāli parādīja ievērojamu uzlabojumu dzesēšanas efektivitātē turbīnas asmens īpaši aizmugurējā malā, uzsverot kanālu dizaina nozīmi turbīnas asmens termiskās veiktspējas uzlabošanā. Šis pētījums piedāvā būtiskas atziņas par turbīnas asmens dzesēšanu, ar sekām uz gāzturbinu dzinēju ekspluatācijas efektivitātes un kalpošanas laika uzlabošanu.

Promocijas darbs ir sastādīts angļu valodā, tajā ir 145 lappuses, 69 attēls, 7 tabulas, atsauces uz līdz 106 literatūras avotiem.

ABSTRACT

This doctoral work focuses on the critical challenge of cooling turbine blades in gas turbine engines, a component exposed to extreme temperatures and thermal stresses during operation. Predominantly, these blades experience intense heat due to fuel combustion in the engine's combustion chamber, necessitating efficient cooling methods to prevent overheating and failure. A key aspect of this research was the optimization of cooling channel designs within these blades. The channels, which circulate coolant fluid, are essential for maintaining blade temperatures within safe limits. The study emphasizes the design considerations crucial for effective cooling: accommodating the required flow rate with acceptable pressure drops, optimizing channel geometry for efficient heat transfer while minimizing profile losses. Material properties of the turbine blades, including thermal conductivity, heat capacity, and melting point, were also considered in the design phase of the cooling channels. An extensive statistical analysis was conducted on CF6 engines installed in B747 aircraft. This involved examining engine failures, performance tests, and Borescope Inspections (BI) reports under various operational conditions. The study provided a detailed examination of the Exhaust Gas Temperature (EGT) margin and other engine parameters, offering insights into engine degradation and performance loss over time. This provided an important understanding to design cooling channels for the blade profile.

In the next step, by employing computational and analytical methodologies, the study evaluated the cooling performance of the base model (original) NASA's 3CX turbine blade. SolidWorks and ANSYS FLUENT were used in this analysis, supported by a MATLAB algorithm for data comparison with the reference experimental data. The research compared different cooling channel configurations, including U-bend, Net-shape, and Jet impingement types, especially designed for doctoral research. The designed channels revealed significant differences in drag forces and thermal performance based on their design features. The findings demonstrate that channel geometry, specifically the hydraulic diameter, significantly influences cooling efficiency. The doctoral research reveals that jet impingement type cooling channels showcased a notable improvement in cooling effectiveness for the turbine blade especially at the trailing edge, underlining the importance of channel design in enhancing turbine blade thermal performance. This study offers critical insights into turbine blade cooling, with implications for improving the operational efficiency and lifespan of gas turbine engines.

The promotional work has been composed in the English language, it contains 145 pages, 69 figures, 9 table, references up to 106 literature sources.

Table of Contents

List Of Figures 9
List Of Tables 11
TERMINOLOGY AND ACRONYMS 12
INTRODUCTION 13
The Topic Relevance 14
The Aim and Objectives of Doctoral Thesis 15
Thesis Presents Following Scientific Novelty: 16
Practical Application of the Thesis 16
Thesis Structure and Its Main Results 17
Research Methodology 19
Thesis Approbation and Publications 21
Scientific Journals 21
Conferences Papers 21
1. GAS TURBINE ENGINES OVERVIEW AND COOLING TECHNOLOGY 24
1.1. Bryton Cycle 25
1.2. Gas Turbine Engine Cooling Process 26
1.3. Overview: Turbine Blade Cooling Technology 28
1.3.1. Turbine Blade Cooling Research Review 28
1.3.2. Internal Cooling 31
1.4. Different Internal Cooling Configurations 35
1.4.1. Radial Flow and Multi-Pass Serpentine Cooling 35
1.4.2. Trailing Edge Cooling 36
1.4.3. Jet Impingement type From Multiple Jet 38
1.5. Conjugate Heat Transfer 39
2. STATISTICS AND INVESTIGATION OF CF6 JET ENGINES HOT SECTION FAILURES 42
2.1. Introduction 42
2.2. CF6 Engine Models Configuration 42
2.3. Engine Performance Analysis 43
2.4 EGT& EGT Margin Monitoring 44
2.4. Engine Operation and Maintenance 46
2.5. Analysis of CF6 engines based on Borescope Inspection (BI) 46
2.5.1. Low Pressure Compressor Borescope Inspection 48
2.5.2. High Pressure Compressor Results 48

2.5.3. Combustion Chamber Borescope Inspection Analysis Results 49
2.6. High Pressure Turbine Nozzle Guide Vanes Borescope Results 49
2.7. High Pressure Turbine Borescope Results 50
2.8. Borescope Inspection Summary 51
2.9. Summary Of Chapter 2 53
3. COMPUTATIONAL FLUID DYNAMICS ANALYSIS OF FLOW CHARACTERISTICS AND HEAT TRANSFER VARIABILITIES **IN MULTIPLE TURBINE BLADE COOLING CHANNELS** 54
3.1. Introduction 54
3.2. Methodology 56
3.3. U Bend Cooling Channel (Case 1) 57
3.4. Net Bend Cooling Channels Design (Case 2) 60
3.5. Jet Impingement type Cooling Channels Optimization (Case 3) 62
3.6. Numerical Method 65
3.7. Parameter Definition 66
3.8. Boundary Condition 68
3.9. Results 69
3.9.1. Cooling Performance: 69
3.9.2. Performance Analysis for U Bend Cooling Channel 69
3.10. Performance Analysis for Net Bend Cooling Channels 73
3.11. Performance Analysis for Jet Impingement Type Cooling Channels 77
3.12. Result Comparison of Cooling Channels Flow Characteristics 81
3.13. Discussion 84
3.14. Summary Of Chapter 3. 85
4. DESIGN OPTIMIZATION OF TURBINE BLADE COOLING CHANNELS BY APPLYING JET IMPINGEMENT TYPE COOLING CHANNELS. 87
4.1. Introduction 87
4.2. Methodology 88
4.3. Initial Base Model Configuration 89
4.4. Mathematical Model 91
4.5. Heat Transfer Conjugation 93
4.6. Boundary Condition 98
4.7. Base Model Meshing 99
4.8. Optimized Model Configuration 101
4.9. Validation of the flow domain 102
4.10. Results 103

4.10.1. Configuration Of Base Model 103
4.10.2. Trailing Edge Focus 106
4.11. Conjugate Heat Transfer 109
4.12. Determination Of Cooling Effectiveness for The Optimized Model 112
4.13. Summary Of Chapter 4 113
GENERAL CONCLUSIONS 116
REFERENCES 118
Appendix 1 126
Appendix 2 127

List Of Figures

FIG. 1.1 GAS TURBINE ENGINE CROSS SECTION[4] 24
FIG. 1.2 BRAYTON CYCLE [8] 25
FIG. 1.3 TYPICAL GAS TURBINE ENGINE COOLING AND SEALING FOR AIRFLOWS. [15] 27
FIG. 1.4 HISTORICAL PROGRESS OF TURBINE INLET TEMPERATURE WITH TIME. [21] 29
FIG. 1.5 THE TURBINE BLADE COOLING SYSTEM PROBLEM PARAMETERS 30
FIG. 1.6 COOLING ARCHITECTURE OF A MODERN GAS TURBINE BLADE. (A) EXTERNAL FILM COOLING, (B) INTERNAL IMPINGEMENT COOLING AND SERPENTINE CHANNEL COOLING: [28] 31
FIG. 1.7 TURBINE BLADE/VANE WITH AN INSIDE SERPENTINE SHAPE COOLING CONFIGURATION[32] 32
FIG. 1.8 SCHEMATIC OF SERPENTINE PASSAGEWAYS WITH MANY PASSES FOR INTERNAL COOLING OF TURBINE BLADES.[54] 36
FIG. 1.9 EXPERIMENT ON ENERGY EFFICIENT ENGINE (E3) SHOWING THE VARYING TEMPERATURE FOR THE 1ST STAGE HIGH PRESSURE TURBINE VANE[56]. 37
FIG. 1.10 TYPICAL TEST MODEL USED BY FLORSCHUETZ ET AL. [62] 39
FIG. 1.11 RIG LAYOUT FOR RIB CHT ANALYSIS A.) FULL RIG WITH HIGHLIGHTED SECTIONS B.) RIB SETUP[71] 41
FIG. 2.1 SCHEMATIC OF CF6 TURBOFAN ENGINE. [75] 43
FIG. 2.2 EGT TO THRUST RATING RELATION. 45
FIG. 2.3 EGT MARGIN TO ENGINES LIFE RELATION. 46
FIG. 2.4 HPC STAGES 48
FIG. 2.5 COMBUSTION CHAMBER (DOME ASSEMBLY &SPECTACLE PLATE) 49
FIG. 2.6 HPT STAGE 1 NOZZLE GUIDE VANES. 50
FIG. 2.7 HPT STAGE 2 NOZZLE GUIDE VANES 51
FIG. 2.8 HPT STAGE 1 BLADES. 51
FIG. 3.1 . U-BEND MODEL CONFIGURATION 57
FIG. 3.2 3D U-BEND MODEL FLOW DOMAIN 57
FIG. 3.3 D U BEND MESH CONFIGURATION 59
FIG. 3.4 3D U-BEND INFLATION LAYERS 59
FIG. 3.5 U BEND MESH ELEMENT ASPECT RATIO 59
FIG. 3.6 NET BEND OPTIMIZED MODEL. 60
FIG. 3.7.NET CHANNELS MESH CONFIGURATION 61
FIG. 3.8 INFLATION MESH LAYERS 61
FIG. 3.9 MESH ASPECT RATIO QUALITY FOR NET CHANNELS 61
FIG. 3.10MESH INDEPENDENCE CRITERIA BETWEEN MESH ELEMENTS AND VELOCITY AT DIFFERENT MESH ELEMENT CONFIGURATION. 62
FIG. 3.11 JET IMPINGEMENT COOLING CHANNELS CONFIGURATION 63
FIG. 3.12 JET IMPINGEMENT COOLING CHANNELS CONFIGURATION JOINTS 63
FIG. 3.13 JET IMPINGEMENT TYPE MESH CONFIGURATION 64

FIG. 3.14 JET IMPINGEMENT TYPE MESH ELEMENT ASPECT RATIO 65
FIG. 3.15 U BEND TEMPERATURE CONTOURS 70
FIG. 3.16 U BEND VELOCITY COUNTERS 70
FIG. 3.17 U BEND PRESSURE COUNTERS 71
FIG. 3.18 GRAPH BETWEEN FRICTION FACTOR (F), AND (RE) REYNOLDS NUMBER FOR U CHANNEL 72
FIG. 3.19 .NET COOLING CHANNEL TEMPERATURE CONTOURS. 73
FIG. 3.20. NET COOLING CHANNEL VELOCITY CONTOURS 74
FIG. 3.21 .NET COOLING CHANNEL PRESSURE CONTOURS 75
FIG. 3.22 THE VARIATION OF FRACTION FACTOR WITH RENOLDS NUMBER FOR NET COOLING CHANNELS. 76
FIG. 3.23 JET IMPINGEMENT TYPE COOLING CHANNEL VELOCITY VECTORS. 78
FIG. 3.24. JET IMPINGEMENT TYPE COOLING CHANNEL TEMPERATURE CONTOURS. 78
FIG. 3.25. JET IMPINGEMENT TYPE COOLING CHANNEL PRESSURE CONTOURS 79
FIG. 3.26. VARIATION OF FRICTION FACTOR WITH REYNOLDS NUMBER FOR JET IMPINGEMENTS TYPE COOLING CHANNELS. 80
FIG. 3.27. VARIATION OF DRAG FORCE WITH RENOLDS NUMBER 81
FIG. 3.28. COMPARISON OF N_{UA}/N_{UO} VS. RENOLDS NUMBER FOR COOLING CHANNELS. 82
FIG. 3.29. THE VARIATION F/F0 WITH RENOLDS NUMBER FOR DIFFERENT COOLING CHANNELS. 83
FIG. 3.30. THE VARIATION TP WITH RENOLDS NUMBER COOLING CHANNELS. 84
FIG. 4.1 FINITE ELEMENT GRIP STRUCTURE FOR NASA C3X WITH COOLING CHANNEL'S LOCATIONS [50] 90
FIG. 4.2.BASE MODEL TURBINE BLADE COOLING 91
FIG. 4.3 THE 3D DOMAIN FOR THE CONJUGATE HEAT TRANSFER SIMULATION. 96
FIG. 4.4. FLUID DOMAIN MESHING 100
FIG. 4.5 FULL NASA C3X VANE MESHING: (A) FULL NASA C3X VANE MESHING; (B) BASE MODEL COOLING CHANNELS MESHING. 100
FIG. 4.6. ASPECT RATIO MESH. 101
FIG. 4.7. FLOW DOMAIN AND OPTIMIZED TURBINE BLADE COOLING CHANNEL MODEL: (A) HOT DOMAIN CONFIGURATION; (B) OPTIMIZED TURBINE BLADE COOLING CHANNELS. 102
FIG. 4.8. CFD ABSOLUTE PRESSURE FLOW DOMAIN 103
FIG. 4.9. NORMALIZED C3X VANE SPAN COORDINATE [50]. 104
FIG. 4.10.BASE MODEL MEAN GAUGE PRESSURE DATA COMPARED WITH C3X VANE DATA. 104
FIG. 4.11. BASE MODEL TEMPERATURE COMPARISON WITH NASA C3X EXPERIMENTAL DATA. 105
FIG. 4.12. AVERAGE HEAT TRANSFER COEFFICIENT COMPARISON. 105
FIG. 4.13.. BASE MODEL MEAN TEMPERATURE DATA COMPARISON BETWEEN THE REFERENCE DATA. 106
FIG. 4.14.TRAILING EDGE TEMPERATURE COMPARISON BETWEEN NASA BASE MODEL AND JET IMPINGEMENT TYPE COOLING CHANNELS. 107
FIG. 4.15. TRAILING EDGE TEMPERATURE COMPARISON BETWEEN NASA BASE MODEL AND JET IMPINGEMENT TYPE COOLING CHANNELS. 107
FIG. 4.16 TEMPERATURE CONTOURS FOR THE COOLING CHANNELS IN THE TURBINE BLADE WALL 108

FIG. 4.17. TRAILING EDGE TEMPERATURE COMPARISON BETWEEN NASA BASE MODEL AND JET IMPINGEMENT TYPE COOLING CHANNELS. 109
FIG. 4.18. AVERAGE HEAT TRANSFER COEFFICIENT COMPARISON BETWEEN NASA C3X EXPERIMENT DATA, WANG EXPERIMENT DATA, AND CURRENT STUDY BASE MODEL. 110
FIG. 4.19. AVERAGE HEAT TRANSFER COEFFICIENT COMPARISON BETWEEN NASA BASE MODEL, AND JET IMPINGEMENT TYPE. 111
FIG. 4.20. BLADE WALL HEAT FLUX COMPARISON BETWEEN NASA BASE MODEL, AND OPTIMIZED MODEL. 112

List Of Tables

TABLE 1 INVOLVEMENT IN THE PRODUCTION OF SCIENTIFIC PUBLICATIONS. 23
TABLE 2 STATISTICAL ANALYSIS FOR DIFFERENT FAILURE TYPES AND LOCATIONS FOR CF6 ENGINES 52
TABLE 3 COOLING CHANNEL DESIGNS 57
TABLE 4. INITIAL FLOW CONDITION FOR THE DOMAIN. 69
TABLE 5 U BEND DRAG FORCES AT LOCATIONS A, B, C, AND D. 73
TABLE 6 NET COOLING CHANNELS DRAG FORCES AT LOCATIONS A, B, AND C. 77
TABLE 7 NASA C3X AIRFOIL VANE COORDINATES [49] 89
TABLE 8.BOUNDARY CONDITION FOR THE DOMAIN. 99
TABLE 9 COOLING CHANNELS INPUT BOUNDARY CONDITIONS. 99

TERMINOLOGY AND ACRONYMS

CHT – Conjugate Heat Transfer

CFD – Computational Fluid Dynamics

RANS – Reynolds-Averaged Navier-Stokes

HPT – High Pressure Turbine

LPT – Low Pressure Turbine

HPC – High Pressure Compressor

LPC – Low Pressure Compressor

NGV – Nozzle Guide Vane

TBC – Thermal Barrier Coatings

FOD – Foreign Object Damage

EGTM – Exhaust Gas Temperature Margin

TSN – Time Since New

CNC – Cycle Number Since New

LE – Leading Edge

BI – Borescope Inspection

TP – Thermal Performance

INTRODUCTION

Gas turbine engines, a specialized type of internal combustion engine, operate by harnessing continuous fuel combustion to drive a turbine. This turbine, in turn, powers a compressor and generator, often used for electricity generation. These engines have widespread applications in power generation, aviation, and marine propulsion. The reliability and performance of gas turbine engines are significantly impacted by the potential failure of turbine blades due to cooling challenges.

To improve the energy extracted from combustion and enhance efficiency, gas turbine engines benefit from raising the gas temperature entering the turbine. However, this elevated temperature places greater stress on turbine blades, potentially compromising their strength and lifespan. To address this challenge, the industry employs materials with higher heat resistance and sophisticated cooling techniques to ensure that the blades operate safely.

Balancing the desire for higher operational temperatures to improve efficiency with the need for safety is an ongoing industry challenge. Cooling issues can arise from various factors, including blockages in cooling passages, insufficient coolant flow rates, or improper coolant temperatures, leading to overheating and potential blade damage. A malfunctioning blade can not only affect other engine components but also disrupt airflow and cause imbalanced rotations, resulting in significant engine vibrations and the possibility of catastrophic engine failure. Therefore, effective cooling system design and maintenance are essential to prevent such problems and ensure the safe and efficient operation of gas turbine engines.

Addressing the challenges posed by increasing turbine inlet temperatures requires the implementation of advanced cooling configurations, optimization techniques, and Conjugate Heat Transfer (CHT) analyses. These cooling configurations aim to strike a balance between efficient blade cooling and minimizing efficiency losses. Optimization methods enable the identification of the most effective cooling strategies through numerical simulations and modeling. CHT analyses provide a deeper understanding of the heat transfer processes within the blades, allowing for improvements in cooling system design and efficiency.

By integrating these approaches, engineers and researchers in the gas turbine industry can develop cooling solutions that effectively manage elevated temperatures while ensuring the safe and reliable performance of gas turbine engines.

The Topic Relevance

Turbine blades are critical components in gas turbine engines that are exposed to high temperatures and thermal stresses during operation. The blades are subjected to extreme heat generated by the combustion of fuel and air in the combustion chamber, which can cause the blades to overheat and fail if not properly managed.

One common method of managing the high temperatures in turbine blades is to use cooling techniques. Cooling can be achieved by passing a coolant fluid, typically air or a mixture of air and fuel, through internal channels in the blade. The coolant fluid absorbs some of the heat generated by the combustion process and carries it away from the blade, which helps to keep the blade temperature within a safe operating range. However, the cooling process can also introduce new challenges in the design and operation of turbine blades. The design of the cooling channels must be optimized to ensure efficient heat transfer and minimize pressure losses. The coolant fluid flow rate, temperature, and distribution must also be carefully controlled to avoid hot spots and thermal gradients that can lead to thermal stresses and blade failure.

In addition, the use of cooling channels can also affect the aerodynamic performance of the blade. The presence of cooling channels can increase the surface roughness of the blade, which can increase drag and reduce the overall efficiency of the engine. Therefore, the design of the cooling channels must also consider the aerodynamic performance of the blade and minimize any negative effects on the engine's overall efficiency.

Overall, the cooling of turbine blades is a critical aspect of gas turbine engine design and operation. Effective cooling techniques can help to increase the service life of turbine blades and improve the performance and reliability of gas turbine engines.

The complex geometry of cooling channels makes them difficult and expensive to manufacture. Additionally, the small size of the channels can make them difficult to inspect and maintain. The researcher’s goal is to design a new geometry that can achieve better cooling configuration and is easily manufacturable.

The Above problems determine the purpose of this work.

The Aim and Objectives of Doctoral Thesis

The main aim of this study is to investigate the performance improvement of turbine blade cooling for gas turbine engines by optimizing the design of turbine blade cooling channels. Turbine blade failures occur due to cooling problems and can have serious consequences on the performance and reliability of a gas turbine engine. It, therefore, is based on these reasons that the set objectives were investigated.

Objectives

1. Design and optimization of the special type of turbine blade cooling channels (U Bend type, Net type, and Jet impingement type) for improved heat transfer and cooling efficiency.
2. To investigate the CF6 engine failure due to heat effects causing damage to turbine blade.
3. To carry out Computational Fluid Dynamic (CFD) based analysis for investigation of heat transfer and flow phenomenon in turbine blade cooling channels.
4. To develop MATLAB codes to integrate with CFD software for the temperature profiles and heat transfer.
5. To compare the thermal performance and aerodynamic characteristics of the three designed cooling channels.
6. To carry out heat transfer conjugation analysis with real turbine blade boundary conditions and compare with reference experiment results.
7. To compare the results achieved from the doctoral thesis with the experimental studies of literature.

Thesis Presents Following Scientific Novelty:

1. Specially designed jet impingement type of turbine blade cooling channels that are optimized for the turbine blade for enhanced cooling.
2. A notable achievement of this study is the detailed temperature profiling, especially at the trailing edge and suction side of turbine blades. This advancement provides critical insights into thermal stresses and performance, contributing to the prolonged durability and effectiveness of turbine systems.
3. Qualitative and quantitative analysis of the turbine blade cooling channels thermal performance under various operational conditions.
4. Development of MATLAB algorithms which can be integrated with the CFD simulation environment and provide extremely accurate results for the complex aerodynamic and heat transfer analysis within blade cooling channels.

Practical Application of the Thesis

1. This research directly contributes to the turbine manufacturing industry. The Proposed design of the cooling channels can be seamlessly integrated into existing turbine production processes. Adaptations required for this integration are minimal given the fact that modern additive manufacturing techniques can help this adaptation, offering a straightforward path towards enhancing turbine blade performance and extending their operational lifespan.

2. The optimized cooling channels significantly boost the cooling efficiency of turbine blades. By facilitating more effective heat dissipation, these designs can lead to a marked reduction in operational cost.

3. The cooling channel design showcased in this thesis is highly scalable and versatile, adaptable to various turbine sizes and types. This universal applicability makes the research valuable not just for large-scale power plants but also for smaller, localized energy generation applications.

4. The improved cooling efficiency also impacts maintenance needs and the durability of turbine blades. Enhanced cooling reduces thermal stress, thereby diminishing the

frequency of maintenance and repairs.

Thesis Structure and Its Main Results

The thesis consists of the introduction, Four chapters, with a conclusion. In the introduction, the relevance and significance of the study were articulated. Further, the research aims, objectives, and the scope—including both the subject and object of investigation were comprehensively outlined.

Chapter One serves as an exhaustive exploration into Gas Turbines, tracing its historical evolution and operational mechanics. This chapter also delves into advanced aspects such as the cooling processes of Gas Turbine engines and latest research advances in turbine blade cooling technologies.

Chapter Two is an additional but related study about engine performance that specifically focusses on empirical analysis, featuring a case study that examines the Hot Section Failures of CF6 Jet Engines. This investigation is grounded in test reports gathered from various aircraft sources across different geographic regions. It underscores the utilization of real data obtained from engine performance tests and Borescope Inspections (BI) reports. This data serves as the foundation for scrutinizing the occurrences of failures within the CF6 sections, particularly the High-Pressure Turbine (HPT) section. The chapter also presents a statistical analysis of the behavior and deterioration of engine parameters. One notable aspect of this analysis is the monitoring of Exhaust Gas Temperature (EGT) and EGT margin for CF6 engines operating in diverse climatic zones. This examination explores the correlation between take-off EGT, and take-off thrust for CF6 engines utilized in B747-400 aircraft. It reveals variations in engine conditions based on the climatic zones in which these engines operate.

Chapter Three employs Computational Fluid Dynamics (CFD) to optimize and analyze the flow characteristics and heat transfer variations in different cooling channel types of turbine blades as U bend, Net type, and Jet impingement type cooling channel. The chapter also highlights the thermal and hydraulic characteristics of various cooling channel configurations at different Reynolds numbers (Re). Key findings indicate that slimmer

turning vanes are more effective in reducing drag and improving thermal performance. Net type Cooling channels (Case 2) showed promising results in the Nu_a/Nu_0 ratio at a Re range of 10,000 to 50,000, while jet impingement type (Case 3) excelled in drag reduction at Re=30,000. Intriguingly, drag force remained constant across extensive Re ranges, suggesting a form of robustness in fluid dynamics. The results have significant implications for optimizing cooling efficiency in different operational conditions.

*Chapter Four i*s dedicated to the optimization of referenced data concerning cooling channels for turbine blades, specifically through the implementation of jet impingement-type cooling techniques. The chapter also encompasses the validation results obtained from the comparison of both simulation and reference experimental data.

These results uncover a more pronounced temperature profile, particularly along the blade's edge regions, with a prominent effect on the blade's suction side. These disparities are a consequence of the inherent limitations of CFD simulations, as previously discussed. Notably, the temperature at the center of the blade registers as higher, with variations spanning from 10 to 35K. Nevertheless, the temperature contours observed in both investigations exhibit a consistent overall pattern, with the vane's trailing edge being the hottest point at 670+K.The comparison drawn between the CFD results of the current study and the NASA model results facilitates an analysis of the correlation between these two datasets and the accuracy of the current CFD model. The slight deviations between the two datasets can be attributed to the diverse assumptions and simplifications integrated into the current study's CFD model, as well as potential experimental inaccuracies in the NASA data.

.

Conclusions contain a summary of the executed work, section synthesizes the research findings, highlighting the most consequential outcomes and suggesting avenues for future scholarly inquiry.

Research Methodology

Aa the turbine blade cooling channel is complicated flow mechanism within the blades, the detailed flow phenomenon and its qualitative and quantitative analysis is arguable only possible by numerical analysis conducted by means of Computational Fluid Dynamics (CFD). In turn, this numerical analysis can provide a good comparison to the overall experimental performance of the turbine blade passages. Computational Fluid Dynamics (CFD) stands as a potent instrument for the purpose of conceptualizing cooling setups for gas turbine blades. CFD simulations offer intricate insights into the anticipated flow patterns and heat transfer behaviors within the turbine blade. These insights, in turn, serve as a foundation for enhancing the cooling system's design and elevating the blade's thermal efficiency. The ensuing sections elucidate the methodologies harnessed in this research:

1. **Literature Survey**: The initial phase involves an extensive literature survey. This entails gathering and critically evaluating data from prior studies that have delved into gas turbine blade cooling configurations. These studies serve as a foundational reference for both computational and experimental aspects of the research.

2. **Modeling and Design with SolidWorks**: To materialize the cooling configurations, a meticulous 3D Computer-Aided Design (CAD) model of the gas turbine blade and associated cooling system is crafted using SolidWorks. This step ensures a detailed and accurate representation of the physical components.

3. **Initial Domain Configuration**: The research proceeds by establishing the initial configuration of the simulation domain. This entails defining the fundamental geometry and dimensions, encompassing the gas turbine blade and the encompassing fluid domain.

4. **Mesh Generation via ANSYS ICEM-CFD**: The generation of a high-fidelity mesh is pivotal for an accurate simulation. ANSYS ICEM-CFD is harnessed for this purpose, meticulously constructing a mesh that mirrors the intricate geometry of the gas turbine blade and the surrounding fluid domain.

5. **Selection of Heat Transfer Model**: A judicious choice of the heat transfer model is made, contingent on a thorough review of available options. The selected model will be

instrumental in simulating the intricate heat transfer dynamics between the gas turbine blade and the surrounding fluid. One of the potential models considered is the Conjugate Heat Transfer (CHT) model.

6. **Selection of Turbulence Model**: The turbulence within the fluid domain is addressed by selecting an appropriate turbulence model. This choice is informed by a comprehensive review of available models, with contenders such as the SST k-omega or k-epsilon model under consideration.

7. **Development of MATLAB Coding**: A custom MATLAB code is crafted to facilitate essential calculations for the CFD simulation. These codes play a pivotal role in processing and analyzing simulation data, facilitating comparisons with reference experimental data.

8. **CFD Simulation with ANSYS FLUENT**: The heart of the research lies in the CFD simulation itself, which is executed using ANSYS FLUENT as the CFD solver. The selected heat transfer and turbulence models, in conjunction with the custom MATLAB algorithm, are instrumental in conducting the simulation. Subsequently, the obtained simulation results are meticulously compared with referenced experimental data, serving as a crucial validation step.

The use of CFD simulations provides several advantages lower costs, faster operation than the experimental methods, which allows for a more comprehensive analysis of the flow and heat transfer within the turbine blade. Additionally, CFD simulations can provide detailed information about the flow and heat transfer at different points within the blade, which can be used to design more efficient augmented heat transfer channels. Therefore, the study employed ANSYS FLUENT code as a CFD solver, and ANSYS ICEM-CFD was used for mesh generation. ANSYS FLUENT is a widely used commercial CFD software that can solve a wide range of fluid flow and heat transfer problems and can also generate high-quality meshes that are suitable for use in CFD simulations. Together, these tools can be used to perform detailed and accurate CFD simulations of the cooling configurations in a gas turbine blade.

Thesis Approbation and Publications

In the period of making of the thesis 7 publications have been published in international journals and conferences:

Scientific Journals

Full-text journal papers published indexed in SCOPUS or WOS database:

1. Elmenshawy Adham Ahmed Awad Elsayed, Alomar Iyad and Arshad Ali. "Optimization Turbine Blade Cooling by Applying Jet Impingement Cooling Channels" *Transport and Telecommunication Journal 24*, no.3 (2023): 320-337. https://doi.org/10.2478/ttj-2023-0026.
2. Elmenshawy Adham Ahmed Awad Elsayed, Alomar Iyad, Arshad Ali, and Medvedevs Aleksandrs. "Computational Fluid Dynamics Analysis of Flow Characteristics and Heat Transfer Variabilities in Multiple Turbine Blade Cooling Channels" *Transport and Telecommunication* Journal 25, no.1 (2024): 77-96. https:// doi.org/10.2478/ttj-2024-0008.
3. Arshad Ali, Cong P, Elmenshawy Adham Ahmed Awad Elsayed, and Blumbergs Ilmārs, "Design optimization for the weight reduction of 2-cylinder reciprocating compressor crankshaft," *Archive of Mechanical Engineering, vol. 68, no. 4, pp. 449–471*, 2021, doi: 10.24425/ame.2021.139311.
4. Nagaraj. Pavithra., Elmenshawy Adham Ahmed Awad Elsayed, and Alomar Iyad, "Vibroacoustic Soundproofing for Helicopter Interior," *Aviation journal, 27(1), 57–66*.2023, https://doi.org/10.3846/aviation.2023.18629

Conferences Papers

Full-text conference papers published in conference proceedings indexed in SCOPUSor WOS database.

1. A. A. A. E. Elmenshawy and I. Alomar, "Statistics and Investigation of CF6 Jet Engines Hot Section Failures," Reliability and Statistics in Transportation and Communication. RelStat 2021. Lecture Notes in Networks and Systems, vol 410. Springer, Cham2022, pp. 88–98 . https://doi.org/10.1007/978-3-030-96196-1_9.

2. A. Arshad, A. J. Kallungal, and A. A. A. E. Elmenshawy, “Stability Analysis for a Concept Design of Vertical Take-off and Landing (VTOL) Unmanned Aerial Vehicle (UAV),” in 2021 International Conference on Military Technologies (ICMT), Jun. 2021, pp. 1–6. doi: 10.1109/ICMT52455.2021.9502764.
3. A. A. A. E. Elmenshawy and Y. A. H. Alshwaily, “Optimization of Propeller Performance for a Quadcopter Drone by Applying Aerodynamic Propeller-Ducts,” Reliability and Statistics in Transportation and Communication. RelStat 2021. Lecture Notes in Networks and Systems, vol 410. Springer 2022, pp. 186–197. doi: 10.1007/978-3-030-96196-1_17.

Author’s Contribution to Publications

The scientific publications were produced through a collaborative effort involving the supervisors Professor Ali Arshad, as well as co-authors and consultants. The authors jointly planned and carried out the work on these publications. Table 1 provides a summary of the author's contributions to the research work included in the scientific publications.

Table 1

Involvement in the production of scientific publications.

Nr.	Publikācijas nosaukums	Publikācijas vieta	Līdzautoru daļa%								
			Elmenshawy A	Arshad A.	Alomar I.	Blumbergs I.	Cong P.	Kallungal A.	Alshwaily Y.	Nagaraga P.	Medvedevs A.
1.	Optimization Turbine Blade Cooling by Applying Jet Impingement Cooling Channels	Transport and Telecommunication Journal 24, no.3 (2023): 320-337. 320-337. https://doi.org/10.2478/ttj-2023-0026.	60	20	20						
2.	Statistics and Investigation of CF6 Jet Engines Hot Section Failures	Reliability and Statistics in Transportation and Communication. RelStat 2021. Lecture Notes in Networks and Systems, vol 410. Springer, Cham2022, pp. 88–98 . https://doi.org/10.1007/978-3-030-96196-1_9	50		50						
3.	Design optimization for the weight reduction of 2-cylinder reciprocating compressor crankshaft	Archive of Mechanical Engineering, vol. 68, no. 4, pp. 449–471, 2021, doi: 10.24425/ame.2021.139311.	20	40		20	20				
4.	Stability Analysis for a Concept Design of Vertical Take-off and Landing (VTOL) Unmanned Aerial Vehicle (UAV),	2021 International Conference on Military Technologies (ICMT), Jun. 2021, pp. 1–6. doi: 10.1109/ICMT52455.2021.9502764.	20	60				20			
5.	Optimization of Propeller Performance for a Quadcopter Drone by Applying Aerodynamic Propeller-Ducts,"	Reliability and Statistics in Transportation and Communication RelStat 2021. Lecture Notes in Networks and Systems, vol 410. Springer 2022, pp. 186–197. doi: 10.1007/978-3-030-96196-1_17.	50						50		
6.	Vibroacoustic Soundproofing for Helicopter Interior	Aviation journal, 27(1), 57–66.2023, doi: 10.3846/aviation.2023.18629	40		20					40	
7.	Computational Fluid Dynamics Analysis of Flow Characteristics and Heat Transfer Variabilities in Multiple Turbine Blade Cooling Channels"	" Transport and Telecommunication Journal 25, no.1 (2024): 77-96. https:// doi.org/10.2478/ttj-2024-0008.	40	20	20						20

1. GAS TURBINE ENGINES OVERVIEW AND COOLING TECHNOLOGY

Gas turbine engines boast a rich and extensive chronicle that covers more than 100 years. Initially conceptualized by John Barber in 1791 [1], the idea of using ongoing combustion to energize a turbine didn't materialize into practical applications until the early 1900s [2].

Among the pioneers in the field, French engineer Auguste Rateau made significant strides with a rudimentary gas turbine engine in 1903 [2]. His invention incorporated a straightforward axial compressor, a combustion chamber, and a turbine to energize a modest electrical generator. Over subsequent years, advancements in design and engineering led to more efficient and capable engines. The application of gas turbine technology in aircraft propulsion came to fruition during the Second World War, ushering in the era of turbojet engines. This served as a watershed moment in the technological timeline of gas turbines, facilitating their broader adoption in the aviation sector. Post-war periods witnessed continued advancements, including the introduction of sophisticated designs, novel materials, and cutting-edge cooling methods. At their core, gas turbine engines comprise a compressor, a combustion chamber, a turbine, and an exhaust outlet. The operational cycle involves the perpetual compression of air, which is blended with fuel and ignited in the combustion chamber. The resultant hot gases propel the turbine, which in turn powers the compressor and any attached generators [3]. Finally, the cooled exhaust gases are vented out through the nozzle. Fig.1.1 shows the gas turbine engine cross section.

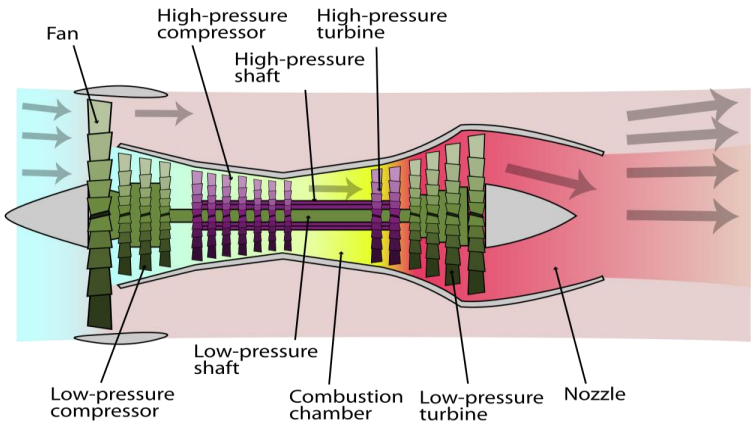

Fig. 1.1 Gas turbine engine cross section [4].

The functionality of a gas turbine engine is primarily split into two key phases: the act of compressing air and the subsequent expansion process. During the compression phase, air is sucked into the engine and subjected to both pressure and temperature increases. This conditioned air then merges with fuel in the combustion chamber, igniting to form heated gases. These gases are funneled through the turbine in the expansion phase, instigating its rotation which, in turn, powers both the compressor and the electrical generator.

The engine's operational efficiency is influenced by multiple variables, such as the temperature levels at different stages—during air compression, post-combustion, and prior to re-entering the compressor. Additionally, the structural design and the selection of materials employed in the engine's assembly have a significant impact on its overall performance [5].

Gas turbine engines find diverse applications across sectors like electrical power production, aerial transportation, and nautical propulsion systems [6]. They present a range of benefits when compared to alternative engine types, including a superior power-to-weight ratio, minimal vibrational disturbances, and elevated reliability levels. Nonetheless, they are not without challenges, one of the primaries being the efficient thermal management of the heated gases, which has long-term implications on both durability and operational effectiveness.

1.1. Bryton Cycle

The Brayton cycle serves as the thermodynamic framework underlying the functioning of gas turbine engines, a category of internal combustion engines. Alternatively referred to as the Joule cycle, it takes its name from George Brayton, the American engineer credited with developing the inaugural practical gas turbine engine during the late 19th century [7]. Fig.1.2 presents the Bryton cycle.

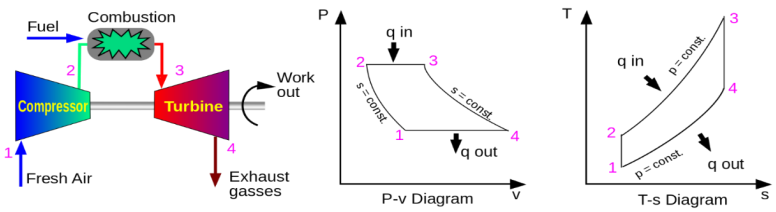

Fig. 1.2 Brayton cycle [8].

The Brayton cycle involves four processes:

- Isentropic compression: Air is compressed from the inlet to a high pressure.
- Constant pressure heating: The compressed air is heated by adding heat from an external source, such as combustion of fuel.
- Isentropic expansion: The hot air expands through a turbine to produce work.
- Constant volume cooling: The expanded air is cooled, typically by passing it through a heat exchanger, before being recycled back to the inlet.

The Brayton cycle efficiency is dependent on the temperatures and pressures involved in the four processes, as well as the design of the engine components like the compressor, turbine, and heat exchanger. The Brayton cycle is commonly employed in gas turbine engines for power generation, aviation, and other industrial applications.

1.2. Gas Turbine Engine Cooling Process

In a gas turbine engine, the secondary air system is responsible for providing cooling and sealing air to various components of the engine [9]. The typical cooling and sealing airflows circulating through the secondary air system include:

1. Compressor Discharge Air: Compressed air from the compressor is directed to the combustion chamber, where it provides cooling to the hot components, such as the combustor liners and turbine blades [10].

2. Bleed Air: A portion of the compressed air is bled off from the compressor discharge and is used for cooling and sealing purposes.

3. Film Cooling Air: The film cooling air is introduced into the engine at high velocity through special nozzles, creating a thin layer of cool air over the hot components, such as the turbine blades and vanes [11]. This protects the metal from excessive heat and reduces the risk of failure.

4. Seal Air: Seal air is directed to various engine components, such as the rotor seals, bearing seals, and casing seals, to prevent leaks. The pressure of the seal air is carefully controlled to ensure that it provides an effective seal while minimizing the impact on engine performance [12].

5. Cooling and Sealing Air Flow Control: The cooling and sealing airflows are controlled by various valves, such as bleed valves and film cooling air valves, which regulate the flow and pressure of the air. The airflows are also monitored to ensure that they are at the correct temperature and pressure and are distributed appropriately to the various engine components [13].

The process of the secondary air system helps to keep the engine components cool, prevent leaks, and maintain engine performance. The design of the secondary air system is critical to the overall performance and reliability of the gas turbine engine [14].

Fig.1.3 presents Typical Gas turbine engine Cooling and Sealing for Airflows.

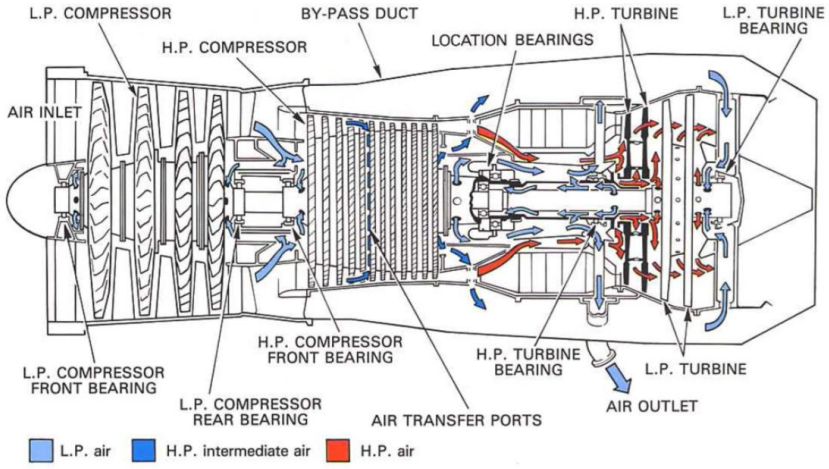

Fig. 1.3 Typical gas turbine engine cooling and sealing for airflows [15].

1.3. Overview: Turbine Blade Cooling Technology

1.3.1. Turbine Blade Cooling Research Review

`Turbine blade cooling is a critical aspect of gas turbine engines. The blades in a turbine rotate at high speeds and are subject to high temperatures due to the combustion of fuel. The main objective of turbine blade cooling is to prevent overheating, which can lead to decreased efficiency and damage to the blades. The cooling is necessary to ensure that the turbine can operate at peak efficiency and to extend the service life of the blades [16].

There are various cooling methods used in turbine blade design, such as film cooling, transpiration cooling, internal cooling, and others. These cooling methods are designed to provide a flow of cool air to the blade surface, which can come from different sources such as bleed air from the compressor or external source like the engine's fan. The design of the cooling channels, their location, and the cooling method used, depend on the specific application and the type of turbine. As the temperatures of gas turbine inlets have risen, they are now being operated at higher temperatures such as 1850 K. These higher temperatures put stress on the turbine blades and vanes, making cooling necessary to protect them from thermal failure as modern alloys can withstand temperatures up to 1350K only. Cooling of the turbine parts is necessary to protect the blades and vanes from thermal failure, as the high temperatures reached in gas turbine operation can cause damage to these components [17]. As the temperatures of gas turbine inlets have been increasing over the last few decades, it is expected that this trend will continue in the future. Advancements in turbine blade cooling technologies have made it possible for turbines to operate at higher temperatures and it is likely that these technologies will continue to improve, allowing for even higher temperatures to be reached. This trend is driven by the increasing demand for more efficient and powerful gas turbines [18]. Over the last 50 years, there has been a significant amount of research on gas turbine blade cooling techniques. Researchers have been using a combination of analytical, computational, and experimental methods to improve the cooling of gas turbine blades. These methods have been used to study various cooling techniques such as film cooling, impingement cooling, and internal cooling. Additionally, recent monographs have been focusing entirely on gas turbine heat transfer and associated cooling technology. This research has led to a better understanding of the heat transfer mechanisms involved in gas turbine operation and has resulted in the development of more effective cooling methods [19], [20]. Fig. 1.4 shows the

historical progress of turbine inlet temperature with time, since 1960's, and presents the improvement cooling and material technology [21].

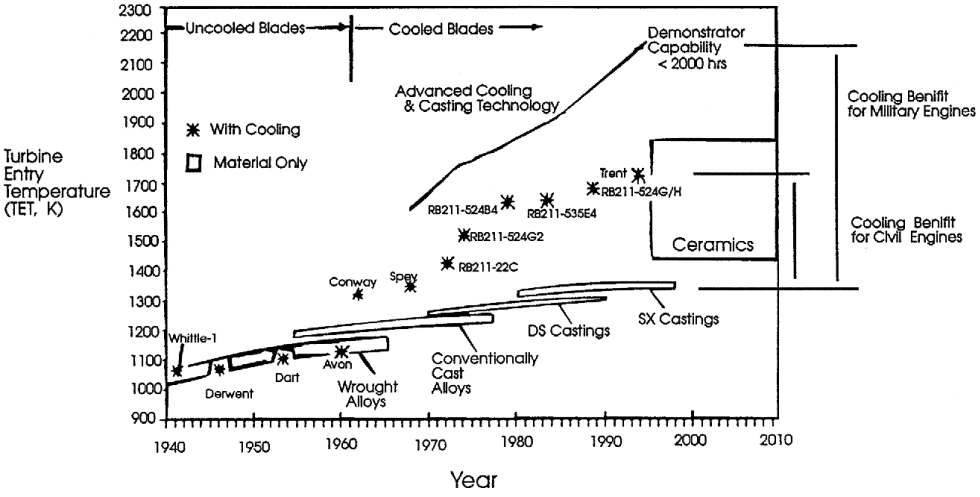

Fig. 1.4 Historical progress of turbine inlet temperature with time. [21]

There are several cooling systems used in turbine blades today, each with their own unique characteristics and advantages. This starting point refers to the process of how the turbine blades are cooled in a gas engine [22]. Cold air is extracted from the compressor and directed through an inlet channel at the blade root. This air then flows through one or more cooling systems, such as film cooling, internal convection cooling, transpiration cooling, or impingement cooling, which are designed to dissipate heat from the blades and maintain their structural integrity. The cold air is then exhausted through the turbine main vein. The type of cooling system used will depend on the engine design and operating conditions [23]. The cold air that is extracted from the compressor flows through one or several cooling channels within the blade, and then exhausted into the turbine main vein. The two main types of cooling that are used in turbine blades are external cooling and internal cooling. internal cooling of turbine blades has become an essential requirement for modern gas turbines as they are designed to handle increasing power demand and higher gas temperatures. As the power demand increases, the gas temperature in the turbine also increases, which can lead to temperatures that exceed the melting point of the blade material. If the blades are not cooled properly, they can become damaged or even fail, leading to costly repairs and downtime.

Internal cooling systems are used to dissipate heat from the blades and maintain their structural integrity. These cooling systems use internal channels within the blade to circulate coolant air, which absorbs heat from the blade and transports it away. This helps to keep the blade temperature below the melting point, thus allowing it to operate safely and efficiently.

Cooling systems are already used in gas turbines for all static parts, such as the turbine casing and the turbine nozzle guide vanes. However, incorporating cooling systems into rotating turbine blades is a more complex task [24]. The design process must consider the additional challenges posed by the rotation of the blades and the high temperatures experienced by the blades.

Internal cooling of turbine blades is a mandatory requirement for modern gas turbines to meet the increasing power demand and to handle the higher gas temperatures in the turbine that may surpass the material's melting point. However, designing an effective internal cooling system is a tricky process that requires a compromise between multiple physical parameters [25].

Designers must consider factors such as the coolant flow rate, coolant pressure, coolant temperature, blade geometry, and aerodynamic performance. They must also consider the distribution of the coolant throughout the blade and the way the heat is being dissipated[26]. Additionally, the designer must consider the weight, durability, and cost of the cooling system.

It's a complex process that requires a deep understanding of thermodynamics, aerodynamics, and material science. A compromise must be made between the various physical parameters to ensure that the blade's thermal performance, structural integrity, and aerodynamic performance are optimized [6]. Fig.1.5 presents the turbine blade cooling system Problem parameters.

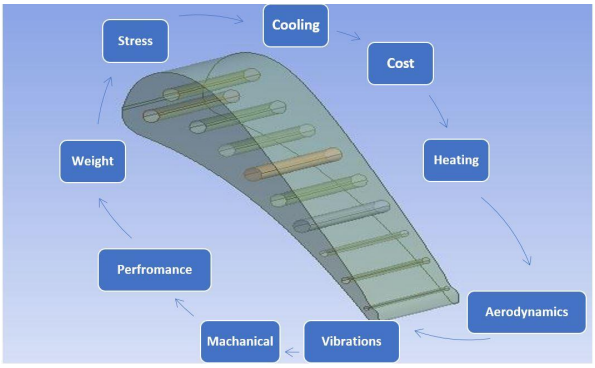

Fig. 1.5 The turbine blade cooling system problem parameters

The result of all this parameter selection is the blade life duration, and poor settings might lead to premature failures. explains the four major blade turbine failures and their temperature

dependence Creep, Corrosion, and Low cycle fatigue. Regarding the lifespan of turbine components, the Exceeding of operational temperature of 15°C can double or halve the life due to Creep, 20°C for Corrosion, and 30°C in the case of Low Cycle Fatigue [27]

The finding demonstrates the effect of tiny metal temperature changes on blade lifetime, which can be cut in half with a few dozen degrees higher temperatures. Through an analysis of uncertainty, Ireland concludes that current leading-edge industrial measurement tools fall short in providing the required precision for reliable lifetime forecasting (his calculations indicate a temperature uncertainty range from 35°C to 80°C). According to Ireland, achieving significant advancements in predictive accuracy would necessitate that internal heat transfer estimates meet an approximate accuracy level of 3%. Fig. 1.6 presents Cooling architecture of a modern gas turbine blade[28].

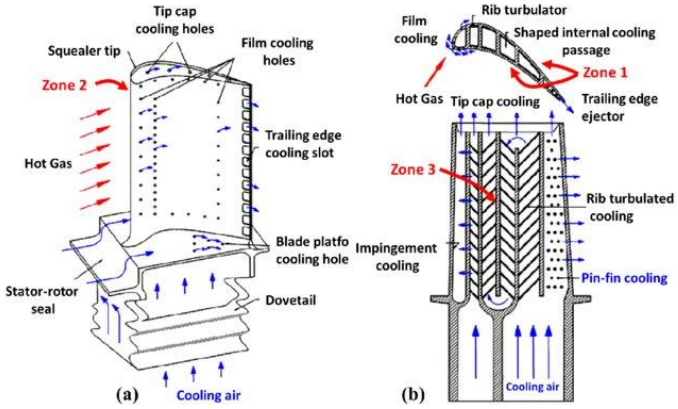

Fig. 1.6 Cooling architecture of a modern gas turbine blade. (a) External film cooling, (b) Internal impingement cooling and serpentine channel cooling [28].

1.3.2. Internal Cooling

Internal turbine blade cooling refers to the technique of circulating coolant, such as oil or water, through channels inside the blades of a turbine to remove heat. This method allows for more effective heat dissipation than external cooling methods, as the coolant is in direct contact with the blades [29]. The coolant is usually circulated through the blades using a pump and a network of internal channels. The coolant absorbs heat from the blades and then exits through a heat exchanger,

where it releases the heat to a secondary fluid, such as water or air, before returning to the blades. Internal cooling can be further divided into Active internal cooling and Passive internal cooling [30]. Active internal cooling is where the coolant is actively circulated by a pump, whereas passive internal cooling is where the coolant is circulated by natural convection. Internal cooling can significantly increase the efficiency and lifespan of the turbine, as it allows for higher operating temperatures and reduces thermal stresses on the blades [31]. However, it can also be more complex and costly to implement and maintain compared to external cooling methods. coolant flow rate, while still maintaining an acceptable pressure drop. This serpentine curved cooling channel design allows for a larger surface area for heat transfer between the coolant and the blade, which increases the cooling effectiveness [32]. The curved shape also helps to reduce the pressure drop, which allows for a higher coolant flow rate and better cooling performance. The serpentine layout also allows for a more uniform distribution of coolant throughout the blade, which helps to ensure that the entire blade is cooled evenly and prevents hot spots from forming. Additionally, this design is relatively simple, cost-effective, and easy to manufacture. This is why it is commonly used in turbine blade cooling systems [33].

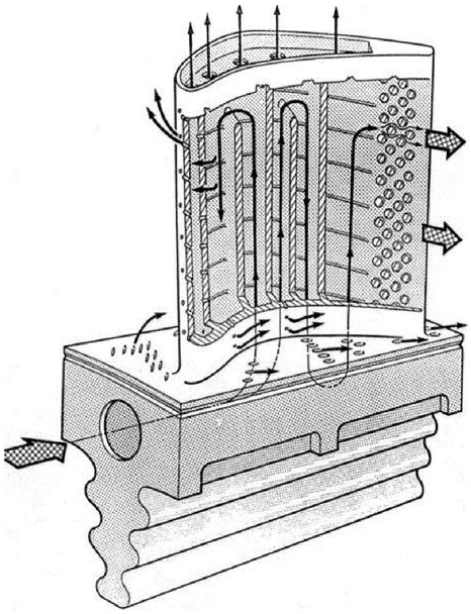

Fig. 1.7 Turbine blade/vane with an inside serpentine shape cooling configuration [32].

Fig.1.7 is the view of a turbine blade/vane with an inside serpentine shape cooling configuration that is industry standard [34]. The efficiency of a turbine is largely governed by its thermodynamic cycle, typically involving stages of compression, combustion, and expansion. Maximizing this efficiency is crucial for energy output and overall performance [33]. The serpentine shaped cooling channel design can achieve high cooling performance with a low coolant mass flow rate by utilizing a high heat transfer coefficient. The high heat transfer coefficient is achieved by increasing the surface area for heat transfer between the coolant and the blade using the serpentine shaped channels. These channels increase the contact area between the coolant and the blade, which allows for more efficient heat transfer. Additionally, the design of the serpentine channels also helps to promote a more uniform distribution of coolant throughout the blade, which helps to prevent hot spots from forming and ensures that the entire blade is cooled evenly. This technology is primarily focused on the bulk cooling of a single blade or component, rather than trying to cool specific areas or regions of the blade or component. one of the main challenges with bulk cooling is that it can result in non-uniform cooling and temperature distribution within the blade or component. This can lead to hot spots forming, which can potentially cause damage to the blade or component over time. Additionally, because the coolant flow is concentrated in one area, it can be difficult to distribute the coolant evenly throughout the blade, which can result in some areas of the blade not being cooled sufficiently. Another challenge with bulk cooling is that the heat transfer coefficients can be hard to measure or predict due to the complex fluid dynamics involved. The complex flow patterns and high velocities of the coolant can make it difficult to accurately measure or predict the heat transfer coefficients, which can make it difficult to optimize the cooling performance of the blade or component [35]. In addition, high fluid dynamics can also lead to increased pressure drop and higher pumping power requirement. These challenges have led to the development of advanced cooling techniques such as film cooling, transpiration cooling and conjugate heat transfer method. These methods are intended to improve the cooling effectiveness, to increase the cooling distribution and to provide a more uniform temperature distribution throughout the blade or component [33].

The aerospace industry is constantly researching and developing new technologies to improve the efficiency and performance of aircraft [36]. One area of focus is on developing more advanced cooling systems for engines and other components. Micro-cooled airfoils are one possibility being studied to simplify internal cooling systems and improve the overall performance

of aircraft. This technology uses small, precisely placed cooling channels to dissipate heat, rather than larger, more complex systems. It is thought that this could lead to significant weight savings and increased fuel efficiency for aircraft. Micro cooling entails distributing the cooling system in a succession of smaller and more widely distributed cooling channels, sub-channels, or elements, resulting in improved cooling homogeneity and lower in-plane thermal gradients [33] . The development of micro-cooled airfoils is an active area of research, and there are still many obstacles that need to be overcome before it can be implemented in aircraft. Some of these obstacles include optimizing the cooling channels, ensuring the proper function of micro-turbines, and addressing issues related to thermal management [37 - 46].These studies have focused on various aspects of micro-cooled airfoils, such as the design and optimization of cooling channels, the development of new materials and coatings, and the use of advanced computational simulations to predict performance. Despite the ongoing challenges, research in this area continues to make progress, and it is expected that micro-cooled airfoils will eventually be integrated into aircraft to improve their performance and efficiency [47].

Wang found that the optimization of the cooling channel design improved the thermal and structural performance of the turbine blades and vanes and reduced the cooling mass flow rate required [48]. The study showed that the use of Computational Fluid Dynamics (CFD) and evolutionary algorithms can be an effective method These algorithms are inspired by the process of natural selection and are particularly useful for solving complex optimization problems that may have multiple competing objectives or constraints [49]. This is used for designing and optimizing cooling systems for turbine blades and vanes. Overall, the study demonstrated that the cooling channel design plays a critical role in the performance and durability of gas turbine blades and vanes, and that optimizing the design can improve overall efficiency and reduce costs. The study used several RANS (Reynolds Averaged Navier-Stokes) turbulence models to help predict the performance of the cooling channels under different conditions [50]. The author also used a globally convergent method to optimize the cooling channels and achieve a high level of convergence. This research is one of the examples of the ongoing effort to optimize the cooling channels and improve the performance of gas turbine blades and vanes by using advanced computational methods [47], [51].

This study demonstrates the importance of using advanced techniques and models to optimize cooling passage designs to be able to improve the thermomechanical performance of turbine blades

and vanes. By using an evolutionary algorithm based on 2-D Analytical thermomechanical model, Wang was able to optimize the cooling channel design and reduce maximum temperature by up to 50 K. This highlights the importance of using advanced modeling and simulation techniques in the design process to ensure optimal performance and longevity of turbine blades and vanes [47], [52].

1.4. Different Internal Cooling Configurations

1.4.1. Radial Flow and Multi-Pass Serpentine Cooling

This type of cooling system is less efficient than more advanced designs and can lead to large temperature gradients between the airfoil surface and the cooling hole sites. The multi-pass serpentine cooling system is a more efficient solution as it cools the mid-body of the airfoil before being ejected out through the root or through main body film perforations or trailing edge slots. This type of cooling design allows for more effective cooling while still being cost and production efficient [53]. To address these issues, more advanced cooling systems such as the multi-pass serpentine cooling system have been developed. This system utilizes a serpentine shaped cooling channel that runs down the middle of the blade, allowing for more efficient cooling and reducing temperature gradients between the airfoil surface and the cooling holes. Additionally, this type of cooling system allows for the use of a lower coolant mass flow rate while still achieving a high heat transfer coefficient, resulting in improved overall cooling effectiveness. The multi-pass serpentine cooling system is a better cooling solution than the radial cooling hole arrangement [54]. This is because the serpentine cooling system allows for a more efficient and uniform distribution of coolant throughout the blade, resulting in a more consistent temperature gradient across the blade and a reduction in thermal stress on the material. Additionally, the serpentine cooling system allows for a higher coolant flow rate, which can further improve heat transfer and cooling effectiveness. Overall, the serpentine cooling system is a more advanced and effective cooling solution for turbine blades compared to the radial hole scheme. Fig. 1.8 depicts one such configuration. This multi-pass serpentine cooling system allows for more efficient cooling of the turbine blades as the coolant can circulate through multiple circuits, providing a more uniform cooling effect. Additionally, the use of film perforations or trailing edge slots allows for even greater cooling effectiveness. This type of cooling system is typically more complex and expensive to implement than radial hole cooling systems but is often necessary for high heat load applications or to prevent temperature gradients

in the blades [55]. Fig. 1.8 presents Schematic of serpentine passageways with many passes for internal cooling of turbine blades.

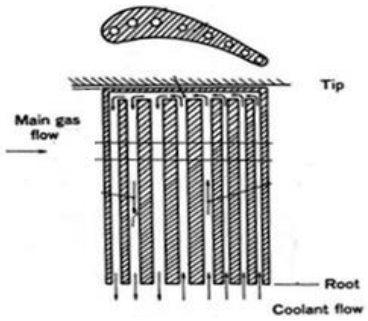

Fig. 1.8 Schematic of serpentine passageways with many passes for internal cooling of turbine blades [55]

1.4.2. Trailing Edge Cooling

Cooling concepts and methodologies are an important aspect of turbine blade and vane design, as each component has specific cooling requirements based on its function and the amount of heat it generates. Showerhead cooling is one example of a cooling method that can be used in turbine blades. This method involves directing coolant through small holes in the blade, which allows for efficient cooling of the blade surface. Other examples of turbine blade cooling methods include film cooling, impingement cooling, and transpiration cooling. Fig.1.9 depicts eight distinct cooling systems, including leading edge cooling holes. The cooling structure at the trailing edge of the vanes has impinged pin-fin slots and mid cord holes. Halila's E3 project intended to create an HPT configuration with high turbine efficiencies using a static and rotating construction and regulating the blade trip shroud clearances with an active clearance control system [56]. The author claims that this experiment also utilized cutting-edge cooling technology for the system's air-cooled blades and vanes.

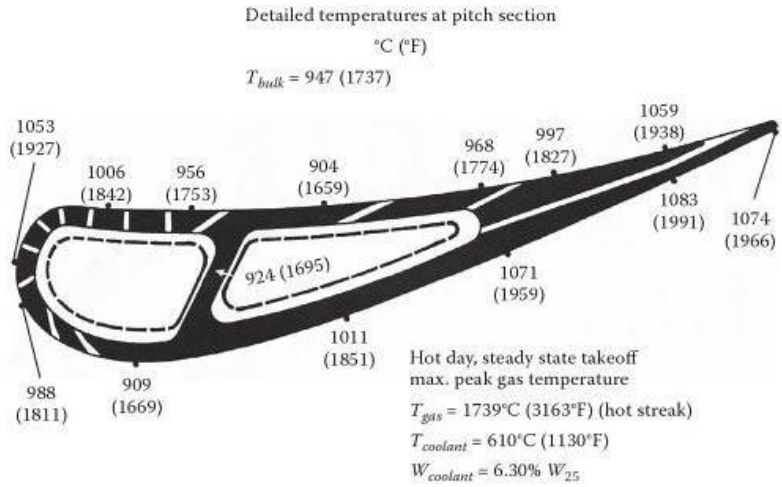

Fig. 1.9 Experiment on energy efficient engine (E3) showing the varying temperature for the 1st stage high pressure turbine vane [56].

This part of the turbine blade is frequently cooled by injecting a film of cooling air via slots on the pressure side of the blade close to the trailing edge. This technique helps shield the trailing edge from high temperatures by creating a cooling buffer between the hot mainstream gas and the airfoil surface. Cunha have emphasized the significance of the trailing edge heat transfer, underlining the necessity for efficient cooling methods and the significance of this area in turbine blade design [57]. Since the heat capacity of a tiny trailing edge mass differs from that of the other regions of the airfoil, a small trailing edge mass might cause a quick thermal response and the likelihood of cyclic loading, which can make it difficult to cool the area efficiently. The design approach used by Obata, the cooling performance of a closed return flow gas turbine blade that is internally cooled, which includes an analytical method for determining it, is likewise a significant contribution in this area. The findings of this approach demonstrated that the metal temperature remains constant along the blade chord, except for the trailing edge, where it decreases [55]. This methodology was proven to be suitable to superheated steam near saturation. Overall, the cooling of the trailing edge region of turbine blades is a complex and critical aspect of turbine design, and various methodologies and techniques have been developed to address the challenges and improve the cooling efficiency in this region.

1.4.3. Jet Impingement type From Multiple Jet

Metzger, [58] illustrates the use of multiple jets as a strategy to enhance thermal transfer away from the vane wall. It reveals that the heat transfer dynamics of multiple jets vary considerably compared to the impact of a single jet on a target surface [58], [59]. They determined that the Nusselt number, when dealing with multiple jets, is largely influenced by the Reynolds number rather than the distance between the jet and the target surface. This variation is attributed to the crossflow generated by spent jets. Fig.1.10 illustrates the count of jets employed to amplify thermal dissipation from the vane's wall. Metzger and his team found that the behavior of multiple jets contrasts markedly with that of a solitary jet interacting with a target surface [59]. They determined that the Nusselt number, in the context of multiple jets, is predominantly affected by the Reynolds number rather than the spacing between the jet and the target surface. The difference arises due to crossflows from exhausted jets. Studies show that the mass from a given jet moves laterally in the cross-jet flow, which in turn can impact the effectiveness of adjacent jets [60]. The crossflow aims to divert a jet away from the target plate where it is impinging. In cases of very strong crossflow and sufficient Fig. 1.10 A Turbine Vane Cross-Section with Impingement and Trailing Edge Pin-Fin Schematic The crossflow can totally divert the jet away from the impingement surface by cooling huge jet-to-target plate gap. Crossflow, according to Florschuetz, reduces overall heat transfer from the impingement surface [61]. They found that crossflow does augment convective heat transfer; however, this enhancement dwindles when the jets are diverted. The aggregate Nusselt numbers decline in scenarios with crossflow, as the boost provided by impingement jets substantially outweighs that of convective gains. Fig.1.10 illustrates a standard test setup employed by Florschuetz and colleagues. In the image, coolant jets contact the target surface in a straight-line arrangement emanating from the jet plate. The exhaust air from the jets positioned upstream influences the heat transfer coefficient profiles of those downstream. This impact intensifies as a greater volume of expended air accumulates on the surface under test [58], [62].

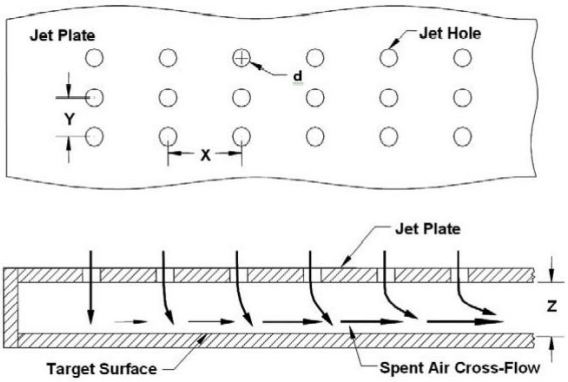

Fig. 1.10 typical test model used by Florschuetz et al [62].

1.5. Conjugate Heat Transfer

As the advantages of jet impingement cooling techniques and their enhanced heat transfer capabilities have been acknowledged, scholarly pursuits in this field have expanded. A focal point of this burgeoning research is conjugate heat transfer (CHT), which scrutinizes the thermal interplay between solids and fluids. This analytical framework broadens our comprehension of the thermal mechanisms at play in jet impingement type cooling, potentially paving the way for optimized cooling configurations in gas turbine blades.

Modeling CHT within the realm of Computational Fluid Dynamics (CFD) presents intricate challenges. A primary hurdle lies in the precise depiction of thermal and flow boundary layers on the object's surface. These layers are highly contingent upon the flow characteristics and the material's thermal attributes, aspects that are often elusive in CFD simulations. Moreover, the computational intensity required for accurate CHT modeling can be a constraint in terms of time-efficiency [63].

Despite these complexities, advances in computational techniques are emerging to enhance the precision and computational efficacy of CHT simulations within CFD environments. Such a comprehensive evaluation of an entity and its adjacent fluid dynamics offers a nuanced understanding of heat transfer processes in gas turbine blade cooling [64]. While considerable literature exists on various cooling configurations, empirical studies explicitly focusing on CHT are relatively limited. Hylton's 1983 investigation serves as seminal work in this domain,

employing CHT to unravel the complexities of heat transfer mechanisms in gas turbine blade cooling. His research incorporated simplified cooling channel designs and micro-cooling strategies, laying the groundwork for subsequent studies. Notably, NASA's assessment of the Mark II and C3X turbine blades—each equipped with ten radial internal cooling channels—has contributed significantly to the data pool on heat transfer under diverse flow conditions [51].

The objective of this initiative was to establish an empirical data repository that could aid in the development and assessment of two-dimensional boundary layer codes. These codes aim to forecast the internal heat transfer coefficient, and they also have potential applicability for film cooling predictions in airfoils. During the examination of blades and vanes, the findings confirmed that the Reynolds number significantly influences the overarching heat transfer rate. This conclusion relies on the mean internal heat transfer coefficient, which was calculated using round channel correlations tailored for individual cooling channel conditions and adjusted for thermally developed lengths. The scope of this research is somewhat restricted due to the straightforward nature of the internal cooling architecture and the confined range of experimental data gathered exclusively at the airfoil's middle surface. Despite its limitations, Hylton's work has served as a comparative standard in subsequent studies, helping to refine cooling channel designs in both turbine blades and vanes [51].

Wang conducted one of the studies stated above, using Hylton data to optimize, improve, and demonstrate the various layouts of micro-cooling channels[47], [51], [52], [65]. In another experiment, Mendonca utilized data from C3X turbine vanes to corroborate an unstructured finite volume methodology. This approach integrated flow dynamics, thermal conditions, and stress analyses for turbine blades, employing both Computational Fluid Dynamics (CFD) and Conjugate Heat Transfer (CHT) simulations [66]. Additional research has utilized Hylton's work as a standard for validating different Computational Fluid Dynamics (CFD) algorithms and turbulence frameworks. For instance, Facchini projected that the realizable $k{-}\epsilon$ model would outperform the standard $k{-}\epsilon$ model in ANSYS CFD simulations [67].On the other hand, employed Ansys CFD with the V2f and conventional k- model [68]. Finally, validated commercialized Fluent to evaluate both the standard and realizable k- models using several turbulence models to mimic Hylton [69]. The overwhelming conclusion drawn from the several investigations presented is that the V2f model predicted Hylton [51], [70]. The studies collectively attained a satisfactory alignment between predicted and observed surface temperatures on the pressure-facing aspect of the C3X

turbine vane. However, a noticeable trend of substantial deviations emerged between the measured and estimated temperatures on the vane's suction side. This pattern suggested that the current CFD algorithms and models encountered challenges in precisely predicting fluctuating boundary layer transitions. While multiple tests yielded temperature distributions across the airfoil's span, considerable inconsistencies were evident when juxtaposing these results [51].

The technique of conjugate heat transfer analysis is commonly employed to scrutinize thermal dynamics across diverse turbine parts and cooling configurations. This approach integrates both conductive and convective heat transfer mechanisms to offer precise estimations of temperature patterns within the hardware and the adjacent fluid medium [71-74]. In the cooling cavity of the turbine blade near the trailing edge, a cooling design featuring a trapezoidal cross-sectional shape, a wall with rib-induced roughness, and slotted openings on the opposing side is used for conjugate heat transfer analysis. Fig.1.11 depicts the rig arrangement utilized by [71].

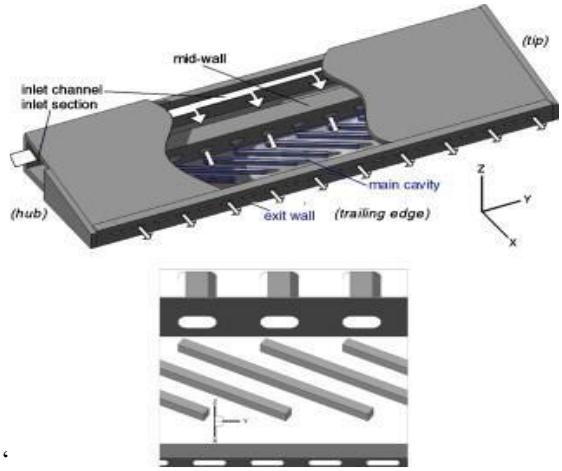

Fig. 1.11 Rig layout for rib CHT analysis a.) Full rig with highlighted sections b.) Rib setup [71].

Also defined the intake test section Re to 67,500 and imposed a uniform heat flux along the rib-roughened wall The researcher employed both infrared thermography and finite element methods to produce non-dimensional representations of temperature and Nusselt number (Nu) across the wall with rib-induced roughness. Subsequently, this thermal performance data was juxtaposed with convective metrics and earlier studies featuring an identical design [71].

2. STATISTICS AND INVESTIGATION OF CF6 JET ENGINES HOT SECTION FAILURES

2.1. Introduction

This chapter presents additional but related research that primarily investigates the performance of civil aviation aircraft engines, specifically focusing on CF6 engines used in boing B747 aircraft across various countries and climatic conditions. The results for this chapter were published in [75] .Utilizing actual data from engine performance tests and Borescope Inspections (BI), the study delves into the failure patterns of CF6 engines, particularly the High-Pressure Turbine (HPT) section. It offers a detailed statistical analysis of engine parameters, highlighting how deterioration affects engine efficiency and leads to reduced operational reliability and increased maintenance and cycle costs. A key focus is placed on the Exhaust Gas Temperature (EGT) margin, a crucial indicator of engine performance decline. The study extensively analyzes various engine parameters, including fan speeds, oil pressure and temperature, fuel flow, vibration, and EGT, to gain comprehensive insights. The BI reports provide an in-depth examination of the nature, size, and locations of cracks across different engine sections, such as the Low- and High-Pressure Compressors (LPC & HPC), Low- and High-Pressure Turbines (LPT & HPT), and the Combustion Chamber (CC). The study presents various graphs to elucidate engine parameter trends, such as engine thrust power and HPT temperature and pressure, related to the engine's total operational hours or Time Since New (TSN).

Furthermore, the study identifies factors contributing to power loss in engines with increasing TSN and proposes strategies to enhance engine performance.

2.2. CF6 Engine Models Configuration

The CF6 engine, drawing on the foundational design of the TF39 military engine used in the Galaxy C-5 military transport aircraft, benefited significantly from General Electric's experience with the TF39. This background allowed the CF6 to undergo extensive operational testing, resolving many early-stage issues through substantial flight hours under challenging conditions. The CF6 features a conventional two-shaft design. In this setup, the Low-Pressure Compressor (LPC) and Low-Pressure Turbine (LPT) are mounted on the same shaft as the intake fan. The High-

Pressure (HP) shaft, forming the first driving shaft, connects the High-Pressure Turbine (HPT) and High-Pressure Compressor (HPC). The second shaft, the Low-Pressure (LP) system, links the LPT, LPC, and the fan. This architecture classifies the CF6 as a twin-spool turbofan engine.

In this engine design, "cold air" undergoes additional compression and mixes with "hot stream air" exiting the turbine in mixed exhaust systems. Initially, the air is compressed in the fan. Both airflows are then combined in a mixer before entering the nozzle, ensuring they reach the same static pressure. This mechanism is depicted in Fig. 2.1, illustrating the general layout of the CF6 turbofan engine [76].

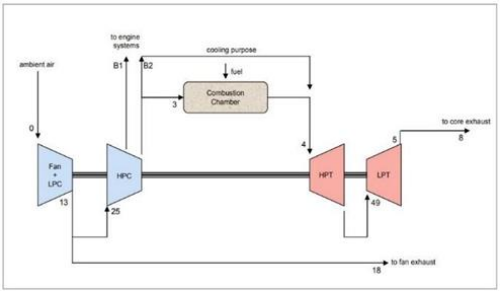

Fig. 2.1 Schematic of CF6 turbofan engine [76].

2.3. Engine Performance Analysis.

Throughout the analysis, a comprehensive range of engine parameters was meticulously examined, encompassing, but not limited to, factors like engine oil temperature, fan speed, oil pressure, vibration, Exhaust Gas Temperature (EGT), and fuel flow. The EGT margin is defined as the difference between the engine's highest permissible EGT, often referred to as the Redline EGT, and the peak EGT observed during take-off. It's crucial to note that exceeding the temperature threshold, or the Redline EGT, can lead to significant engine damage [77]. The examination of Borescope Inspection (BI) reports provides detailed insights into the characteristics, sizes, and positions of cracks in various engine components, including the Low-Pressure Compressor (LPC), High-Pressure Compressor (HPC), Low-Pressure Turbine (LPT), High-Pressure Turbine (HPT), and Combustion Chamber (CC). It's important to note that even particles of small diameter can lead to Foreign Object Damage (FOD). This type of damage contributes to the wear of engine parts,

diminishing efficiency. Consequently, there is an increase in Exhaust Gas Temperature (EGT) due to higher fuel consumption, which is necessary to sustain the requisite performance level of the engine [78]. Foreign Object Damage (FOD) typically occurs when objects are dislodged from aprons, ramps, and runways by the landing gear, as well as through the engines' thrust reverser and inlet-vortex, particularly during taxiing, take-off, and landing. This is often referred to as ground-vortex. To mitigate FOD, the industry implements various organizational and design strategies. Key among these is the provision of risk awareness training for ground personnel. Additionally, the development of suitable methodologies for take-off and landing is essential in protecting engines from FOD.

2.4 EGT& EGT Margin Monitoring

The Take-off Exhaust Gas Temperature Margin (EGTM) serves as a crucial measure of durability and operability. It signifies the difference between the actual (uncorrected) Exhaust Gas Temperature (EGT) readings for a specific take-off scenario and the maximum EGT limits set by the engine manufacturer, commonly referred to as the redline [79]. Engine manufacturers aim to set specific Exhaust Gas Temperature (EGT) thresholds, commonly referred to as the redline. These limits are crucial as they factor in the potential degradation of the engine's hot section metal parts. For instance, the resistance of turbine blades and other rotating components to creep and stress fractures can halve with every 500K increase in temperature. Consequently, exceeding these temperature limits might necessitate additional inspections or even premature engine removal.

Fig. 2.2 illustrates the relationship between EGT at take-off and the take-off thrust for CF6 engines used in B747 aircraft across different regions. It highlights the varying conditions of these engines. For example, engine number four exhibits the highest EGT during take-off, coupled with a take-off thrust that is significantly lower than normal. Borescope Inspection (BI) reveals that this engine has defects in the Combustion Chamber (CC), as shown in Fig .2.5, and in the High-Pressure Turbine (HPT) section, particularly in Stage one, as depicted in Fig. 2.8. In contrast, engine number seven shows the highest take-off thrust and a normal take-off EGT. The BI for this engine reveals that in the HPT Stage one, three blades have partially missing coating.

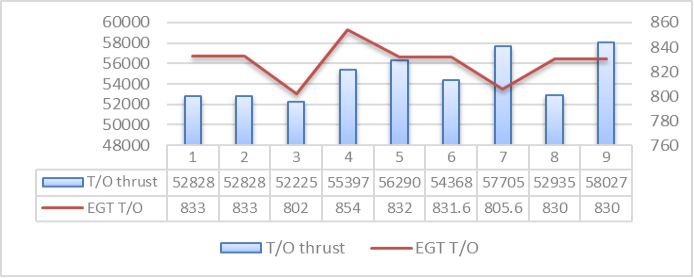

Fig. 2.2 EGT to thrust rating relation.

Furthermore, one blade was observed with 70% of its coating missing. However, unlike engine number four, no cracks were detected in this instance. On the Nozzle Guide Vanes (NGV) of the High-Pressure Turbine (HPT) stage 1, an inspection revealed a vane with a burnt spot on the trailing edge, accompanied by an axial crack and material loss, as shown in Figs. 2.6 and 2.7. Additionally, the Dome Assembly and Spectacle Plate of the combustor exhibited several splash plates with chipped areas (Fig.2.5). The analysis of these findings indicates that these issues are the primary causes of thrust loss in this engine. High EGT is a key factor in the development of these defects. Sources of high EGT, such as cracks, coating loss, and burning spots, directly impact the HPT NGV and turbine blades, which show cracks around the cooling holes (see Fig. 2.8).

Improvements in the materials used for turbine blades and enhancements in the cooling channels of the turbine blades could significantly reduce temperatures, thereby boosting engine performance and reducing maintenance costs. Subsequent figures provide a comparison of 17 CF6 engines operating in different time zones, with varying Total Service Numbers (TSN), cycles, and take-off Exhaust Gas Temperature Margins (EGTM). From this analysis, it was noted that engine number 8 exhibited the lowest EGTM relative to the other engines, despite having the highest CNC, as illustrated in Fig. 2.3.

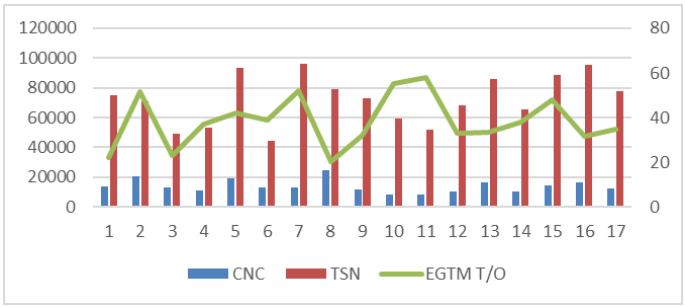

Fig. 2.3 EGT Margin to engines life relation.

2.4. Engine Operation and Maintenance

The average time When a new airplane engine model is integrated into an airline's fleet, one of the initial considerations is the average duration (measured in hours/cycles/calendar days) between refurbishments or overhauls of the High-Pressure Turbine (HPT) T-1 blade. Common practice among airlines is to schedule early overhauls for new engine models, typically around 10,000 hours of operation. For instance, as airlines gain experience and confidence with a particular engine type, the interval for the first refurbishment of these engines can extend up to 22,000 hours. Subsequent runs, or second-run engines, often achieve approximately 15,000 hours in service before requiring overhaul. During the overhaul, the engine's hot section is usually the primary focus. The typical cycle-to-hour ratio varies from one airline to another, influenced by the nature of their operations. For short-haul flights, each cycle tends to last between 1 to 4 hours, whereas long-haul or coast-to-coast flights in continental zones often exceed 4 hours per cycle. Other airline operations might average between 6 to 13 hours per cycle. These metrics are crucial in planning the overhaul process. It’s observed that engines operated in shorter cycles tend to exhibit more wear and tear in the hot-section parts compared to those used in longer cycles. This suggests that the deterioration of these components is more dependent on the number of cycles than the total operating time [80], [81].

2.5. Analysis of CF6 engines based on Borescope Inspection (BI)

Borescope Inspections (BI) are a primary tool for conducting preventive maintenance on key engine components like the compressor, turbine, and Combustion Chamber (CC). This method

plays a crucial role in managing the lifespan of an engine. Statistical data indicate that BI identifies 90 percent of the instances requiring unscheduled engine replacements. Alongside routine inspections of the entire engine, BI is a vital method for diagnosing various engine issues, including problems related to engine vibration, surges, and shifts in engine capabilities and performance. Given its significance in detecting and addressing potential issues, placing a strong emphasis on the effective management of Borescope Inspections is essential to ensure the safe operation of engines [82]. Several key factors significantly impact the functional performance of engine structural components, particularly influencing the deterioration rate of the hot section parts of engines. These factors include:

- Abrasion of the blade's Leading Edge (LE) due to environmental factors like sand and dust.
- Erosion resulting from blockages in the internal cooling gas flow passages.
- Chemical corrosion, often caused by specific air compositions, including dust and oceanic environmental elements.
- The engine thrust rate and the value of thrust derate.
- The ratio of the passage area in the gas-air path.

The operational environment often plays a decisive role in affecting these components. Additionally, variations in the management approaches between domestic and international civil aviation industries necessitate adjustments in the Borescope Inspection (BI) schedule to prevent in-flight engine failures.BI reports provide detailed insights into the behavior, dimensions, and locations of cracks in different sections of engines, such as the Low-Pressure Compressor (LPC), High-Pressure Compressor (HPC), Low-Pressure Turbine (LPT), High-Pressure Turbine (HPT), and Combustion Chamber (CC). Beyond monitoring and analyzing engine events related to BI, further research is essential to understand the progression of all types of defects, considering the likelihood and prevalence of structural defects in engine components. This research should inform the scheduling of BI intervals. Typically, hot section parts like the CC and HPT blades, as well as the guide vanes of the HPT and LPT, tend to expand over time. In contrast, initial damages in colder section parts like the HPC are less likely to exhibit such expansion. The analysis of BI reports for CF6 engines installed in B747 aircraft is a critical component of this ongoing assessment and maintenance process, the analysis results are described in the following subchapters (2.5.1 – 2.5.6).BI of the LPC, HPC, CC, LPT and HPT is required to detect On Condition Defects and special defects. If any defects are discovered, they must be observed and evaluated in relation to

the applicable hardware serviceability limits.

2.5.1. Low Pressure Compressor Borescope Inspection

The results from Borescope inspection (BI) test show that within the limits of the Low-Pressure Compressor (LPC), it's essential to conduct conditional defect assessments to forecast future deterioration rates. These conditional defects include a range of issues, such as tears or cracks, scratches, nicks, dents, tip curling, erosion, pits, distortions in trailing or leading edges, and loss of metal. Additionally, certain specific inspection requirements are linked with unique defects. For instance, issues like Foreign Object Damage (FOD), fan stalls, potential bird strikes, and pronounced fan vibrations often occur in engines that have experienced problems necessitating specialized inspections.

It's noteworthy did not identify any critical defects in the LPC during their assessment. This observation is significant in understanding the overall health and operational readiness of the engine's low-pressure compressor.

2.5.2. High Pressure Compressor Results

Borescope inspection results show that the defects encompass the same types of defects as those found in the Low-Pressure Compressor (LPC). Additionally, certain specialized defects are associated with specific inspection requirements. These include issues such as the presence of oil fumes or core stall detected in cabin air, high core vibration, and Foreign Object Damage (FOD). Such defects are typically identified in engines that have experienced issues necessitating specialized inspections. In the analysis of available Borescope Inspection (BI) data for a set of CF6 engines, the authors were able to identify specific anomalies. They noted four blades exhibiting minor tip curling on the leading edge (LE), and two blades showing signs of blend repair. These observations are detailed in Fig. 2.4(a), providing visual evidence of the identified defects.

(a)Stage one. **(b) Stage Eight** **(c) Stage Nine**

Fig. 2.4 HPC stages

In stage 8, One blade with small nick and one blade with minor dent on LE (see Fig. 2.4 (b)). In Stage 9 one blade with minor dent on LE see Fig. 2.4 (c).

2.5.3. Combustion Chamber Borescope Inspection Analysis Results

The defects identified in the Combustion Chamber (CC) include noticeable discoloration of the inner liner. Additionally, specific defects arise from evidence of overheating and impact damage affecting the High-Pressure Turbine (HPT) rotor blades. Observations also included the Dome Assembly & Spectacle Plate, where several splash plates were found to have chipped areas. These findings are illustrated in Fig. 2.5(a), providing a visual representation of the mentioned defects.

(a) (b) (c)

Fig. 2.5 Combustion Chamber (Dome Assembly &Spectacle Plate)

The examination of the Inner and Outer Combustion Liners revealed the presence of multiple axial cracks. These cracks were generally less than half the length of the panel. Additionally, one notable crack on the inner liner was observed to be 1½ times the length of the panel. It's important to note that there were no more than 30 cracks on every single panel for each liner. These specific findings are visually documented in Fig. 2.5(b) and (c), providing detailed illustrations of the observed defects.

2.6. High Pressure Turbine Nozzle Guide Vanes Borescope Results

When assessing turbine engines 'on condition', various defects are considered, encompassing issues such as discoloration, burns, and cracks, along with obstructions in cooling air passages. Additionally, particular attention is given to special defects including instances of over-temperature operation, engine stalls, and significant increases in the trend of Exhaust Gas Temperature (EGT).

These defects are crucial indicators, signaling potential operational and safety concerns within the engine. [83]. In the HPT Stage 1 Nozzle Guide Vanes, an inspection identified a vane exhibiting a burned spot on the trailing edge, accompanied by an axial crack and material loss. This condition is deemed serviceable according to the guidelines outlined in AMM Subtask 72-00-00-206-001-J00, as referenced in Table 618` [84]. The Thermal Barrier Coatings (TBC) were observed to be partially missing on the trailing edges and platforms, as detailed in Fig. 2.6.

(a) (b) (c)

Fig. 2.6 HPT stage 1 nozzle guide vanes.

For the High-Pressure Turbine (HPT) stage 2 Nozzle Guide Vanes, it was noted that one vane had a minor burned spot on the trailing edge (TE). Additionally, there was a partial absence of Thermal Barrier Coatings (TBC) on all vanes, as depicted in Fig. 2.7.

2.7. High Pressure Turbine Borescope Results

'On Condition' defects for turbine engines typically encompass a range of issues, including but not limited to: cracks on the trailing edges (TE) that may appear curled, bent, or fractured; wear on the tip zone such as trailing edge wear or missing pieces; issues with the blade platform like cracks, distortion, or damage; as well as cracks or burning on both the convex and concave surfaces of the airfoil. Additionally, defects can include the obstruction or plugging of cooling channels within the blades.

(a) (b)

Fig. 2.7 HPT stage 2 nozzle guide vanes

Additionally, certain specialized inspection requirements are associated with unique defects, including core stall (N2), overheating, metal presence in the tailpipe, N2 overspeed, core vibrations, and hard landing impacts. Engines exhibiting these specific issues typically require special checks and ongoing monitoring due to the prevalence of such defects [83].

In the High-Pressure Turbine (HPT) Stage 1 Blades, there are several blades where the coating is partially missing. Notably, one blade has 70% of its coating missing, as shown in Figure 2.8. The inadequacy of the coating in offering sufficient oxidation protection leads to significant over-aging of the blade's substrate material during its service life.

(a) **(b)**

Fig. 2.8 HPT Stage 1 Blades.

2.8. Borescope Inspection Summary

Table 2 presents a statistical analysis encompassing various types of failures and their locations, based on Borescope Inspections (BI) conducted on numerous CF6 engines installed in B747 aircraft. These engines have operated under varying cycles, hours, and in different geographical zones.

The analysis reveals that the first stage turbine blades typically have an average lifespan of

72,000 hours. It is recommended that these blades undergo repairs after every 24,000 hours of operational life. During these maintenance sessions, routine procedures are carried out on the blades, which include cleaning the cooling holes, reapplying Thermal Barrier Coatings (TBC), and refurbishing areas on the non-pressure sides of the blades.

The TBC process involves the application of two distinct layers. The 'bond coat' serves as the inner layer, providing resistance to oxidation and corrosion, while the 'top coat' is an insulating ceramic layer that forms the outer surface of the coating [81], [85].

Table *2*

Statistical analysis for different failure types and locations for CF6 engines.

Location / Type of defect	LPC	HPC	C.C	LPT	HPT Nozzle	HPT
Tip curl	0	5	0	0	0	1
Blended blade	1	6	0	2	0	0
Nicks	0	7	0	0	0	0
Minor dent	0	8	9	0	0	0
Cracks	0	2	0	0	0	5
Missing martials	0	1	0	0	1	0
Deformation	0	0	4	0	1	4
Burning spot	0	0	4	0	1	5
Coating missing	0	1	9	1	1	9
Erosion	0	0	0	1	0	6
Tip corner	0	0	0	0	0	1

Analysis of Table 2 led the authors to determine that the High-Pressure Turbine (HPT) section, particularly in stage one, is the most defect-prone area of the engine, specifically concerning the turbine blade and Nozzle Guide Vanes (NGV). The Borescope Inspection (BI) of the HPT revealed various types of defects including cracks, burning spots, missing coatings, and erosion on the stage one turbine blade, as depicted in Figs 2.6, 2.7, and 2.8.

Additionally, the High-Pressure Compressor (HPC) section exhibited its own set of issues, including blended blades, nicks, and some cracks. The BI reports highlighted that the most critical

defects, especially the cracks, were predominantly located between the cooling channels of the turbine blades. This observation led the authors to conclude that enhancing these cooling channels could significantly reduce the temperature of the turbine blades, thereby lowering maintenance costs and enhancing engine performance.

2.9. Summary Of Chapter 2

The utilization of real data from engine performance tests and Borescope Inspection (BI) reports enabled the authors to conduct an in-depth analysis of failures in CF6 engine sections, focusing primarily on the High-Pressure Turbine (HPT) section. This analysis included a statistical review of engine parameter behavior and degradation. Monitoring the Exhaust Gas Temperature (EGT) and EGT margin of CF6 engines across various climatic zones facilitated an examination of the relationship between take-off EGT and thrust in B747-400 aircraft. This revealed differing conditions among these engines. A comparative analysis of the take-off EGT Margin (EGTM) for 17 CF6 engines with varying life cycles, based on BI data, was also performed. The authors identified that the most prevalent defects in the engine were located around the HPT section, particularly in stage one turbine blade and NGV. The BI of the HPT showed evidence of cracks, burning spots, missing coatings, and erosion in the stage one turbine blade. The combustor and HPT were identified as critical components affecting engine performance due to their sensitivity to defects.

Based on these findings, the authors proposed several suggestions for improvements:

1. Enhancing the cooling channels in turbine blades and the HPT nozzle could reduce fatigue and temperature, necessitating a redesign of the cooling channels.
2. The combustor, especially its Dome Assembly and Spectacle Plate, requires advancements to better control the flame, thereby preventing cracks that directly impact engine performance.
3. To increase turbine reliability, the implementation of advanced prognosis and health monitoring systems is essential. These systems would anticipate the remaining life of turbine blades and discs, with a particular focus on fracture-critical areas, to prevent catastrophic failures.

3. COMPUTATIONAL FLUID DYNAMICS ANALYSIS OF FLOW CHARACTERISTICS AND HEAT TRANSFER VARIATIONS IN MULTIPLE TURBINE BLADE COOLING CHANNELS

The body of this chapter, and results were published in [86].

3.1. Introduction

The Gas turbine blades have endured prolonged exposure to abrasive high-temperature gases in challenging environments. Presently, advanced gas turbines operate with inlet gas temperatures exceeding 1600 degrees Celsius, surpassing the material's permissible limits [87]. The future advancement of gas turbines will inevitably involve even higher gas temperatures. Therefore, the research and development of cutting-edge and efficient cooling technologies for turbine blades hold significant importance. These innovations aim to safeguard gas turbine blades and subsequently reduce maintenance expenses. In recent years, researchers have shown a strong interest in dimple and protrusion structures due to their efficiency and low resistance characteristics. [88] conducted a study on the turbulent friction and thermal transmission properties of channels featuring dimples. [89] conducted experiments to explore the impact of Reynolds number on channels with teardrop-shaped and spherical dimples. [90] examined enhanced heat exchange and resistance performance in channels featuring a single-sided socket structure [91] and investigated the effects of Nusselt number and dimple depth on channel behavior. delved into the comprehensive performance of channels with dimple configurations and V-shaped ribs. [92] focused their research on the influence of suction holes and dimple structures on the flow characteristics within a U-shaped channel.

Blade malfunctions stemming from cooling inadequacies can severely compromise both the efficiency and dependability of gas turbine engines [83]. Elevating the inlet gas temperature can maximize the energy harnessed from combustion, thereby boosting the engine's efficiency. However, this temperature increase also subjects the turbine blades to heightened stress, impacting their resilience and longevity [93]. Consequently, there is an industry-wide push to use materials with superior heat tolerance and cutting-edge cooling solutions to maintain the blades under secure operational conditions.

The goal is to find the ideal equilibrium between enhanced operating temperatures and secure

functionality [79], [81].Cooling-related issues can emanate from various factors, including obstructed cooling channels, suboptimal flow rates, or unsatisfactory coolant temperatures. These can culminate in the blades overheating, which may lead to their failure. A compromised blade can, in turn, inflict damage on additional engine parts, distort airflow, and induce imbalanced rotations—potentially resulting in catastrophic engine failure [75]. However, to counter these issues, meticulous cooling system design and maintenance are indispensable. Sophisticated cooling setups, computational optimization techniques, and Conjugate Heat Transfer (CHT) analyses are increasingly being deployed to tackle the complexities induced by rising turbine inlet temperatures. Such advanced cooling systems aim for a nuanced balance—adequate blade cooling without performance-efficiency trade-offs [71].Optimization algorithms guide the search for the most effective cooling strategies, supported by numerical simulations [70]. CHT analyses contribute to a deeper understanding of intra-blade heat transfer, thereby informing improvements in cooling configurations. By synergizing these multiple approaches, professionals in the gas turbine sector are better equipped to design cooling mechanisms that proficiently manage elevated temperatures while preserving engine safety and reliability. While existing literature abounds with research focusing on the architecture of blade cooling channels, there is a noticeable gap in studies that concurrently examine turning vanes and variable cross-sectional attributes. This study addresses this gap by selecting a cooling channel with varying different cross-sections as its baseline model. Sourced from an actual gas turbine blade NASA C3X, this model incorporates protrusion structures on its surface. The investigation includes a comprehensive analysis of flow dynamics, heat transfer, and resistance features for channels equipped with different designs of cooling channels. In the scope of this research, ANSYS FLUENT was employed for Computational Fluid Dynamics (CFD) solving, while mesh creation was facilitated through ANSYS ICEM-CFD. The latter was specifically chosen for its capability to produce highly accurate and precise meshes compatible for CFD analyses. Collectively, these software tools enabled us to execute in-depth and precise CFD simulations focused on the cooling setups within the gas turbine blade (NASA C3X). MATLAB algorithms were used for comparison between reference experiment data and simulation results. Despite the critical nature of this issue, existing literature scarcely addresses cooling channels that incorporate factors like variable cross-sectional attributes and rotational effects. In this study, Computational Fluid Dynamics (CFD) and numerical methodologies were employed to scrutinize the efficacy of three distinct cooling channel models characterized by variable cross-sectional

features. In this research, three unique cooling channel designs U-bend, Net-type, and Jet Impingement type were developed and subjected to a detailed performance analysis across Reynolds numbers ranging from 10,000 to 60,000. The findings indicated, as R_e continues to rise, heat transfer efficiency notably improves, leading to a corresponding increase in Thermal Performance (TP). Within the lower R_e range (10,000 to 30,000), when the Reynolds Number (R_e) is at 10,000, the TP in Net cooling channel (case 2) sees an improvement of 3.5%. However, an overly thick internal channels net can result in significant friction losses. In the R_e range of 20,000 to 30,000, Net cooling channel (case2) doesn't perform as well in terms of Thermal Performance (TP) as (case1) does. Jet impingement type (Case 3) showed better thermal performance at R_e 20,000 with 11.27 % than U bend cooling channel (Case 1). This leads to a gradual outperformance of jet impingement (case 3) in TP compared to other channel configurations. Based on these observations, it can be projected that Jet impingement type cooling channels (case 3) will offer the most balanced thermal performance when R_e exceeds.

3.2. Methodology

The core objective of the present study is to engineer a state-of-the-art design for cooling channels in turbines, targeting a considerable augmentation in thermal efficiency and cooling efficiency, coupled with a reduction in drag forces. Utilizing cutting-edge Computational Fluid Dynamics (CFD) models and empirical analyses, the study aspires to establish a channel configuration that is versatile across an extensive range of Reynolds Numbers and diverse flow regimes. A key focus of this investigation lies in an exhaustive examination of the fluid dynamics at various critical segments within the cooling channels, such as bends and junctions, with the intent to pinpoint zones requiring optimization. MATLAB algorithms are deployed for data processing, allowing for rigorous computational analysis and comparative evaluation based on experimental findings. Table 3 presents the three different designs of the cooling channel specifically designed for this study.

Table 3

Cooling channel designs.

Case 1	U bend cooling channel
Case 2	Net Cooling Channel
Case 3	Jet impingement type cooling channel

3.3. U Bend Cooling Channel (Case 1)

The main goal of this design was to cover a wide area in the trailing edge. A diameter of 6.3 mm from the original NASA C3X cooling channel was adopted as in [51]. As suggested by Hylton a modified 20 mm U bend from the original channel with a bend angle 129.5^{o}, and symmetry were also applied for the full entire length of 76.2 mm as seen in Fig. 3.1 [51]. The main focus here was to increase the angle in u bend, so as to help minimize pressure drop and the drag. The geometrical turbine cooling channel design was created using ANSYS Workbench.

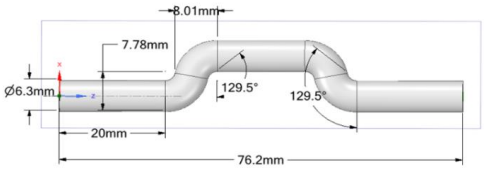

Fig. 3.1 . U-bend model configuration

The cooling channel geometry and computational domain for mesh generation for this case was created. Fig. 3.2 presents the geometry before meshing and shows the computational boundaries selected for this U bend geometry.

Fig. 3.2 3D U-bend model flow domain

The size and properties of a smooth channel with known reference experimental data were chosen to analyze the hydrodynamic and heat transfer characteristics through a straight channel [94].

The Mesh used in carrying out for this model, had the following properties: bounding length (14.44, 6.3, 76.2) mm, and a total volume of 2589 mm2. One control volume was selected, and a mesh was created using CFD.

Since transport phenomena for momentum and other scalar quantities are most prominent in regions close to the wall, where solution variable gradients are larger. In this thesis, therefore, the inner layer was considered and was divided into three zones, each characterized by its respective non-dimensional distance, known as the wall Y+ value. This value is analogous to the local Reynolds number. Specifically, the viscous sublayer corresponds to Y+ values below 5, the buffer or transitional layer ranges from 5 to 30, and the fully turbulent layer 30 and 60. For the purposes of this study, a viscous sublayer was assumed by selecting a Y+ value of 1. Air serves as the fluid medium for this investigation, with a density of 1.229 kg/m3 and a viscosity of 0.0000173 kg/ (m.s). The normal wall distance, denoted as Y, was calculated using eq (4.1):

$$Y = \frac{Y^{+}\nu}{u_{\tau}} \tag{3.1}$$

Where ν – presents fluid viscosity, *kg/ (m.s);*

u_{τ} – presents the friction velocity and it can be calculated with:

$$u_{\tau} = \sqrt{\frac{\tau_w}{\rho}} \tag{3.2}$$

Where $\boldsymbol{\rho}$ – is the density, kg/m^3;

τ_w – presents the wall shear stress which can be calculated with:

$$\tau_w = 0.5\, C_f \rho\, u^2 \tag{3.3}$$

Where C_f – is Skin friction coefficient.

$$C_f = \frac{0.058}{R_e^{0.2}} \tag{3.4}$$

Where R_e – is Reynolds number.

The above equations from (3.1- 3.4) were used to calculate the normal distance to the wall which is 0.00213 mm. Mesh inflation was done using normal distance to wall as the thickness of

first layer, 10 layers were chosen, and rate of growth is 1.35. Mesh contained 3962979 node, and 969878 elements as seen in Fig. 3.3 presents the mesh configuration, and Fig.3.4 presents the inflation layers.

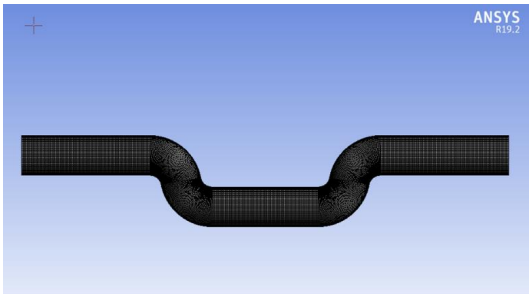

Fig. 3.3 3D u bend mesh configuration

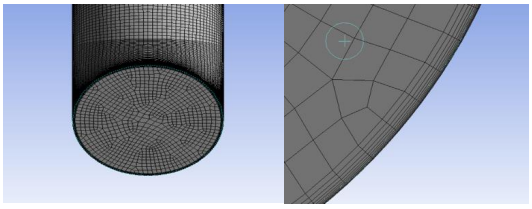

Fig. 3.4 3D U-bend inflation layers

The aspect ratio of mesh elements emerges as a critical variable in the pursuit of reliable and efficient CFD analyses. Its influence extends to the credibility and precision of the simulation's numerical outcomes. Hence, meticulous attention to this aspect ratio is indispensable, more so in specialized applications such as the cooling channels in turbines where exactitude is paramount. In this context, Fig.3.5 presents the aspect ratio, providing empirical evidence written for its pivotal role in the computational study.

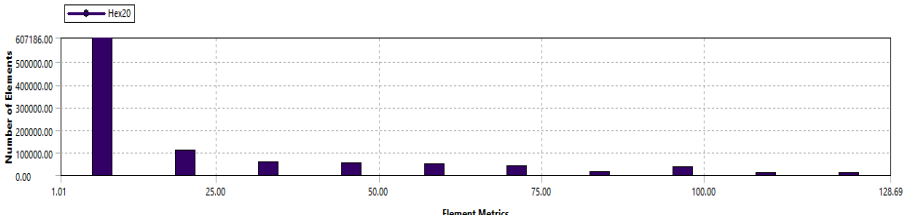

Fig. 3.5 U bend mesh element aspect ratio

3.4. Net Bend Cooling Channels Design (Case 2)

The core design principle aims to broaden the cooling coverage around the trailing edge of the turbine blade. Utilizing the original NASA C3X cooling channel diameter of 6.3 mm as a [1], design features of three net channels strategically positioned between every two existing channels [51], [70]. The design also integrates symmetry and has an overall length of 76.2 mm. Within this framework, two Net type channels each have a width of 5.2 mm, while the middle channel is slightly narrower at 4.2 mm, as illustrated in Fig. 3.6. The key advantage of this layout is the enhanced surface area available for cooling. To bring this design concept to fruition, computational modeling was performed using ANSYS Workbench.

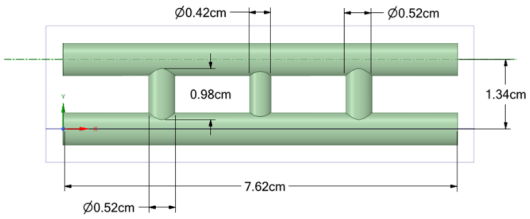

Fig. 3.6 Net bend optimized model.

The size and properties of a smooth channel with known reference experimental data were chosen to analyze the fluid dynamics and heat transfer characteristics through a straight channel. The size and features of the smooth channel were obtained from the previous study's [62] experimental investigation and was employed in this study.

The three-dimensional unstructured meshing was used to mesh the designed channel. Mesh carried out for this model, was done using the properties i.e., bounding length (14.44, 6.3, 76.2) mm and total volume 2589 mm2. The mesh was created using ANSYS ICEM. An element size of 0.5 mm for this case was chosen to provide more accuracy for the flow conditions. Equations 3.1 to 3.4 (mentioned above) were used to calculate the normal distance to the wall, which gave a result of 0.00213 mm. Mesh inflation was also performed using normal distance to the wall as thickness of the first layer, with 10 layers, and a growth rate of 1.2. Mesh contained nodes 116291, and 264386 elements, as seen in Fig. 3.7 presents the mesh configuration, and Fig. 3.8 shows the inflation mesh layers.

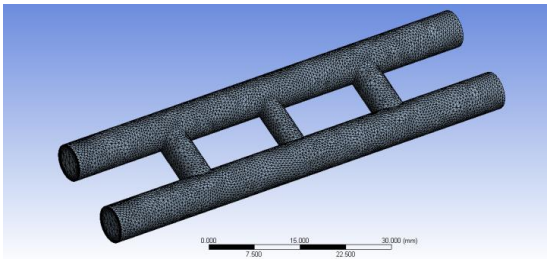

Fig. 3.7.Net channels mesh configuration.

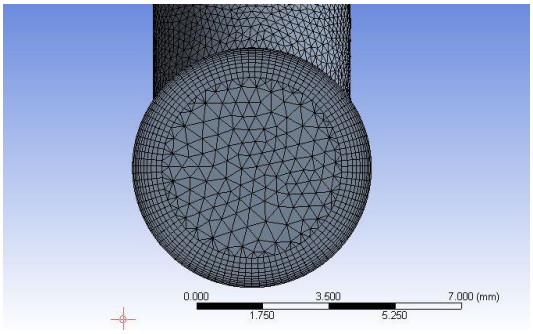

Fig. 3.8 Inflation mesh layers.

The mesh element's aspect ratio is a key factor in achieving accurate and trustworthy CFD simulations. Its role is crucial in determining the validity and exactness of the numerical results generated by the simulation. This is especially critical in specialized for cases like turbine cooling channels, where high precision is essential. Fig. 3.9 offers a detailed evaluation of the mesh quality by representing the aspect ratio graph, manifesting reliability of the computational analysis.

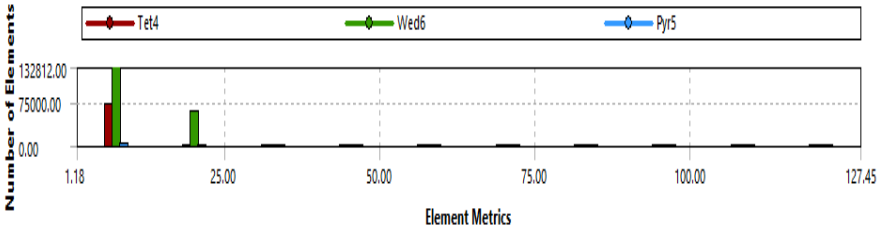

Fig. 3.9 Mesh aspect ratio quality for net channels

Fig. 3.10 illustrates the mesh independence criteria, depicting the relationship between mesh element size and velocity across various mesh configurations. A trend of progressive increase in velocity with increasing mesh density can be seen till mesh size of 264386 elements, where the velocity is 161 m/s. After this point the velocity curve becomes uniform and the variations with respect to the mesh elements are insignificant. Therefore, after suggested value from the mesh independence analysis, 264386 number of elements were used for the CFD analysis.

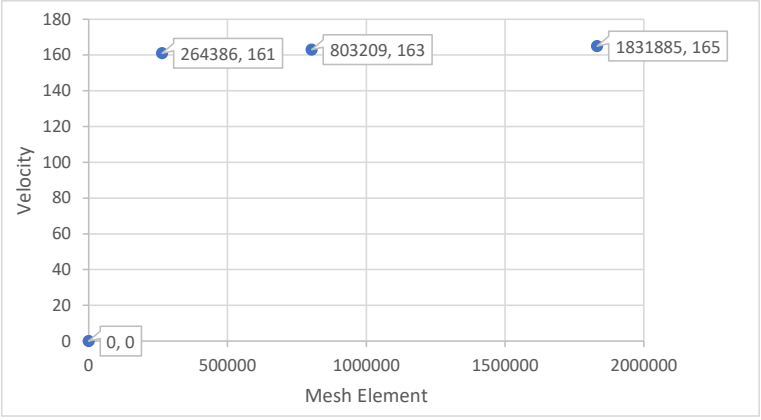

Fig. 3.10 Mesh independence criteria between mesh elements and velocity at different mesh element configuration.

3.5. Jet Impingement type Cooling Channels Optimization (Case 3)

The focus of this study was to enhance the cooling effectiveness of gas turbine components using an optimized jet impingement type cooling channel. The study yielded promising outcomes, specifically an improved heat transfer coefficient and a reduced blade leading edge temperature, without causing a notable increase in pressure drop. This underscores the significance of precisely selecting jet impingement type variables in cooling system designs for gas turbine elements. By retaining the mesh structure from the foundational model and incorporating insights from Glynn's research [95], it was confirmed that reducing the diameter of the channel jet nozzle can significantly enhance heat transfer. Additionally, this doctoral thesis adheres to Yamane's [93] guidelines on optimal nozzle Height-to-Diameter (H/DJ) ratios, which should range between 2 to 8. For this study, a jet diameter of 1.94 mm was selected, yielding a H/DJ ratio of 8, aligning well with Yamane's suggested parameters. Furthermore, the jet Spacing to Jet Diameter (S/DJ) ratio was

maintained between 4 and 8, with a selected jet spacing of 11.44 mm, resulting in an S/DJ ratio of 5.89. So, utilizing the ANSYS Workbench, the channel geometrical design was created, and this optimized design was carried out with five jet channels. Fig.3.10, and Fig. 3.11 present Jet impingement type cooling channels configuration.

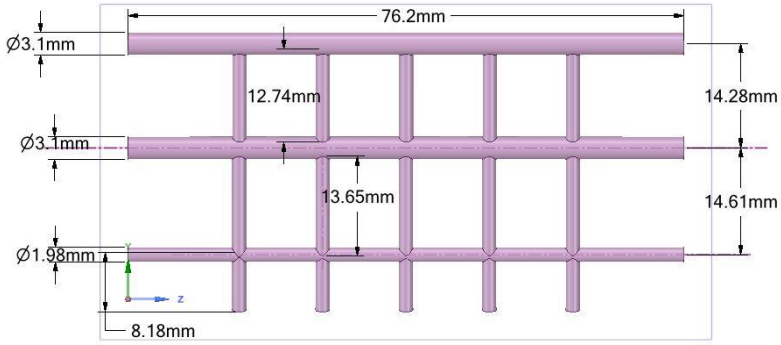

Fig. 3.11 Jet impingement cooling channels configuration

For the computational model in this study, the mesh was designed using ANSYS ICEM. The control volume was set at (16.045 mm, 38.256 mm, and 76.2 mm) with a total volume of 1871.9 mm^2, containing 243,212 nodes and 664,928 elements. A single domain was chosen for the analysis, and the element size was set at 4.338 mm to enhance flow condition accuracy. Fig. 3.12 presents the jet impingement type mesh configuration.

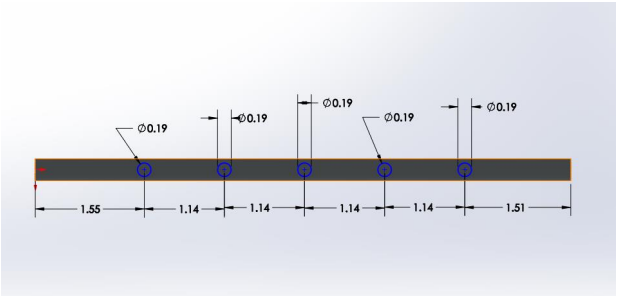

Fig. 3.12 Jet impingement cooling channels configuration joints

Due to the dynamics of smaller scales of the channel and fluid momentum transport within them, the regions close to the wall are particularly active where the solution variable gradients are high. The mesh in these areas was divided into three distinct zones, each identified by its respective Y+ value, a non-dimensional distance parameter related to the local Reynolds number. In this study, the Y+ values were categorized as follows: less than 5 for the viscous sublayer, between 5 and 30 for the buffer or transition zone, and 30 to 60 for the fully turbulent flow zone. For this analysis, a Y+ value of 1 was selected, corresponding to the viscous sublayer near the wall. The fluid medium was chosen as air as ideal gas, having a density of 1.229 kg/m^3 and a viscosity of 0.0000173 kg /m·s. Based on these parameters, the normal wall distance 'Y' was computed using equation. (3.1). Fig.3.13 presents Jet impingement type mesh configuration.

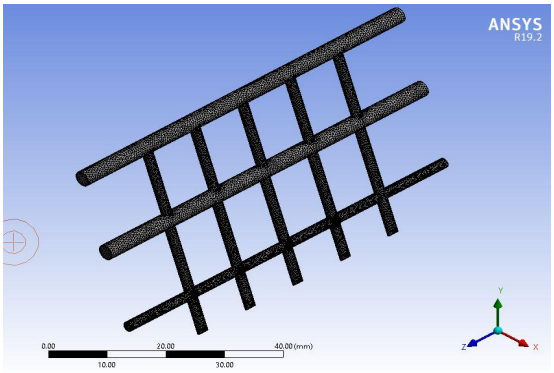

Fig. 3.13 Jet impingement type mesh configuration

The aspect ratio of the mesh elements is an essential component for ensuring the reliability and accuracy of CFD simulations. Its significance cannot be overstated, particularly in specialized applications like turbine cooling channels, where precision is crucial. Fig. 3.14 presents an examination of the mesh aspect ratio, thereby highlighting its critical role in contributing to the integrity and accuracy of computational research. In Fig. 3.14, the aspect ratio chart of the grid schemes reveals the good quality of the mesh.

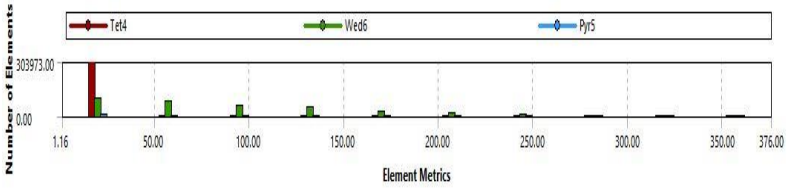

Fig. 3.14 Jet impingement type mesh element aspect ratio

3.6. Numerical Method

The dynamics of fluid flow and heat transfer adhere to specific physical principles, and the mathematical representation of these fluid dynamics is derived by means of fundamental fluid flow governing equations. These complicated equations are typically resolved using numerical methods to investigate the underlying dynamics within fluid flow and heat transfer phenomena. This exploration yields valuable theoretical insights that can guide practical engineering applications. These governing equations 3.5 to 3.8 are the mass equation, momentum equation, and energy equation, with the addition of the fluid state equation to ensure a comprehensive solution [96].

$$\frac{\partial \rho u_i}{\partial x_i} = 0 \tag{3.5}$$

$$\frac{\partial \rho u_i u_j}{\partial x_i} = \rho g_i + F_i - \frac{\partial P}{\partial x_i} + \frac{\partial}{\partial x_i} \cdot \left(2\mu S_{ij}\right) \tag{3.6}$$

$$\frac{\partial \rho u_i E_0}{\partial x_i} = \rho u_i F_i - \frac{\partial q_i}{\partial x_i} + \frac{\partial}{\partial x_j} \cdot \left(u_j T_{ij}\right) \tag{3.7}$$

$$\rho = f(\rho, T) \tag{3.8}$$

Where, F_i – represents the body force, *N*;

P – stands for pressure, *Pa;*

S_{ij} – denotes the strain rate tensor, s^{-1} ;

E_0 – signifies the total internal energy, *J/kg*;

T_{ij} – corresponds to the surface force, *Pa.*

The equation 3.8 suggests that the density (ρ) of a substance is a function of its own density and temperature (T).

In the current investigation, Reynolds-Averaged Navier-Stokes (RANS) based analysis was implemented using a widely used finite-volume solver for the simulations. In a similar study, a

three-pass channel structure equipped with turning vanes and ribs were explored by Guo et al. in [97]. According to the study, the Shear-Stress Transport (SST) k-ω turbulence model demonstrated a maximum deviation of 6.5% from the experimental data. This was notably lower than the discrepancies found with Realizable k-ω and RNG k-ω models, which showed errors of 19.3% and 22.4% respectively. Therefore, in this doctoral thesis work, the SST k-ω turbulence model was used for better accuracy. In addition, the SST turbulence model is specifically efficient in resolving the near-wall flow which makes it suitable for the impingement type cooling channels where the cooling channels pathways are extremely short and narrow.

For the evaluation of pressure drop, Equation 3.10 was used which was derived from the Darcy-Weisbach equation given in [98]. The formula presumes the flow to be fully developed, in turbulent motion, and incompressible, with negligible variations in elevation or velocity along the conduit's length.

$$\Delta P = f \frac{L}{D} \frac{\rho U^2}{2g} \tag{3.10}$$

Where, ΔP – the pressure drop, *pa*;

f – is friction factor;

L – is length of the channel or pipe, *mm*;

D – is the diameter of the channel, *mm*;

ρ – is the density, kg/m^3;

U – is the mean velocity of the fluid, *m/s*;

g – represents gravitational acceleration, m/s^2.

3.7. Parameter Definition

In the experimental setup by Wang [48], the central vane of the NACA C3X turbine blade received cooling via air circulation from the hub towards the root through a series of ten cylindrical channels. The blade material was constructed from ASTM 310 stainless steel. Wang's model replicated these conditions, defining the material properties of ASTM 310 stainless steel to include a specific heat capacity (Cp) of 502 *J/(kg·K)* and a density (ρ) of 8030 kg/m^3 [47], [48].

Based on Wang's [48] study, in this doctoral work, the Reynolds Number (R_e), and the hydraulic diameter (D_C) for each cooling channel was derived from key parameters including fluid mass flow rate ($\dot{m}$), viscosity (μ), and coolant density (ρ). These calculations were carried out to

ensure outlet pressure compatibility with NASA's C3X data, by matching the inlet Reynolds Number from 10000 to 50000. Reynolds Number serves as a pivotal criterion for understanding flow behavior in each cooling channel. Turbulent flows, generally marked by higher Reynolds Numbers, tend to favor elevated heat transfer rates but also lead to transitional flow regimes. These transitional phases present computational challenges, making it difficult to precisely model both flow behavior and heat transfer characteristics within the cooling system.

For the hydraulic diameter-based Reynolds Number (R_e), Equation (3.11) was employed to characterize each cooling passage, using (D_C) as the main parameter for calculation. This approach aids in capturing the details of flow dynamics, which is also crucial for accurate simulation and thermal performance evaluation.

$$R_e = \frac{\frac{\dot{m}}{A} D_c}{\mu} \tag{3.11}$$

Where, ṁ – mass flow rate, *kg/s* ;

μ – fluid viscosity, *kg/m·s*;

D_c – is the cooling channel's hydraulic diameter, *m*;

A – is the area, m^2

Similarly, the Nusselt number was obtained by eq 3.12:

$$N_u = \frac{q D_C}{(T_w - T_f)\lambda} \tag{3.12}$$

Where, *Tw* – presents the wall temperature, K;

T_f – is the average inlet temperature, K; based on mass flow.

λ – denotes the thermal conductivity of the fluid, *W/m·K*;

q – represents the heat flux, W/m^2.

The Nusselt Number (N_{u0}) was used to determine the (HTC) of each cooling channel [99].

$$N_{u0} = \left(0.023 p_r^{0.5} R_e^{0,8}\right) \tag{3.13}$$

Where, Cr – is correction coefficient;

P_r – Prandtl number;

R_e – is Reynolds number.

Resistance factor (friction factor) f is represented as follows:

$$f = \frac{\Delta p D_C}{2\rho L u_{in}^2} \tag{3.14}$$

Where, L – is the length, *m;*

Δp – is the pressure drop, Pa.

ρ – fluid density, kg/m^3

u_{in} – *fluid velocity ,m/s*

The reference resistance factor f_0 was taken from the experimental value given in [48] :

$$f_0 = 0.507 R_e^{-0.3} \tag{3.15}$$

Thermal Performance (TP) provides a comprehensive assessment of the cooling channel characteristics and can be computed as follows:

$$\text{TP} = \left(\frac{N_{ua}}{N_{u0}}\right) \times \left(\frac{f}{f_0}\right)^{-1/3} \tag{3.16}$$

where N_{ua} – presents the average Nusselt number of all heating surface including PS, SS, and tip wall surface.

Drag force was calculated by Eq (3.17)

$$F_d = f \times \frac{\text{L} \times \rho \times U^2}{D_C} \times A \tag{3.17}$$

Where L – is the length, *mm*;

ρ – fluid density, kg/m^3;

U – fluid velocity, *m/s*;

D_c – hydraulic diameter, *mm*;

f – friction factor.

3.8. Boundary Condition

The boundary conditions for the analysis were taken from the experimental test conditions performed by Hylton [51], with a code number 1143 with a heat flux to the wall of 1135 Watt/M^2/K. The constant mass flow rate for the inlet is calculated by Reynolds Number and the inlet channel temperature of the cooling fluid is 298.15K. Tables 4 present the boundary conditions used for the analysis. The outlet pressure used for this study is 1 atm. For simplicity, air as ideal gas was used as the cooling fluid in the channels.

Table 4.

Initial flow condition for the domain.

P_0	q	M_i	l	T_u	T_w/T_g	M_e (x=0.09836)
321KPa	1135 Watt/M^2/K	0.17	0.016m	6.5%	0.73	0.9

3.9. Results

3.9.1. Cooling Performance:

The main idea of the research was to design effective cooling channels for the turbine blade using Computational Fluid Dynamics (CFD) simulations. The simulations were incorporated by special codes developed in MATLAB. The comparative analysis is structured into three distinct segments with specialized cooling configurations and their respective characteristics. Data generated from the study, such as temperature and pressure contour plots, are critically evaluated. This multi-faceted comparison aims to unearth the optimal cooling arrangement by examining key metrics, including Nusselt numbers, friction factors, thermal performance, and drag force, particularly in critical zones within the cooling channels. This analytical approach aims to not only identify the most efficient cooling configuration but also offer insights into potential ways for performance enhancement.

3.9.2. Performance Analysis for U Bend Cooling Channel

Fig.3.15 illustrates the results of the Computational Fluid Dynamics (CFD) simulations, providing insights into the temperature distribution within U bend channels. Notably, the simulations reveal that the maximum temperature reaches approximately 529 K within these channels during fluid flow.

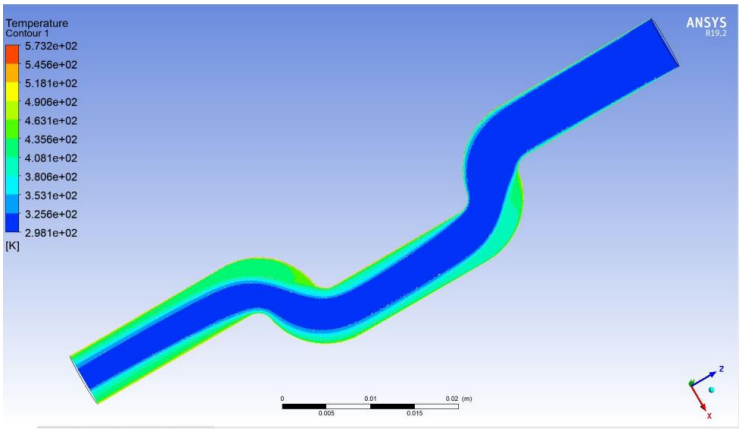

Fig. 3.15 U bend temperature contours

Fig. 3.16 presents velocity contour plots, which depict an intriguing phenomenon: a noticeable increase in velocity around the corners of the bend, with the maximum velocity recorded at an impressive 156 meters per second (m/s).

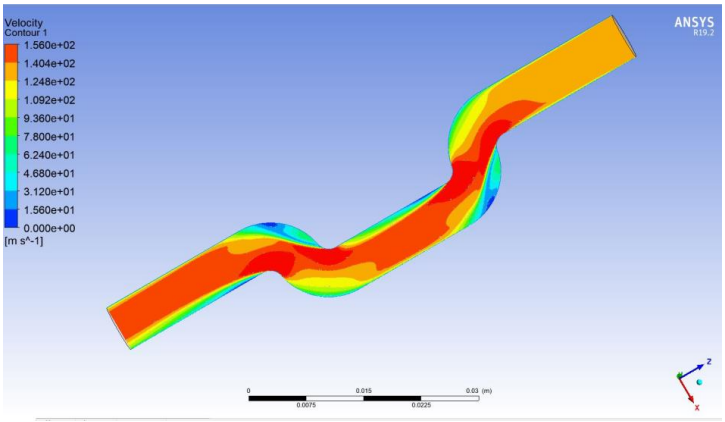

Fig. 3.16 U bend velocity Counters

Fig.3.17 presents the introduced pressure contour plots that offer valuable insights into the system's dynamics. These contours reveal an interesting observation: pressure levels began to elevate notably at the corners of the bend, which were designed with an angle of 129 degrees. The maximum pressure recorded within the system reaches 15.130 KPa. Furthermore, as the channels

progress towards their end. A substantial pressure drop was observed with the pressure eventually decreasing to 3.076 KPa. This information highlights the impact of channel design on pressure distribution throughout the system.

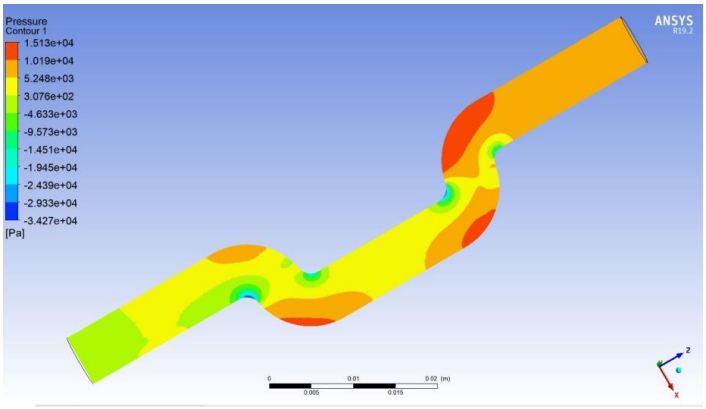

Fig. 3.17 U bend Pressure Counters

Fig. 3.18 illustrates the relationship between the friction factor and Reynolds number, particularly at the bends within the cooling channels. Four most critical locations within the U bend cooling channel were selected i.e., location A, B, C, and D. These are the locations where the flow experiences resistance due to the geometric configuration of bends, therefore, these locations are important where the drag force may have the greatest impact due to pressure drop. As seen in Fig.3.18, the friction factor peaks at 0.92 in location A when the Reynolds number is 10,000. As the Reynolds number escalates to 50,000, there is a significant decrease in the friction factor. This suggests a significant influence of Reynolds number on the friction factor, especially at critical points such as channel turns.

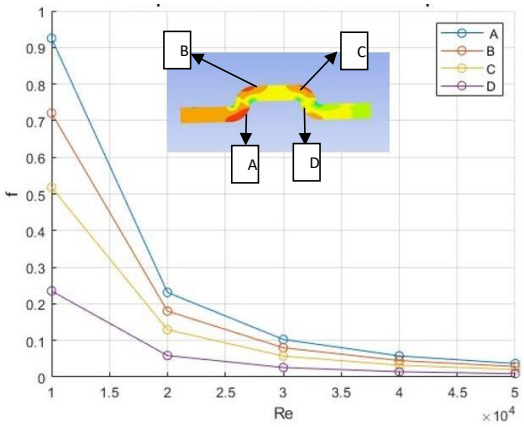

Fig. 3.18 Graph between friction factor (*f*), and (*Re*) Reynolds Number for U channel

Based on the above-mentioned analysis and results, the relationship between the drag force and Reynolds number was studied. A special MATLAB code was developed using the fluid flow equations in order to formulate the precise impact of R_e on the drag force within the cooling channels. As the cooling channels are located in the internal structure of the turbine blade and they possess extremely narrow pathways, therefore, the evaluation of drag force (which mainly appears as pressure drop) within the cooling channels is of paramount importance. MATLAB code developed for this drag force evaluation is given in Appendix 2 of this doctoral thesis. The results for Re and drag force evaluated from the developed MATLAB code are presented in Table. 5. As seen from the calculated values, the maximum drag force is at location A which is the first bend in the cooling channel. On the positive side, the flow pressure is sufficient to travel across the channel with carried momentum energy to perform the cooling process, as observed in velocity contours of Fig. 3.16. Intriguingly, this level of drag force maintains its constancy across a Reynolds Number range spanning from 10,000 to 50,000. From the simulated results of CFD analysis and the MATLAB code, it can be concluded that the U Bend channel design offers good cooling, but the drag force is slightly higher.

Table 5

U bend Drag forces at locations A, B, C, and D.

Location	Drag force
A	0.25 N
B	0.19 N
C	0.14 N
D	0.061 N

3.10. Performance Analysis for Net Bend Cooling Channels

Fig. 3.19 presents the results of the Computational Fluid Dynamics (CFD) analysis aimed at understanding thermal behavior within the network of Net Bend cooling channels. The temperature contours explicitly highlight the highest temperature zones associated with peak thermal values within the channels. The temperature reaches nearly 541K for the fluid flowing through the cooling channel. This peak temperature point may have significant implications for the material properties and operational conditions, emphasizing the importance of thermal management strategies within these networked systems.

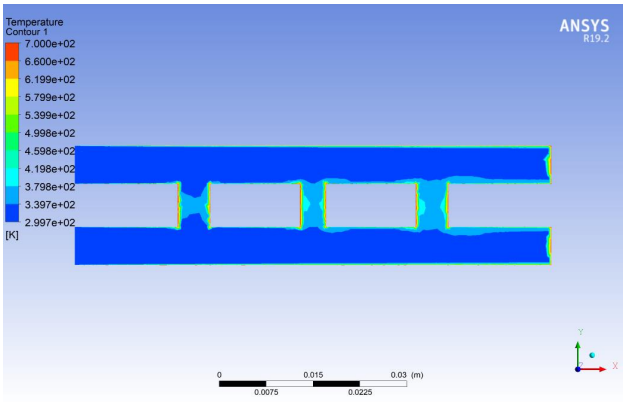

Fig. 3.19 .Net cooling channel temperature contours.

Fig. 3.20 showcases contour plots of fluid velocity, offering a detailed visual analysis of the fluid dynamics within the designed channel network system bends. The data indicates a surge in fluid velocity specifically around the corner regions, reaching an extraordinary 179 m/s. These observations not only highlight the intricacies of fluid flow within constrained geometries but also underline the need for meticulous design considerations, especially when dealing with high-velocity flow conditions.

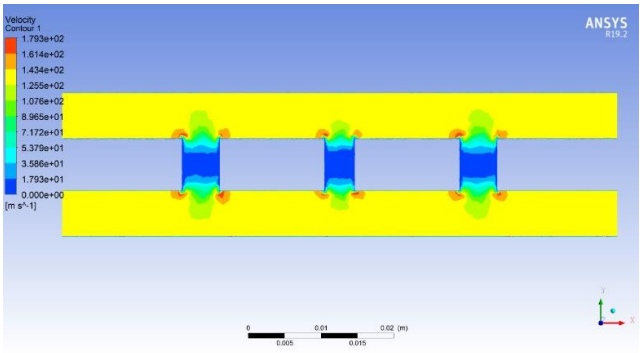

Fig. 3.20. Net cooling channel velocity contours.

Fig. 3.21 presents the pressure contour plots which offer valuable insights into the system's dynamics. These contours reveal an interesting observation: pressure levels begin to elevate notably within the Net channels, which have been designed with an angle of 90 degrees. The maximum pressure recorded within the system reaches 6.874 KPa. Furthermore, as the channels progress towards their termination, a substantial pressure drop can be observed with a value reaching to 1.736 KPa. This information highlights the impact of channel design on pressure distribution throughout the system.

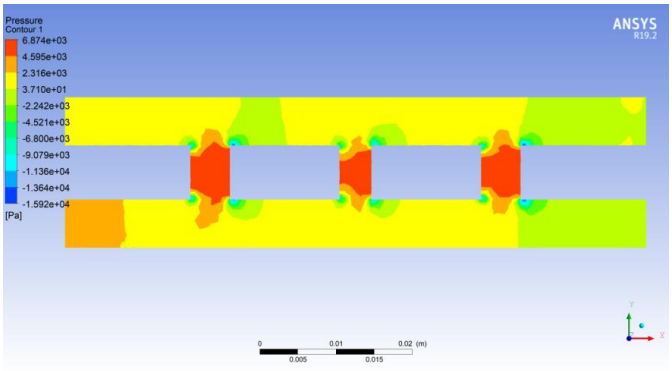

Fig. 3.21 .Net cooling channel pressure contours.

Fig. 3.22 demonstrates the relationship between the friction factor and Reynolds number, with a focus on the bends in the cooling channels. Three critical locations within the net cooling channel were specifically chosen for analysis: locations A, B, and C, these points are of particular interest due to the resistance encountered by the flow, resulting from the variations in the geometric configuration. Consequently, these locations are pivotal in understanding the impact of drag force, especially in relation to the pressure drop. As depicted in Figure 3.18, a notable peak in the friction factor, reaching 1.2 at location C, is observed at location when the Reynolds number is 10,000 throughout the channel. However, as the Reynolds number increases to 50,000, there is a marked decrease in the friction factor at all selected locations. This indicates a substantial effect of the Reynolds number on the friction factor, particularly at critical junctures like the turns in the channel. The cooling effect will be highly dependent on the speed variations and a minimum pressure to maintain the flow within the channel is inevitable, as seen in pressure variation contours in Fig. 3.21.

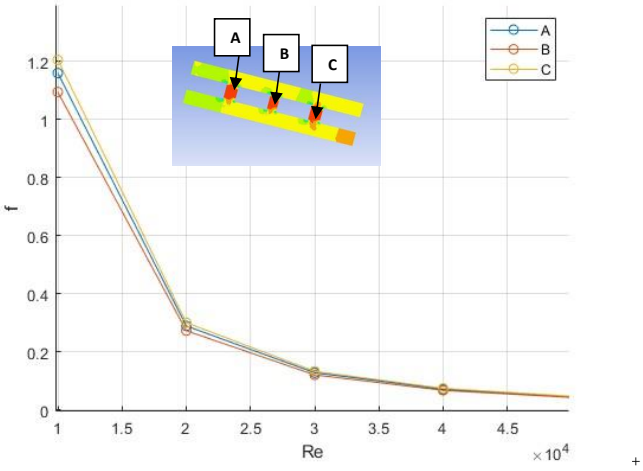

Fig. 3.22 The variation of fraction factor with Reynolds Number for net cooling channels.

Based on the analysis and results previously mentioned, the relationship between drag force and Reynolds number was closely examined. A specialized MATLAB code was developed, utilizing fluid dynamic equations, to accurately determine the impact of the Reynolds number (R_e) on the drag force within the cooling channels. Considering that these channels are situated within the internal structure of turbine blades and feature extremely narrow passageways, assessing the drag force primarily manifesting as a pressure drop is crucial. The MATLAB code created for this evaluation is included in Appendix 2 of this doctoral thesis. The results correlating Reynolds number with drag force, as derived from the MATLAB code, are presented in Table 6. The calculated values reveal that the maximum drag force occurs at location A, which is the initial bend in the cooling channel. On a positive note, the flow pressure is adequate to flow through the channel, carrying sufficient momentum energy to facilitate the cooling process. This is evident in the velocity contours shown in Fig. 3.20. Interestingly, this level of drag force remains consistent across a range of Reynolds numbers, from 10,000 to 50,000. From the combined insights of Computational Fluid Dynamics (CFD) analysis and MATLAB code, performed in this doctoral thesis, it is unfortunately observed that the Net type cooling channel is not as efficient as the classic U Bend channel, as the amount of heat transfer carried by the flow in Net channel is lower than the U Bend channels.

From this point, on one hand, U Bend channel is better than the Net type channel, however,

the amount of heat energy transported to turbine blade from the combustion chamber is too high to be sufficiently handled by only the U-shaped sections of the U Bend channel due to lower surface area availability. Therefore, a new (out of the box) solution in terms of the increased surface area channels is essential. This doctoral thesis offers a relatively complex but effective cooling channel design i.e., Impingement type cooling channel. The results of this impingement type cooling channel are given in the next section.

Table 6

Net cooling channels drag forces at locations A, B, and C.

Location	Drag force
A	0.0271 N
B	0.026 N
C	0.023 N

3.11. Performance Analysis for Jet Impingement Type Cooling Channels

Jet impingement type cooling channel, which is a special network of cooling channels, was designed in a web-shape manner at the trailing edge of the blade. This network of channels is close to the jet impingement channel in terms of design proposed by [95]. Fig. 3.23 presents a trend of velocity flow in terms of velocity vectors within the jet impingement type cooling channels. The velocity reaches an elevated level of approximately 116 m/s in the main impingement sections and distributes to subsections of the cooling channel. This high-velocity zone could be a critical factor in understanding the unanticipated HTC results.

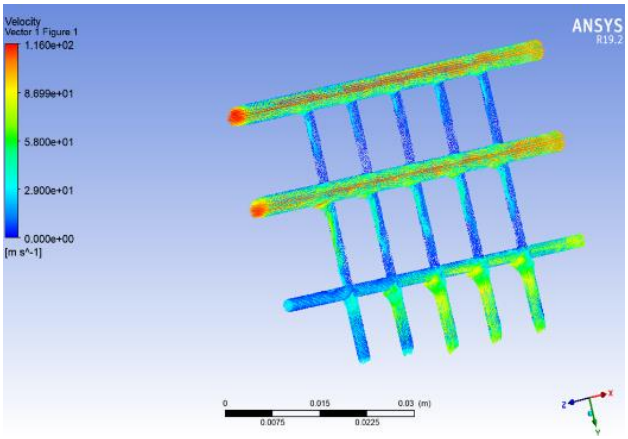

Fig. 3.23 Jet impingement type cooling channel velocity vectors.

Fig. 3.24. presents the temperature contours within the jet impingement type cooling channel. The temperature within the channels varies from 465.3 K to 658.3 K, demonstrating the heat (temperature) distribution within the blade.

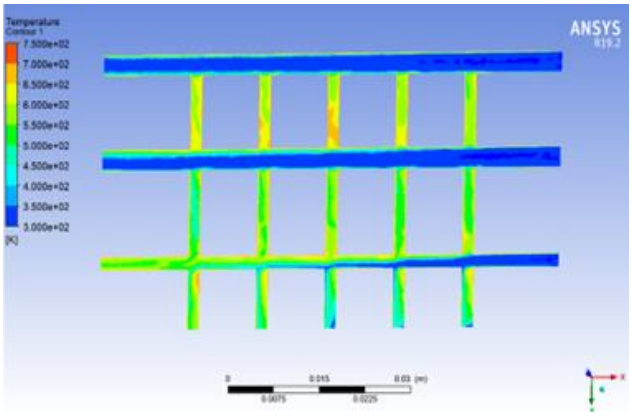

Fig. 3.24. Jet impingement type cooling channel temperature contours.

Fig. 3.25 explains the pressure contour plots. Pressure drops along the channel. At this point, the pressure escalates, peaking at 4.281 KPa. As the channels extend towards their endpoints, a marked pressure build up is observed due to the decelerated flow at the end section, plummeting to a value of 1,320 KPa. This data underscores the significant role that channel geometry plays in modulating pressure distribution across the channel.

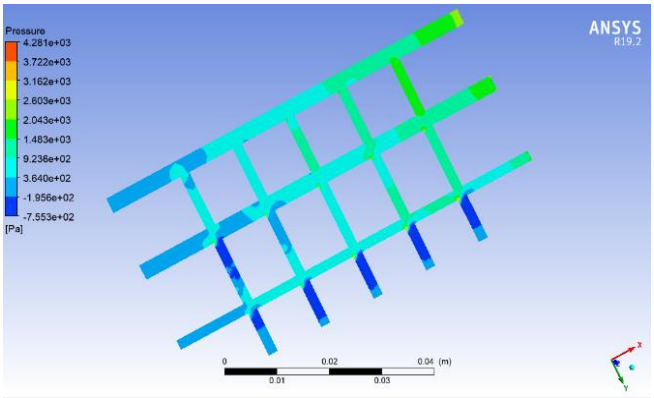

Fig. 3.25. Jet impingement type cooling channel pressure contours.

Fig. 3.26 illustrates the most important flow relationship between the friction factor and Reynolds number. As the jet impingement type is very complicated in configuration, therefore, for simplicity, 15 locations were chosen, each demonstrating a joint location in the channel. The friction factor was calculated at each location with respect to the Reynolds Number. The data indicates an apex in fraction factor, reaching a value of 0.027 at the designated point 7, corresponding to a Reynolds Number of 10,000. Conversely, an escalation of the Reynolds Number to 50,000 manifests a notable decrement in the friction factor, plummeting to a value of 0.0056. Such variations manifest the sensitivity of the friction factor to fluctuations in Reynolds Numbers, particularly at geometrically complex regions i.e., bends in the cooling channels. These Reynolds Number-based variations provide the foundation for the further investigations into thermal management strategies for cooling channel heat transfer, discussed in the next chapter of this doctoral thesis.

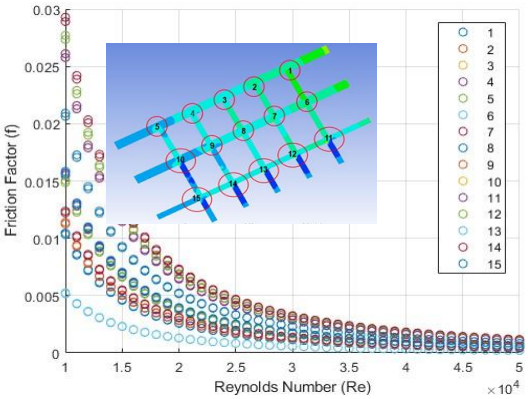

Fig. 3.26. Variation of friction factor with Reynolds Number for jet impingements type cooling channels.

Based on the analysis and findings, the relationship between drag force and the Reynolds number was evaluated. A MATLAB code was created also for the impingement type channel as well, incorporating fluid dynamics equations, to precisely quantify the influence of the Reynolds Number (R_e) on the drag force within the cooling channels. Given that these channels are integrated into the turbine blade's internal structure and feature notably narrow passageways, assessing the drag force predominantly manifested as a pressure drop is critical. The MATLAB code devised for this assessment is detailed in Appendix 2 of this doctoral thesis. The outcomes pertaining to R_e and drag force, ascertained through the MATLAB code, are presented in Fig. 3.27. According to the derived data, the highest drag force is located at position 7, Fortunately, the flow pressure is sufficient to navigate the channel, maintaining enough momentum energy to execute the cooling function, as illustrated in the velocity victors of Fig. 3.23. Remarkably, this drag force level decreases across Reynolds numbers ranging from 10,000 to 50,000. Based on the results from Computational Fluid Dynamics (CFD) simulations and MATLAB code analyses, it is evident that the Jet impingement type cooling channel design ensures effective cooling, with decreasing drag force as Reynolds number increases.

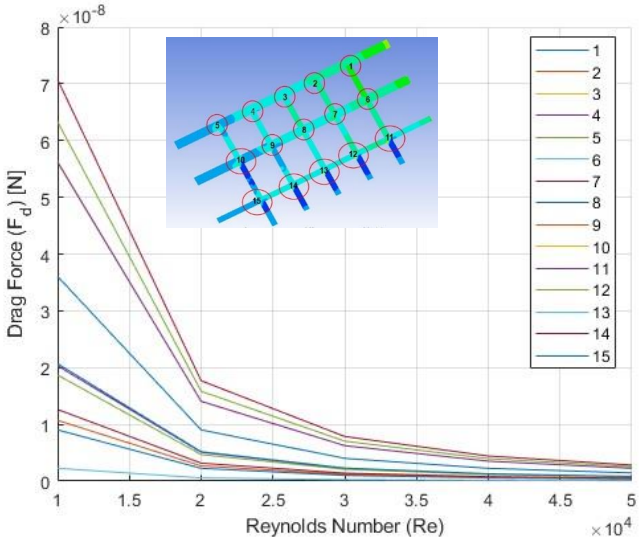

Fig. 3.27. Variation of drag force with Renolds number.

3.12. Result Comparison of Cooling Channels Flow Characteristics

The comparison of the results obtained from the three designed cooling channels (U bend, Net type, and Jet impingement type) is presented in this section. Nusselt number ratio is a very important and useful parameter for the flow heat transfer. The importance of the Nusselt number ratio in this context lies in its ability to quantify the efficiency of heat transfer processes. A higher N_{ua}/N_{u0} ratio indicates a more effective convective heat transfer compared to conductive heat transfer. In practical applications, such as in cooling channels, this efficiency is crucial for maintaining optimal operating temperatures and ensuring the longevity and reliability of equipment. The observed variations in the Nusselt number ratio across different cases highlight the impact of design choices and operational parameters on heat transfer efficiency. The data reveals an initial decline in the Nusselt number ratio (Nu_a/N_{u0}) for all cases, followed by an increase in the Reynolds number (Re). Notably, the Jet Impingement Cooling Channel (Case 3) and the U-Bend Cooling Channel Type (Case 1) demonstrate more significant improvements compared to the Net Cooling Channel (Case 2). The guide vane's thickness emerges as a critical factor influencing thermal exchange at the tip-wall. As illustrated in Fig.3.28, at a Reynolds number of 60,000, the Jet Impingement Cooling Channel Type (Case 3) exhibits a significant increase of 25.3% in the

Nusselt number ratio (Nu_a/N_{ua}). This enhancement is primarily due to the increased fluid acceleration in the outer region of the Jet channels. Specifically, the significant increase in the Na/N0 ratio for the jet impingement cooling channel underlines the effectiveness of this design in enhancing heat transfer, especially at higher Reynolds Numbers.

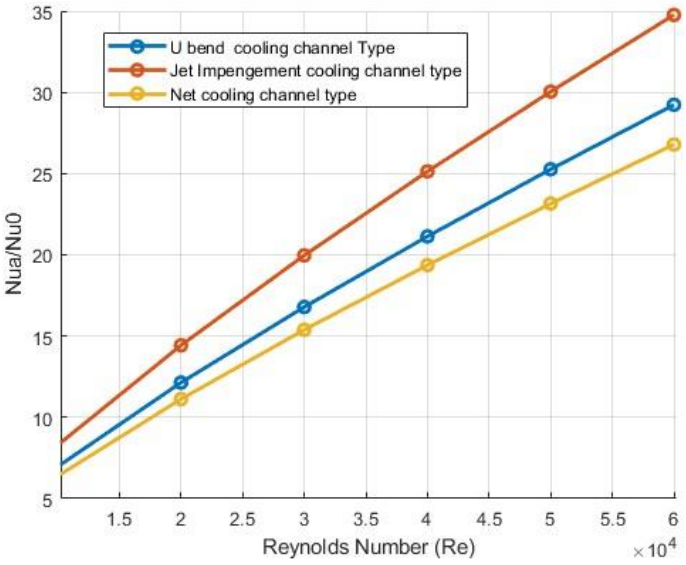

Fig. 3.28. Comparison of N_{ua}/N_{uo} vs. Renolds Number for cooling channels.

The assessment of a channel's overall performance heavily relies on its frictional characteristics. Fig. 3.29 illustrates the variations of f/f_o with Reynolds number (R_e) for all considered cases. The data from the graph highlights, when Reynolds Number (R_e) reaches 20,000, Net cooling channels (Case 2) stand out with a remarkable 25.7% reduction in drag. However, it's essential to note that excessively thick turning vanes can increase channel friction accordingly. This phenomenon occurs because as the thickness of the guide vanes increases, the flow area at the channel's corners decreases, leading to increased resistance due to the reduced cross-sectional area of the basin. While at R_e equal 30,000, Jet impingement type cooling channel (case 3) has reduction in drag with 10.56 % compared to the Net cooling channels (case 2), and up to 20 % reduction than U bend cooling channels (case 1).

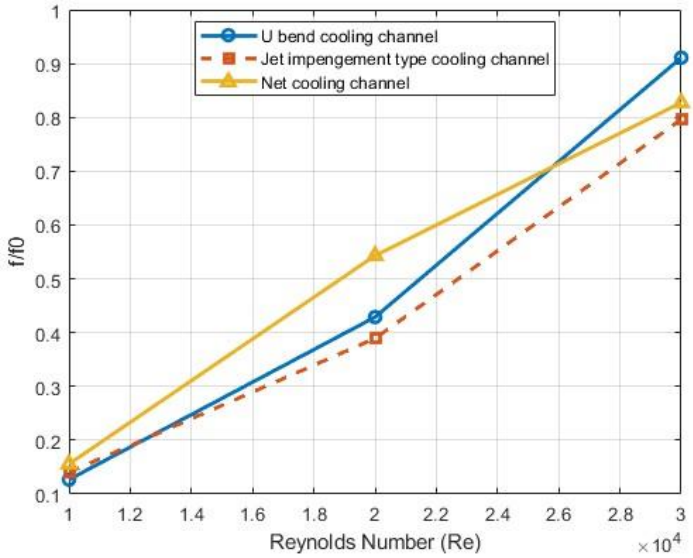

Fig. 3.29. The variation f/f_o with Renolds Number for different cooling channels.

The enhancement in the channel's thermal transfer efficiency often comes at the cost of diminished frictional performance. The Thermal Performance (TP) metric offers a more holistic view by simultaneously accounting for both heat exchange and friction characteristics, thereby providing a well-rounded assessment of the channel's overall performance. Figure 3.30 illustrates how Thermal Performance (TP) varies with Reynolds Number (R_e) across different channels. Initially, as Re escalates, the TP for each channel experiences a decline, reaching its lowest point around R_e=25,000. This phenomenon is largely attributed to minimal advancement in heat exchange levels and a noticeable uptick in channel friction at lower R_e values. Subsequently, as R_e continues to rise, heat transfer efficiency notably improves, leading to a corresponding increase in TP. Within the lower Re range (10,000 to 30,000), when the Reynolds Number (R_e) is at 10,000, the TP in Net cooling channel (case 2) sees an improvement of 3.5%. However, an overly thick internal channels net can result in significant friction losses. In the Re range of 20,000 to 30,000, Net cooling channel (case2) doesn't perform as well in terms of TP as (case1) does. Jet impingement type (Case 3) showed better thermal performance at Re 20,000 with 11.27 % than U bend cooling channel (Case 1). This leads to a gradual outperformance of jet impingement (case 3) in TP compared to other channel configurations. Based on these observations, it can be projected that Jet

impingement type cooling channels (case 3) will offer the most balanced thermal performance when R_e exceed. Fig. 3.30 presents the variation TP with Renolds number for different cooling channels.

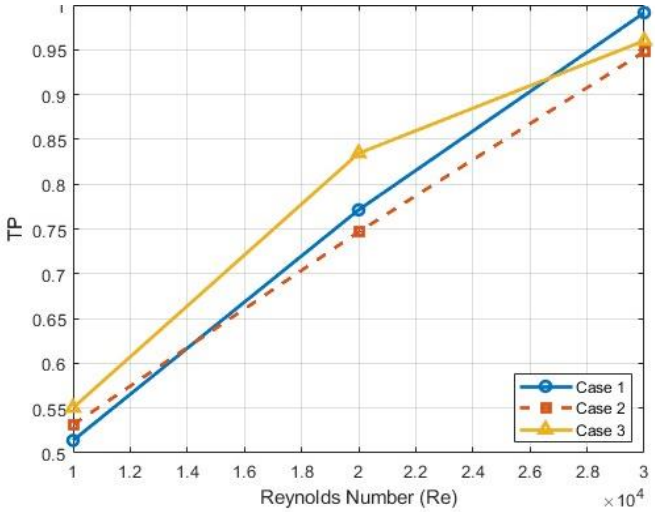

Fig. 3.30. The variation TP with Renolds Number cooling channels.

3.13. Discussion

The overall comparative analysis (in the next Section) shows that the specially designed impingement type cooling channels are (so far) the best performing cooling channels compared in this study. Jet impingement type channels demonstrate enhanced heat transfer capabilities. Full scale analysis for the heat transfer was additionally performed and is presented in Chapter 4 of this doctoral thesis.

Given the observed variations and complexities in performance, the current study strongly suggests the need for more advanced predictive cooling channels. Utilizing machine learning algorithms or more refined CFD models could yield more accurate predictions and provide better design insights. The study serves as a strong foundation but leaves room for additional investigations, particularly in fine-tuning design parameters for specific applications. The goal should be not just to understand but also to control these various factors to achieve an optimized cooling channel system.

3.14. Summary Of Chapter 3.

This investigation thoroughly examines the cooling attributes of various channel configurations. The study examined the thermal and hydraulic characteristics of various cooling channel configurations at different Reynolds numbers (R_e). Key findings indicate that slimmer turning vanes are more effective in reducing drag and improving thermal performance. The results have significant implications for optimizing cooling efficiency in different operational conditions.

As a result, the following findings were discovered:

1. The data reveals an initial decline in the Nusselt number ratio (N_{ua}/N_{uo}) for all cases, followed by an increase in the Reynolds Number (R_e). Notably, the Jet impingement cooling channel (Case 3) and the U-Bend Cooling Channel Type (Case 1) demonstrate more significant improvements compared to the Net Cooling Channel (Case 2). The guide vane's thickness emerges as a critical factor influencing thermal exchange at the tip-wall. As illustrated in Fig 3.28, at a Reynolds number of 60,000, the Jet Impingement cooling channel type (Case 3) exhibits a significant increase of 25.3% in the Nusselt number ratio (N_{ua}/N_{uo}). This enhancement is primarily due to the increased fluid acceleration in the outer region of the Jet channels. Specifically, the significant increase in the (N_{ua}/N_{uo}) ratio for the Jet Impingement cooling channel underlines the effectiveness of this design in enhancing heat transfer, especially at higher Reynolds numbers.
2. The data from the graph highlights, when Reynolds Number (R_e) reaches 20,000, Net cooling channels (Case 2) stand out with a remarkable 25.7% reduction in drag. However, it's essential to note that excessively thick turning vanes can increase channel friction accordingly. This phenomenon occurs because as the thickness of the guide vanes increases, the flow area at the channel's corners decreases, leading to increased resistance due to the reduced cross-sectional area of the basin. While at R_e equal 30,000, Jet impingement type cooling channel (case 3) has reduction in drag with 10.56 % compared to the Net cooling channels (case 2), and up to 20 % reduction than U bend cooling channels (case 1).
3. The Thermal Performance (TP) metric offers a more holistic view by simultaneously accounting for both heat exchange and friction characteristics, thereby providing a well-rounded assessment of the channel's overall performance. Fig 3.30 illustrates how Thermal Performance (TP) varies with Reynolds Number (R_e) across different channels.

Initially, as R_e increases, the TP for each channel experiences a decline, reaching its lowest point around R_e=25,000. This phenomenon is largely attributed to minimal advancement in heat exchange levels and a noticeable uptick in channel friction at lower Re values. Subsequently, as Re continues to rise, heat transfer efficiency notably improves, leading to a corresponding increase in TP. Within the lower R_e range (10,000 to 30,000), when the Reynolds Number (R_e) is at 10,000, the TP in Net cooling channel (case 2) sees an improvement of 3.5%. However, an overly thick internal channels net can result in significant friction losses. In the Re range of 20,000 to 30,000, Net cooling channel (case2) doesn't perform as well in terms of TP as (case1) does. Jet impingement type (Case 3) showed better thermal performance at R_e 20,000 with 11.27 % than U bend cooling channel (Case 1). This leads to a gradual outperformance of jet impingement (case 3) in TP compared to other channel configurations. Based on these observations, it can be projected that Jet impingement type cooling channels (case 3) will offer the most balanced thermal performance when R_e exceeds.

4. DESIGN OPTIMIZATION OF TURBINE BLADE COOLING CHANNELS BY APPLYING JET IMPINGEMENT TYPE CHANNELS.

The results from this chapter were published in [100].

4.1. Introduction

The primary objective is to enhance the cooling efficiency of turbine blades through the application of the jet impingement type method. This study involves the analysis of experimental data from the NASA 3CX turbine blade. A 3D model was created using SolidWorks, and computational fluid dynamics (CFD) simulations were conducted to analyze the coolant flow and temperature distribution within the vane. These simulations were complemented by experimental testing to validate the CFD results and gain deeper insights into the cooling system's effectiveness. For the CFD simulations, ANSYS FLUENT code served as the solver, and ANSYS ICEM-CFD was utilized for mesh generation. A MATLAB algorithm was employed to process experimental data, aiding significantly in the simulations. The study also incorporated heat transfer conjugation analysis, focusing on SST shear stress and the k-ω turbulence model.

The findings of this research reveal that the cooling channels within the blades experience a considerable reduction in hydraulic diameter, ranging from 49 % to 69%, as they extend towards the blade's trailing edge. This reduction markedly influences the heat transfer coefficients and the overall efficiency of the cooling system. The study observed that the pressure side of the turbine blade aligns with the Hylton Model [51]. However, it also noted a higher-than-expected heat transfer coefficient around the blade head and most of the suction side, with a variance of 23 % in the average heat transfer coefficient compared to previous models. A key discovery was the enhanced cooling effectiveness of the optimized jet impingement type model, which stood at 0.4892 for the entire blade, and 0.6936 when compared with its base model counterpart. The optimized model exhibited a substantial increase in cooling effectiveness, up by 29 % for the entire blade and 28 % for the trailing edge. These improvements underscore the critical role of optimized cooling designs in maintaining the efficiency and safety of turbine blade operations.

4.2. Methodology

Computational Fluid Dynamics (CFD) stands out as a pivotal tool in developing these configurations. CFD simulations offer intricate insights into flow dynamics and heat transfer within turbine blades, aiding in the enhancement of cooling designs for better thermal performance. The following methods were employed in this research:

- Utilizing NASA's C3X Hylton Model [51], [70] data, this research involved gathering experimental data on turbine blade cooling configurations for establishing foundation for the Computational fluid dynamics simulation.
- Establishing the base model geometry and dimensions for domain simulation encompassing the turbine blade and its surrounding fluid environment.
- Implementing the conjugate heat transfer (CHT) model to simulate heat exchange between the gas turbine blade and the adjacent fluid.
- Choosing the SST k- ω turbulence model to accurately represent turbulence within the fluid domain.
- A comprehensive three-dimensional CAD model of the gas turbine blade, along with its cooling system, was meticulously developed using SolidWorks. This process involved detailed modeling of the blade's design and its associated cooling features.
- Developing a custom MATLAB code, along with a MATLAB algorithm, to execute necessary calculations for the CFD simulation and compare with the reference experiment data.
- Generating a high-quality mesh through ANSYS ICEM-CFD, faithfully replicating the geometry of both the turbine blade and the associated fluid domain.
- Performing the Computational Fluid Dynamics (CFD) simulation entails Utilizing ANSYS FLUENT as the computational solver for the analysis, seamlessly incorporating the selected heat transfer and turbulence models. To ensure accuracy and facilitate meticulous numerical analysis, a custom MATLAB code is seamlessly integrated into the simulation process.

4.3. Initial Base Model Configuration

The NASA C3X Airfoil coordinates are visually represented in Table 7, where a cascade coordinate system is employed to define the precise shape of the airfoil. Cooling for the vane is achieved through a network of ten radial cooling channels.

Table 7

NASA C3X Airfoil coordinates [51]

Position number	x -- cm	(in.)	Y - cm_	(in.)	Position number	x -- cm	(in.)	y = -cm	in.)
1	0.1097	0.0432	11.6546	4.5885	40	7.4849	2.9468	-0.0617	-0.0243
2	0.3894	0.1533	12.189	4.7988	41	7.3188	2.8814	0.3559	0.1401
3	0.7658	0.3015	12.6764	4.9907	42	7.1483	2.8143	0.7737	0.3046
4	1.2723	0.5009	13.0233	5.1273	43	6.9736	2.7455	1.1895	0.4683
5	1.8743	0.7379	13.1376	5.1723	44	6.795	2.6752	1.6035	0.6313
6	2.4707	0.9727	12.9939	5.1157	45	6.6116	2.603	2.0155	0.7935
7	2.9835	1.1746	12.6538	4.9818	46	6.4237	2.529	2.4254	0.9549
8	3.3985	1.338	12.1976	4.8022	47	6.2309	2.4531	2.8329	1.1153
9	3.7376	1.4715	11.6817	4.5991	48	6.0328	2.3751	3.238	1.2748
10	4.0272	1.5855	11.1364	4.3844	49	5.8296	2.2951	3.6406	1.4333
11	4.2885	1.6884	10.5766	4.164	50	5.6203	2.2127	4.0401	1.5906
12	4.5326	1.7845	10.0094	3.9407	51	5.4051	2.128	4.4364	1.7466
13	4.7648	1.8759	9.4369	3.7153	52	5.1834	2.0407	4.829	1.9012
14	4.987	1.9634	8.8605	3.4884	53	4.9548	1.9507	5.2177	2.0542
15	5.2019	2.048	8.2814	3.2604	54	4.7191	1.8579	5.602	2.2055
16	5.411	2.1303	7.7003	3.0316	55	4.476	1.7622	5.9817	2.355
17	5.6157	2.2109	7.1176	2.8022	56	4.2248	1.6633	6.3564	2.5025
18	5.8171	2.2902	6.5336	2.5723	57	3.9654	1.5612	6.7249	2.6476
19	6.016	2.3685	5.9487	2.342	58	3.6975	1.4557	7.0874	2.7903
20	6.2126	2.4459	5.3632	2.1115	59	3.4204	1.3466	7.443	2.9303
21	6.4074	2.5226	4.7767	1.8806	60	3.1339	1.2338	7.7909	3.0673
22	6.5997	2.5983	4.1897	1.6495	61	2.8374	1.1171	8.1308	3.2011
23	6.7894	2.673	3.6015	1.4179	62	2.5314	0.9966	8.4615	3.3313
24	6.9756	2.7463	3.0122	1.1859	63	2.2149	0.872	8.7826	3.4577
25	7.1575	2.8179	2.4221	0.9536	64	1.8885	0.7435	9.0935	3.5801
26	7.3335	2.8872	1.8301	0.7205	65	1.5519	-0.611	9.3932	3.6981
27	7.5024	2.9537	1.2357	0.4865	66	1.2052	0.4745	9.6815	3.8116
28	7.6624	3.0167	0.6391	0.2516	67	0.8494	0.3344	9.9578	3.9204
29	7.8115	3.0754	0.4115	0.0162	68	0.4999	0.1968	10.2116	4.0203
30	7.8161	3.0772	-0.0053	-0.0021	69	0.3848	0.1515	10.3035	4.0565
31	7.8082	3.0741	-0.0516	-0.0203	70	0.2822	0.1111	10.4094	4.0982
32	7.7879	3.0661	-0.0935	-0.0368	71	0.1938	0.0763	10.5273	4.1446

33	7.7572	3.054	-0.1288	-0.0507	72	0.1212	0.0477	10.6556	4.1951
34	7.718	3.0386	-0.1542	-0.0607	73	0.065	0.0256	10.792	4.2488
35	7.6736	3.0211	-0.1681	-0.0662	74	0.0264	0.0104	10.9342	4.3048
36	7.6269	3.0027	-0.1699	-0.0669	75	0.0064	0.0025	11.0802	4.3623
37	7.5816	2.9849	-0.1588	-0.0625	76	0.0046	0.0018	11.2278	4.4204
38	7.5408	2.9688	-0.1356	-0.0534	77	0.0216	0.0085	11.3741	4.478
39	7.5077	2.9558	-0.1026	-0.0404	78	0.0569	0.0224	11.5171	4.5343

Additionally, Fig. 4.1 presents the Finite element grip structure for each cooling hole for NASA C3X vane. To outline the feature points of the spline accurately, SolidWorks was harnessed, making use of the individual coordinates extracted from Hylton's experimental data[70].

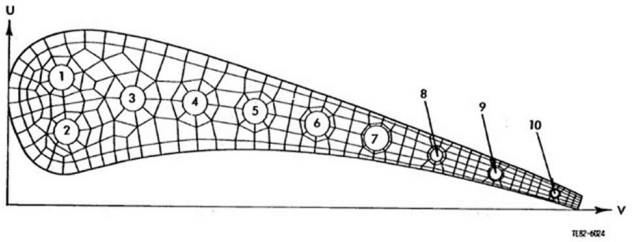

Hole No.	U--cm (in.)	V--cm (in.)	Diameter--cm (in.)	Cr
1	2.377 (0.936)	1.311 (0.516)	0.630 (0.248)	1.118
2	1.057 (0.416)	1.534 (0.604)	0.630 (0.248)	1.118
3	1.981 (0.780)	3.119 (1.228)	0.630 (0.248)	1.118
4	1.981 (0.780)	4.674 (1.840)	0.630 (0.248)	1.118
5	1.869 (0.736)	6.182 (2.434)	0.630 (0.248)	1.118
6	1.666 (0.656)	7.747 (3.050)	0.630 (0.248)	1.118
7	1.412 (0.556)	9.235 (3.636)	0.630 (0.248)	1.118
8	1.087 (0.428)	10.759 (4.236)	0.310 (0.122)	1.056
9	0.737 (0.290)	12.253 (4.824)	0.310 (0.122)	1.056
10	0.345 (0.136)	13.757 (5.416)	0.198 (0.078)	1.025

Fig. 4.1 Finite element grip structure for NASA c3x with cooling channel's locations [51]

In Ansys Fluent, the three-dimensional model was utilized to perform Conjugate Heat Transfer (CHT) analyses on both the initial and improved cooling channel configurations. Fig. 4.2 presents the original three-dimensional layout of the C3X turbine blade. Within the analysis, Hylton introduced a correction coefficient (Cr) into a modified Nusselt Number equation to address the thermal entrance region's influence [51].

Hylton explained that the Cr constant depends on factors such as the Prandtl number (Pr), Reynolds number based on diameter (R_e), and the distance from the leading edge normalized by diameter (X/D) [51]. A range of values for the Cr (correction coefficient), spanning from 1.03 to 1.12, was employed in the calculation of the Nusselt Number (Nu) and the determination of the heat transfer coefficient (HTC) for the ten cooling channels [70]. Subsequently, the Nusselt number

(Nu) and heat transfer coefficient were compared with data from reference experimental data, and the baseline configuration obtained in the present study [6].

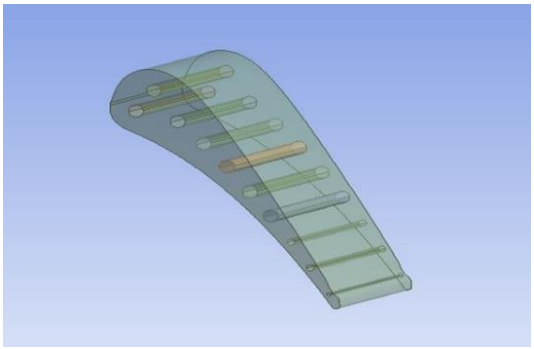

Fig. 4.2. Base model turbine blade cooling.

4.4. Mathematical Model

The governing equations employed in this study encompass the continuity equation (Eq. 4.1), the time-averaged Navier-Stokes (N-S) equations, and the energy equations for the turbulent model. Specifically, the momentum equations utilized in this investigation are represented by Eq. (4.2 to 4.5) [101].

Continuity equation:

$$\frac{\partial \rho}{\partial t} + \frac{\partial (\rho u)}{\partial x} + \frac{\partial (\rho v)}{\partial y} + \frac{\partial (\rho w)}{\partial z} = 0 \tag{4.1}$$

Where, u – represents the velocity components in X direction, *m/s*;

v – represents the velocity components in Y direction, *m/s*;

w – represents the velocity components in Z direction, *m/s*;

ρ – is the fluid density, kg/m^3.

t – time, s.

Momentum Equation:

$$\rho\left(u\frac{\partial u}{\partial x} + v\frac{\partial u}{\partial y} + \omega\frac{\partial u}{\partial z}\right) = -\frac{\partial p}{\partial x} + \mu\left(\frac{\partial^2_u}{\partial x^2} + \frac{\partial^2_u}{\partial y^2} + \frac{\partial^2 u}{\partial z^2}\right) \tag{4.2}$$

$$\rho\left(u\frac{\partial v}{\partial x} + v\frac{\partial v}{\partial y} + \omega\frac{\partial v}{\partial z}\right) = -\frac{\partial p}{\partial y} + \mu\left(\frac{\partial^2_v}{\partial x^2} + \frac{\partial^2_v}{\partial y^2} + \frac{\partial^2 v}{\partial z^2}\right) \tag{4.3}$$

$$\rho\left(u\frac{\partial w}{\partial x} + v\frac{\partial w}{\partial y} + \omega\frac{\partial w}{\partial z}\right) = -\frac{\partial p}{\partial z} + \mu\left(\frac{\partial^2_w}{\partial x^2} + \frac{\partial^2_w}{\partial y^2} + \frac{\partial^2 w}{\partial z^2}\right) \tag{4.4}$$

Where, u – represents the velocity components in X direction, m/s;
v – represents the velocity components in X direction, m/s;
w – represents the velocity components in X direction, m/s;
μ – is Dynamic Viscosity, kg/m·s;
P – is the pressure, Pa;
ρ – is the fluid density, kg/m3.

Energy equation: The energy derivation relation equations have been used [102].

$$\frac{\partial}{\partial x_i}\left(\rho_f u_i\ C_p T - k\frac{\partial T}{\partial x_j}\right) = u_i\frac{\partial p}{\partial x_i}\mu\left(\frac{\partial u_i}{\partial x_j}+\frac{\partial u_j}{\partial x\mathrm{i}}\right) - \frac{2}{3}\ \mu\frac{\partial u_k}{\partial x_k}\delta_{ij} \quad (4.5)$$

Where $\frac{\partial}{\partial x_i}$ – represents the partial derivative with respect to the spatial coordinates;
ρ_f – is the fluid density, kg/m3;
u_i – represents the velocity components in the i-th direction, m/s;
C_p – is the specific heat at constant pressure, J/(kg·K);
T – temperature, K;
k – is the thermal conductivity, W/m·K;
μ – dynamic viscosity, kg/m·s;
δ_{ij} – is the Kronecker delta, which is 1 when i=j and 0 otherwise.

Turbulent flow model

The Wang-RSM model falls under the Reynolds Stress Models (RSM) category, setting itself apart from other commonly used turbulence models such as the Shear Stress Transport (SST) k-ω model, the Standard k-ω model, and the k-ε mode [47]. The SST k-ω model is a turbulence model that combines two equations, harnessing the strengths of both the k-ω and k-ε models. It utilizes the k-ω model in the vicinity of walls and transitions to the k-ε model in the outer boundary layer. The SST k-ω model is highly esteemed for its ability to accurately predict a wide range of flow patterns and geometries while maintaining robustness. In this research, the author selected the SST k-ω Model, which is particularly well-suited for turbulent flows with significant anisotropy, as commonly encountered in cooling channels. Equations (4.6) and (4.7) outline the SST k-ω Model[103], [104].

$$\rho\left(\frac{\partial k}{\partial t} + u\ \cdot\ \nabla k\right) = \nabla\ \cdot\ \left[\left(\mu\ + \frac{\mu t}{\sigma k}\right)\nabla k\right] + P_k - \beta^*\rho k\omega\ + S \quad (4.6)$$

Where, ***k*** –represents turbulence kinetic energy;
μt – stands for turbulent viscosity denotes the turbulence production term, *kg/m·s*;
β^* – is the is a model constant;
ω – represents the specific dissipation rate, m^2/s^3;

σk – corresponds to the turbulent Prandtl number for k;
S – represents the source term resulting from buoyancy and external forces;
μ – is the dynamic viscosity, *kg/m·s*;
P_k – is the production term of k.

$$\rho\left(\frac{\partial\omega}{\partial t} + u \cdot \nabla\omega\right) = \nabla \cdot \left[\left(\mu t + \frac{\mu t}{\sigma_\omega}\right)\nabla\omega\right] + \beta\rho\left(\frac{\omega}{k}\right) * \left(\frac{P_k}{\omega}\right) - \beta^*\beta\rho\omega^2 + S_t \quad (4.7)$$

Where, ω – presents specific dissipation rate of k,
μ_t – presents turbulent viscosity, *kg/m·s*;
σ_ω – is the turbulent Prandtl number for ω;
St – is the source term due to buoyancy and external forces.
To calculate turbulent viscosity for this model the author used Eq (4.8)

$$\mu t = \frac{\rho C\mu k^2}{\omega} \quad (4.8)$$

Where, Cμ – is constant, typically set to 0.09;
k – is the turbulence kinetic energy, *J/kg*;
ω – is the specific dissipation rate of k;
ρ – is the density, kg/s^3.
To calculate pressure, drop, equation (4.9) employed, which is derived from the Darcy-Weisbach equation [98]. This equation assumes that the flow is fully developed, turbulent, and incompressible and that there are no significant changes in elevation or velocity along the length of the channel.

$$\Delta P = f\frac{L}{D}\frac{\rho U^2}{2g} \quad (4.9)$$

Where, ΔP – is the pressure drop, *Pa*;
f – is the friction factor;
L – is the length of the channel or pipe, *m*;
D – is the diameter of the channel, *m*;
ρ – is the density, kg/m^3;
U – is the mean velocity of the fluid, *m/s*;
g – is gravitational acceleration, m/s^2.

4.5. Heat Transfer Conjugation

Heat transfer conduction involves three distinct physical heat transfer processes: external surface conduction, internal cooling passages, and ducts within the blade structure. In the conjugate approach, both external and internal flows and heat transfers are considered in conjunction with the blade's geometry. Analyzing these three aspects helps determine the temperature distribution within

the blade, which, in turn, defines boundary conditions for simulating heat transfer in metal wires.

For the external flow and heat transfer simulation, boundary conditions are established. Meanwhile, internal boundary conditions for line calculations are determined by simulating the internal heat and fluid flow within the coolant channels. As previously mentioned, performing a 3D simulation of heat transfer in the intricate cooling passages of the blade can be quite time-consuming.

In the Wang experiment, the central vane of the C3X transonic turbine was cooled using air flowing from the hub to the deck through ten circular flow channels. The blade material specified for the experiment was ASTM Type 310 stainless steel, characterized by specific heat (Cp) = 502 J·K/kg, density (ρ) = 8030 kg/m³, and thermal conductivity varying with temperature, as described by equation (4.10) below [47], [65], in

$$K_{ss} = 0.0155T + 9.9105 \ (W.K/m) \tag{4.10}$$

In the simulation, Sutherland's formula was employed to characterize viscosity and thermal conductivity. It's important to note that specific heat capacity, dynamic viscosity (represented as μ), and thermal conductivity (denoted as $\boldsymbol{k_{fg}}$ are all influenced by temperature. Consequently, these properties exhibit temperature-dependent behavior, and their respective values can be determined using formulas that are sensitive to temperature variations. This information is encapsulated in equations (4.11 and 4.12) [105].

$$\mu(T) = \mu_0 \left(\frac{T}{T_0}\right)^{\frac{3}{2}} \times \frac{T_0+s}{T+s} \tag{4.11}$$

.

$$k_{fg}(\mathrm{T}) = \lambda_0 \left(\frac{\mathrm{T}}{\mathrm{T_0}}\right)^{3/2} * \frac{\mathrm{T_0+S}}{\mathrm{T+S}} \tag{4.12}$$

Where μ_0 – reference dynamic viscosity,*Pa.s*;

T_0 – reference temperature, *K*;

λ_0 – reference thermal conductivity, *W/(m·K)*;

S – Sutherland's constant.

The dynamic viscosity of the fluid, denoted as μ(T), is a key parameter in fluid dynamics,

representing the fluid's resistance to shear or flow. It is calculated based on a reference dynamic viscosity, μ_o, which is set at 1.7894 x 10^{-5} *Pa.s*. This reference value corresponds to a specific reference temperature, T_o, established at 273.11 K. The temperature of the fluid, represented by T, plays a crucial role in determining the actual dynamic viscosity. Additionally, the equation incorporates Sutherland's constant, denoted as S, which is a fluid-specific value and integral to the calculation. For the fluid in question, Sutherland's constant is determined to be 110.56. This constant is pivotal in adjusting the viscosity calculation to accommodate variations in temperature, ensuring accuracy in the fluid's behavior analysis under different thermal conditions. Where is the thermal conductivity of the fluid, represented as $k_{fg}(T)$, is a fundamental parameter in the study of fluid dynamics, characterizing the rate at which heat is conducted through the fluid. This property is particularly crucial in applications involving heat transfer and energy exchange.

To accurately assess $k_{fg}(T)$, we establish a reference point known as λ_0, the reference thermal conductivity. This reference value is essential for comparative and baseline measurements. For the purposes of our analysis, λ_0 is set at 0.0261 *W/(m·K)*, offering a standardized measure against which the thermal conductivity of the fluid at varying temperatures can be evaluated.The Reynolds Number and hydraulic diameter were computed for every cooling hole, relying on parameters such as the fluid mass flow rate (ṁ), hydraulic diameter of the cooling channel (D_C), coolant viscosity (μ), and coolant density (ρ). This calculation aimed to ensure that the outlet pressure matched the NASA C3X data, necessitating the adjustment of the inlet Reynolds number (R_e). The Reynolds number plays a pivotal role in shaping the flow behavior within each cooling channel. In cases where the flow becomes turbulent, it is more conducive to achieving maximum heat transfer. However, turbulent flow also gives rise to transitional flow regimes. When the flow operates in a transitional regime, it can pose challenges for simulations to accurately predict the flow patterns and heat transfer within the cooling system. The coolant's inlet Reynolds Number (R_e) was determined based on the hydraulic diameter (D_C) of each channel, employing the equation presented below. Equation (4.13) serves as a tool to delineate the characteristics of each cooling passage.

$$R_e = \frac{\frac{\dot{m}}{A} D_C}{\mu} \tag{4.13}$$

Where, ṁ – mass flow rate, *kg/s* ;

μ – fluid viscosity, *kg/m·s*;

D_c – is the cooling channel's hydraulic diameter, *m*.

A – is the area, m^2

The 3D computational domain for simulating heat transfer around the NASA C3X plate was created and utilized for validation purposes to confirm the distribution of heat transfer coefficients around the plate. This domain, specifically designed for the conjugate heat transfer simulation, is illustrated in Fig. 4.3.

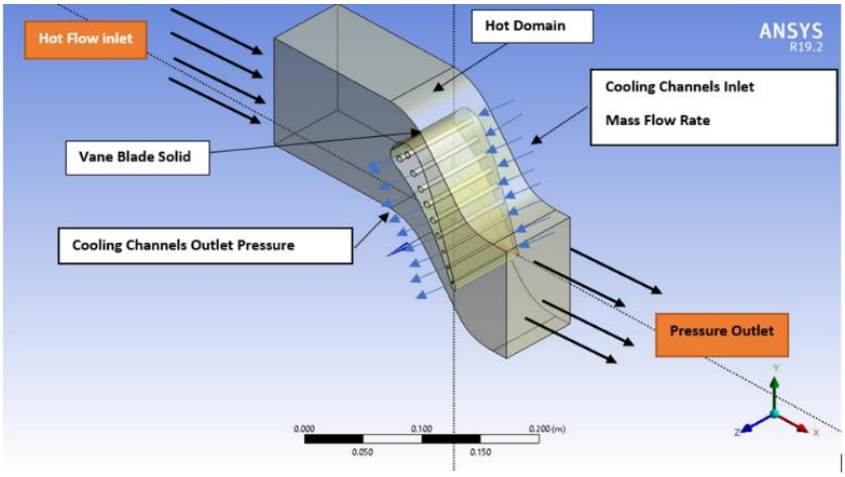

Fig. 4.3 The 3D domain for the conjugate heat transfer simulation.

In the present study, Computational Fluid Dynamics (CFD) was employed along with a range of meshing techniques, including prism layer meshing, polyhedral mesh, and generalized cylinder mesh, to devise and evaluate various cooling configurations within a gas turbine blade. The primary objective was to optimize cooling efficiency while minimizing its impact on the thermodynamic system, quantified through the heat transfer coefficient (HTC). The average heat transfer coefficient (HTC) is a crucial parameter in the design of cooling systems for gas turbine blades. It quantifies the amount of heat transferred from the metal to the coolant and is typically expressed in units of W/m^2-K. Several factors influence the HTC, including fluid properties, flow conditions, and geometric parameters of the cooling system.

Additionally, the study conducted a comparative analysis of its findings with data from earlier research conducted by Hylton and Wang. The calculation of the heat transfer coefficient (HTC) for each cooling channel was carried out using the Nusselt Number equation Eq (4.14)[70].

$$N_{u0} = Cr\left(0.022 p_r^{0.5} R_e^{0,8}\right) \quad (4.14)$$

Where, *Cr* – is correction coefficient;

P_r – Prandtl Number;

R_e – is Reynolds Number.

The Nusselt number (Nu) equation, which relates the HTC to fluid properties and flow conditions, is commonly employed to calculate the HTC. This equation incorporates key parameters such as the correction coefficient (Cr), Prandtl number (P_r), and Reynolds Number (R_e) to account for the effects of fluid properties, flow conditions, and geometric parameters on the HTC. The calculated HTC values using the Nu equation enable comparisons of cooling performance among different cooling configurations and facilitate the optimization of cooling system designs for improved thermal performance.

To determine the Nusselt Number (Nu), various assumptions were made in this analysis. The convective heat transfer coefficient was subsequently computed using the Nu equation, assuming steady and uniform heat flow around the vane. Additionally, it was assumed that the Hylton experimental temperature data was subject to a specified temperature boundary condition. For the reported heat transfer calculations, a constant thermal load was applied by [47], [65].

Finally, the heat transfer coefficient varies based on cooling channel parameters, including diameter and Reynolds Number. To account for these variations in heat transfer coefficients among cooling channels, predictions regarding various coolant characteristics were necessary. For instance, it was assumed that the inlet flow temperature remains uniformly constant as specified by [47], [51], [65], [70]. The number is defined above, and the Prandtl number is as follows in Eq (4.15) [70].

$$P_r = \frac{c_p \mu}{k_{fg}} \quad (4.15)$$

Where, *Cp* – represents the coolant's specific heat capacity, *J/(kg·K)*;

μ – fluid viscosity, *kg/m·s*;

k_{fg} – thermal conductivity which are all represented by Sutherland's Law, as illustrated above, *W/m·K*.

The heat transfer coefficient was then determined using the Nu, as shown in Equation (4.16) below:

$$h = \frac{k_{fg} N_u}{Dc} \quad (4.16)$$

Where, k_{fg} – is thermal conductivity, *W/m·K* ;

D_c – is the cooling channel's hydraulic diameter, *m*.

The heat transfer coefficient can be lowered to Eq. (4.17) by combining Eqs. (4.11), (4.15), and (4.16) [47], [65]:

$$h = 0.02424 \cdot C(\lambda, \dot{m}, \mu) D_C^{-1.8} \tag{4.17}$$

Where, λ – thermal conductivity, *W/(m·K)*;

$\dot{m}$ – mass flow rate, *kg/s* ;

μ – fluid viscosity, *kg/m·s*;

D_c – is the cooling channel's hydraulic diameter, *m*.

In Eq. (4.18), C represents the coefficient associated with a cooling channel and is assumed to be a constant cause of the coolant assumptions mentioned previously.

$$\boldsymbol{C(\lambda, \dot{m}, \mu) = \lambda \cdot (\frac{\dot{m}}{\mu})^{0.8}} \tag{4.18}$$

The C.S. calculated the HTC using Newton's law of cooling. The heat transfer coefficient is calculated by Ansys using the following equation (4.19):

$$\boldsymbol{h = \frac{(q'' \, conduction \, (a))}{[|a| \, T_S - T_w)]}} \tag{4.19}$$

Where T_S – is the standard temperature, *K*;

T_w – is the boundary temperature, *K*.

where it was supposed to be the average volume, and mean bulk temperature for the fluid of the individual channel, T_w is the boundary temperature, for the wall and $\frac{(q'' \, conduction \, (a))}{[|a|\,]}$ is the vector field's heat flux boundary conduction. The heat flux at the boundary considers both molecular and turbulent diffusion effects at the fluid's boundaries. This analysis was conducted to predict the average heat transfer characteristics of each cooling channel, and the results regarding the average heat transfer coefficient (HTC) of the cooling channel are presented in the results section.

4.6. Boundary Condition

C3x boundary condition taken from C3X cascade test conditions code 4311, run 148 [51], Tables 8, and 9 present the boundary condition which the authors used for simulation.

Table 8.

Boundary condition for the domain.

P_0	T_0	M_i	l	T_u	T_w/T_g	M_e (x=0.09836)
321KPa	802K	0.17	0.016m	6.5%	0.73	0.9

Table 9

Cooling channels input boundary conditions.

Channel	Mass flow rate(kg/s)	T_{in}(K)
1	0.022	342
2	0.0221	344
3	0.0218	335
4	0.0218	336
5	0.0225	330
6	0.0225	355
7	0.0216	336
8	0.00744	350
9	0.00477	377
10	0.00256	387

4.7. Base Model Meshing

Achieving mesh independence is a crucial step in CFD simulations, especially in conjugate heat transfer (CHT) analyses. Mesh independence implies that the simulation's results should remain relatively stable regardless of changes in mesh density or geometry, converging to the same solution. To achieve mesh independence, various meshing techniques were employed, including prism layer meshing, polyhedral meshing, and generalized cylinder meshing.

The prism layer mesh is utilized to improve the accuracy of the flow model near wall surfaces and boundaries by creating prismatic cells that are orthogonal to these surfaces. This approach enhances simulation accuracy, especially in areas where the flow experiences high viscosity near walls. Polyhedral meshes and generalized cylinder meshes were also employed to generate high-quality meshes suitable for CHT analysis. These mesh types address the challenges of mesh generation by creating extruded meshes along regions resembling generic cylinders. This is particularly useful for simulating complex geometries or regions with significant curvature.

Additionally, the control volume option in Ansys ICEM was utilized to refine or coarsen

specific areas of the mesh as needed. This feature allows for precise control over mesh density in regions where flow or heat transfer is of particular importance or where sensitivity to mesh density is expected. The mesh was generated using ANSYS ICEM with the Tetrahedron method, a maximum growth rate of 1.2, and a selected curvature normal angle of 18 degrees. The resulting mesh consisted of 3,184,243 elements and 682,571 nodes. Inflation was applied with a first-layer thickness of 0.0021 mm and a total of 10 layers. This inflation is crucial for CHT accuracy.

Fig. 4.4 depicts the blade with the flow domain after meshing, while Fig. 4.5 showcases the meshing for the cooling channels. It's important to note that momentum and scalar transports are most active in near-wall regions, where solution variables exhibit larger gradients. The inner layer in this case consists of three zones with corresponding wall Y+ values, which represent non-dimensional distances. Y+ values are categorized as follows: Y+ less than 5 for the viscous sublayer, Y+ between 5 and 30 for the buffer layer or blending region, and Y+ between 30 and 60 for fully turbulent flows. In this case, a Y+ value of 1 was chosen for the assumed viscous sublayer, indicating its high resolution for accurate CHT simulations.

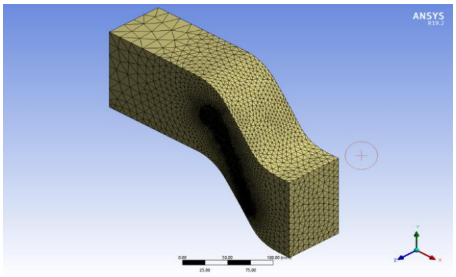

Fig. 4.4. Fluid domain meshing.

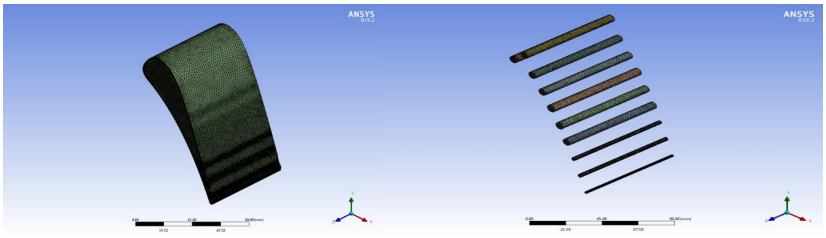

(a) (b)

Fig. 4.5 Full NASA C3X meshing: (a) Full NASA C3X meshing; (b) Base model cooling channels Meshing.

The aspect ratio is a critical parameter in meshing, and it is typically recommended to maintain an aspect ratio between 1.5 to 2.0. This suggests that the ratio of the longest edge to the shortest edge of mesh elements should not exceed 2.0. However, specific applications may permit higher aspect ratios, while others may demand significantly lower aspect ratios, depending on the precision and stability criteria. Fig.4.6 provides a visual representation of the aspect ratio metric, and the graph illustrates that the maximum elements in the mesh exhibit an average aspect ratio of 8.

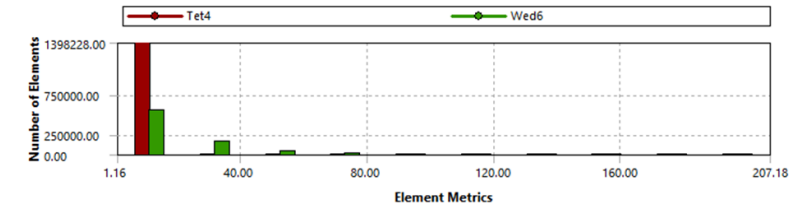

Fig. 4.6. Aspect ratio mesh.

4.8. Optimized Model Configuration

In the current study, the optimized jet impingement type configuration was designed with the objective of increasing cooling effectiveness while maintaining similar pressure drops compared to the base model. The results demonstrated that the optimized jet impingement type configuration successfully improved cooling effectiveness by enhancing the heat transfer coefficient and reducing the temperature at the blade's leading edge. This underscores the significance of considering jet impingement parameters in the design of cooling systems for gas turbine components.

Utilizing the same meshing approach as the base model and drawing from Glynn's research [95], it was confirmed that heat transfer can be enhanced by reducing the jet nozzle diameter. It is essential to carefully determine jet impingement parameters such as the position and diameter of the jet nozzle. According to Yamane's experiments, the H/DJ Ratio should fall between 2 to 8, where H represents the distance between the nozzles and DJ is the jet diameter. By selecting a jet diameter of 1.94 mm, the H/DJ ratio reached 8, aligning with the recommended ratio based on Yamane's Experiment [90]. Additionally, the jet spacing, expressed as the S/DJ ratio, should be within the range of 4 to 8. The determination was made to set the jet spacing at 11.44 mm, resulting

in an S/DJ ratio of 5.89. Fig. 4.7 presents the flow domain and optimized turbine blade cooling channel (jet impingement type).

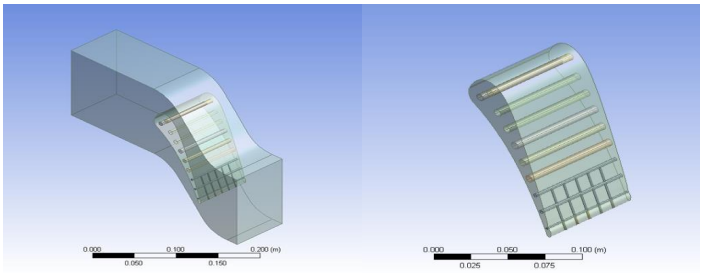

(a) **(b)**

Fig. 4.7. Flow domain and optimized turbine blade cooling channel model: (a) Hot domain configuration; (b) Optimized turbine blade cooling channels.

Mesh generation was conducted using Ansys ICEM, employing identical mesh configuration as the base model. The CFD simulation was performed with the same boundary conditions that were applied to the base model.

4.9. Validation of the flow domain

Fig. 4.8 illustrates the domain of absolute pressure flow, providing insights into the pressure distribution across the vane's surfaces. On the vane's suction side, which is situated in the channel throat area characterized by high flow velocity, the pressure is at its lowest. Conversely, at the stagnation point found at the vane's leading edge, the pressure reaches its highest point. As one moves from the leading edge towards the trailing edge on the pressure side, there is a gradual increase in velocity accompanied by a gradual decrease in pressure. However, in proximity to the suction surface, the velocity initially rises but then diminishes due to adverse pressure gradients resulting from secondary flows. This can lead to boundary layer separation near the trailing edge of the suction-side blade surface, a significant contributor to profile losses in high-loading blades or vanes.

The elevated loading on the suction side contributes to a reduction in suction-side pressure, allowing for an increase in local Mach number and velocity, ultimately leading to the development of supersonic speeds. As the flow approaches supersonic velocities, local shockwaves form, resulting in additional aerodynamic losses such as shock losses or wave drag. It is important to note

that the suction surface pressure increases in regions characterized by unfavorable pressure gradients and downstream of the shock within the boundary layer.

.

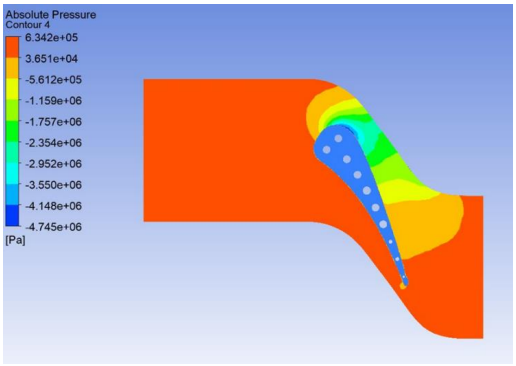

Fig. 4.8. CFD absolute pressure flow domain.

4.10. Results

The present study under discussion involves a comparison of outcomes derived from various cooling configurations through the utilization of CFD simulations, employing Helton's NASA Model and Wang's CFD. This comparative analysis will be structured into three distinct sections, each dedicated to specific cooling configurations and their notable attributes. Additionally, the study will showcase data collected and evaluated within its scope, encompassing contour plots illustrating temperature, pressure, and heat transfer calculations. This comprehensive comparison aims to pinpoint the most efficient cooling configuration while offering valuable insights for enhancing the performance of gas turbine blades and vanes.

4.10.1. Configuration Of Base Model

In this study, graphical representations are presented to compare the mean gauge pressure, mean temperature, and heat transfer coefficient data obtained from Hylton's dataset with the data generated from the current base model. This comparison was achieved by aligning similar span vs. axial cord positions (x vs. l) with the sensor locations in the Hylton dataset, enabling the display of corresponding means at those positions [51]. Fig. 4.9 displays the Normalized C3X span

coordinate. To standardize the data, the parameter $p/p*$ was calculated using Hylton's inlet conditions, which were conducted at a nominal gas-stream total temperature of 811 K. Fig. 4.10 presents the mean gauge pressure data for the base model. This comparison serves to evaluate the accuracy of the current CFD model in comparison to the NASA model, and it enables an assessment of the correlation between the two datasets, thereby validating the results obtained in the current study. It's worth noting that Hylton's NASA data is widely recognized as a benchmark in the aeronautical industry, and any alignment between the current study's data and the NASA data enhances the credibility of the current study's results when compared to the C3X Vane Data.

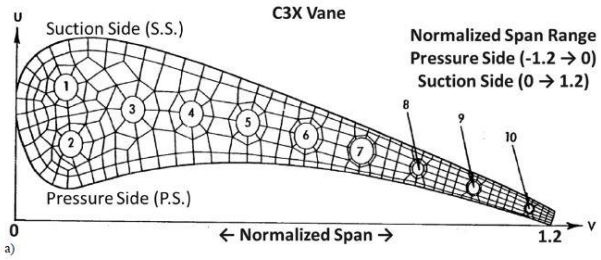

Fig. 4.9. Normalized c3x vane span coordinate [51].

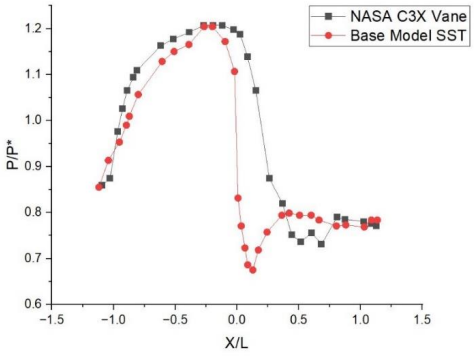

Fig. 4.10.Base model mean gauge pressure data compared with C3X data.

In Fig. 4.10 of the current study, a comparison is presented between the temperature distribution data from the study and Helton's NASA C3X model Experiment data[51]. This comparison is normalized between t/811 to mid-span. Additionally, Fig. 4.12 showcases the

distribution of local heat transfer coefficients over the mid-span of the turbine blade. The analysis of the temperature distribution comparison allows for an assessment of the correlation between the two datasets and the accuracy of the current CFD model. It's worth noting that the pressure side of the vane aligns with the Hylton trend, but the current study predicts an overestimated heat transfer coefficient in the vane head and most of the suction side. The discrepancy in average h between the two models is 23.36%, which can be attributed to the various assumptions and simplifications in the current CFD model, as well as potential experimental errors in the NASA data. However, this difference falls within an acceptable range, indicating that the study's results are reliable and precise.

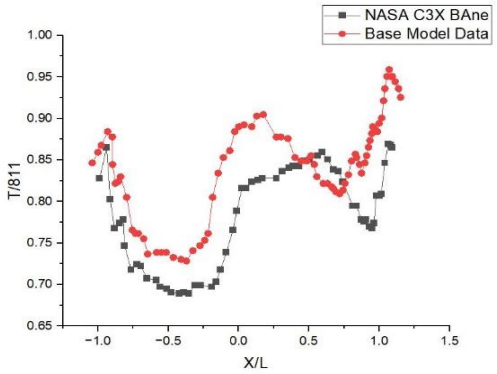

Fig. 4.11. Base model temperature comparison with NASA C3X experimental data.

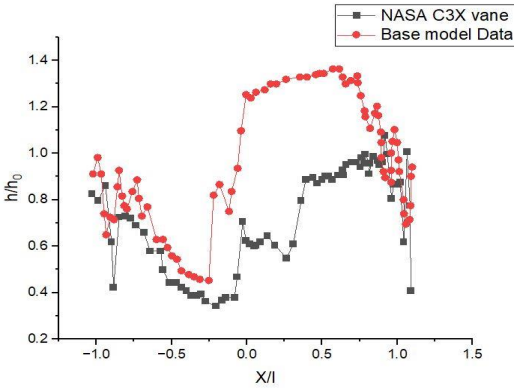

Fig. 4.12. Average heat Transfer coefficient comparison.

Fig. 4.13 in this current study, the temperature distribution in (K) is depicted from the top

view of the basic blade model configuration. Both models exhibit a similar temperature profile with slight variations. However, the current model indicates a higher temperature profile, particularly towards the edge regions, which is most pronounced on the blade's suction side. These distinctions arise from the limitations inherent in CFD simulations, as previously discussed. Notably, the temperature at the blade's center is elevated, ranging from 10 to 35K. Nevertheless, the temperature contours in both investigations follow the same overall pattern, with the vane's trailing edge displaying the highest temperature, exceeding 670K. By comparing the CFD results of the current study with those of the NASA model, as well as with the studies by Wang and Rossman, we can assess the degree of correlation between the two datasets and evaluate the accuracy of the current CFD model. This can assess the correlation between the two datasets and the accuracy of the current CFD model [106]. Figure 4.13 provides visual representations of the temperature contours generated in the current study's baseline for the three configurations. The minor discrepancies observed between the two sets of data can be attributed to the diverse assumptions and simplifications incorporated into the CFD model of the current study, as well as the potential presence of experimental errors in the NASA dataset[47], [51], [65], [70]Top of Form

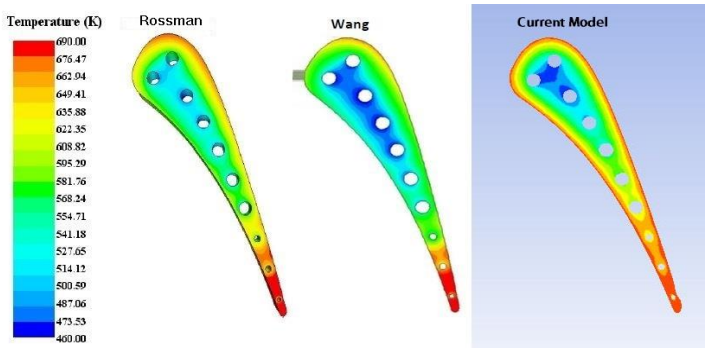

Fig. 4.13.. Base model mean temperature data comparison between the reference data.

4.10.2. Trailing Edge Focus

In this section of the study, recent data is employed to underscore the vital importance of adopting a jet impingement type configuration to enhance the cooling of turbine blade trailing edges. This configuration yields significantly lower temperatures compared to the baseline case, which exhibits a temperature range of 633K to 685K, as depicted in Fig. 4.14. The comparison

clearly illustrates the advantages of employing a jet impingement type cooling setup, particularly in dissipating heat at the vane's trailing edge, where temperatures reach their peak. This information holds crucial implications for the design and optimization of cooling systems for turbine blades and vanes, as it highlights the potential for a triple impingement cooling configuration to greatly improve the performance and efficiency of gas turbine engines.

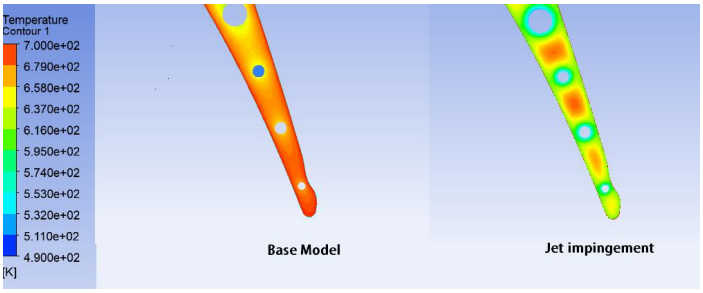

Fig. 4.14.Trailing edge temperature comparison between NASA base model and jet impingement type cooling channels.

In the current study, the network impingement arrangement demonstrates even cooler temperatures than the Base model. It ranges from 545K to 598K, which is 3.1% to 3.9% cooler, and the vane itself is 14.7% to 20% cooler compared to the original NASA C3X vane. Notably, the largest temperature drop is observed at the trailing edge's tip, as depicted in Fig. 4.15. In the base model, the vane's tip reaches a temperature of 700K, while its trailing edge tip registers at 652.75K.

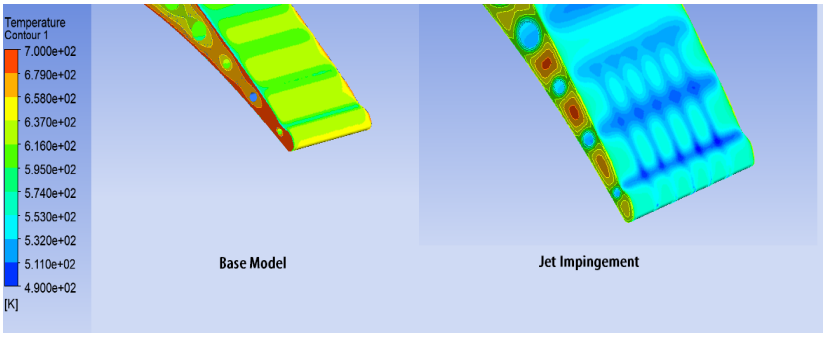

Fig. 4.15. Trailing edge temperature comparison between NASA base model and jet impingement type cooling channels.

This represents a substantial 18.3% reduction in temperature compared to the baseline and

network cooling jet impingement type. This underscores the effectiveness of the jet impingement type cooling configuration in dissipating heat from the vane's hottest region, the trailing edge, leading to enhanced performance and efficiency in gas turbine engines. Figure 4.16 illustrates the variation in temperature along the channel walls, with the average temperature ranging from 540 K to 580 K. This highlights the significant enhancement in heat transfer efficiency at the leading edge of the turbine blade.

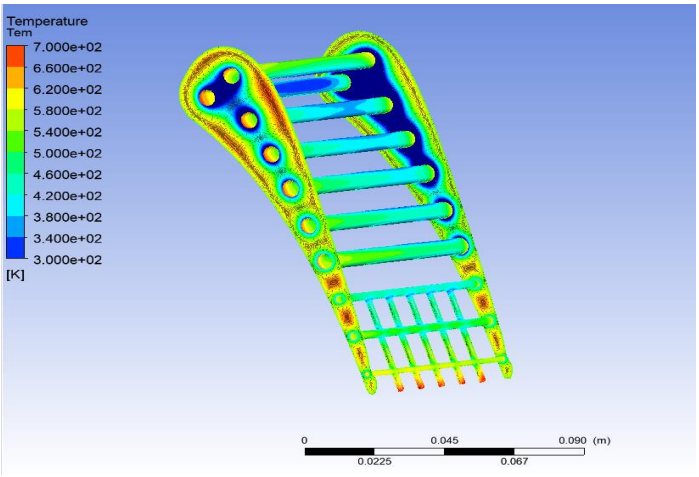

Fig. 4.16 Temperature contours for the cooling channels in the turbine blade wall.

The Jet impingement type configuration proves to be an efficient approach for lowering the temperature at the trailing edge tip of a turbine vane, a critical area prone to failure under high temperatures. The noteworthy 32.20% reduction in temperature at the trailing edge tip when compared to the baseline configuration, along with an 18.95% decrease compared to the NASA model configuration, signifies a substantial enhancement in the turbine's thermal performance. This improvement has the potential to significantly prolong the lifespan of the turbine components.

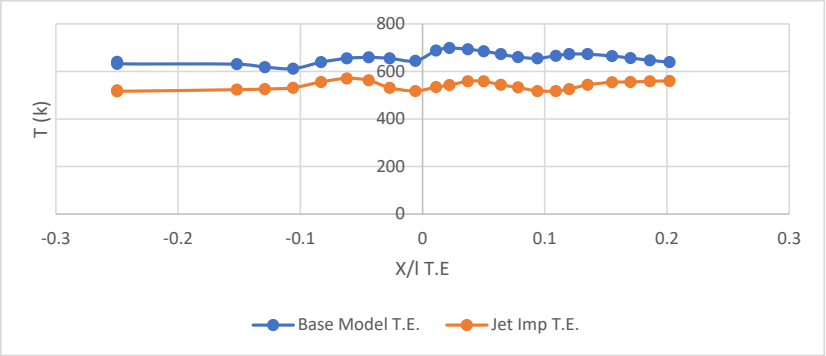

Fig. 4.17. Trailing edge temperature comparison between NASA base model and jet impingement type cooling channels.

Fig. 4.17 illustrates that among the three configurations examined in the study, the Jet impingement type configuration was most effective in lowering the temperature across the vane. The temperature distribution in this configuration was notably cooler compared to the other two, indicating its superiority as a cooling method. Such efficient cooling is crucial for mitigating issues like degradation, corrosion, and vane failure, which typically arise under high-temperature conditions.

4.11. Conjugate Heat Transfer

This text segment outlines an upcoming comparison between the calculated and measured average heat transfer coefficients for each cooling channel. The specific equations slated for use in these calculations are designated as Equations (4.14–4.20). These equations are presumably formulated to compute the heat transfer coefficient employing various methods or models.

The purpose of this comparison is multifaceted. Primarily, it aims to assess the precision and dependability of the calculated results in comparison to experimental measurements. This evaluation serves to verify the effectiveness and accuracy of the equations employed. Additionally, comparison is instrumental in identifying any variances or inconsistencies between the calculated and measured values.

Such a comparative analysis is crucial, as it may lead to adjustments or enhancements in the equations or models currently used for calculations. These refinements are essential for improving the accuracy and reliability of future calculations, ensuring they more closely align with

experimental observations and real-world data.

Fig. 4.18 presents a graphical comparison of the average heat transfer coefficients (HTC) as calculated in different studies. The accompanying caption elucidates the graph's contents. It's noted that the HTC in the current study's Computational Fluid Dynamics (CFD) baseline case is slightly under-predicted for the first eight cooling channels. However, this under-prediction becomes more noticeable near the trailing edge of the vane. This observation aligns with the principle that HTC varies with the hydraulic diameter of the cooling channel, a concept grounded in the fundamentals of heat transfer and fluid dynamics.

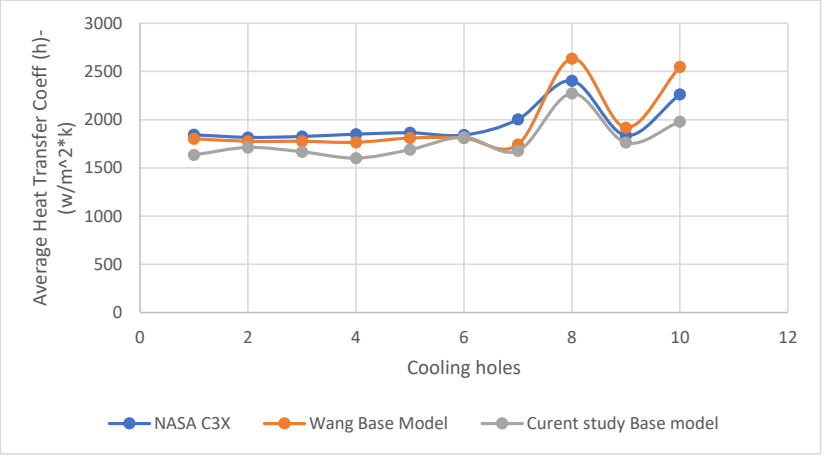

Fig. 4.18. Average heat transfer coefficient comparison between NASA C3X experiment data, Wang experiment data [48], and current study base model.

This section also delves deeper into the specifics of the cooling channels, noting their differences across various studies. A significant reduction in the hydraulic diameter of these channels (by approximately 59.70%-69.55%) is observed as they near the vane's trailing edge. This change is consequential for the performance of the cooling system and the heat transfer coefficients.

Additionally, the passage underscores differences in HTC values among various studies. These variations range from 2.9-15% between the Hylton's original C3X computed data and the current study's CFD baseline case. Moreover, a difference of 2.4-26% is noted between the current study's CFD baseline case and Wang's computed data regarding cooling channel heat transfer coefficients. These findings highlight the pivotal role of cooling channels near the vane's trailing edge in influencing the heat transfer coefficient. They also illustrate that the results of the current

study's CFD model significantly differ from previous studies, particularly in how they model and understand the cooling channels' impact on heat transfer.

This study highlights key distinctions from previous research, notably the departure from the fully developed flow assumption. Unlike prior studies, this research does not presume that the flow within the cooling channels has attained a steady state, with constant velocity and temperature profiles throughout. Instead, it accounts for variations in Reynolds Numbers across individual cooling channels, which can influence heat transfer coefficients.

The focus of this study is a comparative analysis of two different cooling configurations: the Base Model and the Jet Impingement type. The methodology involves calculating the average heat transfer coefficient (HTC) for each cooling channel using a specific method or equation. The findings, as presented in Fig. 4.19, delineate the differences in average HTC for each cooling channel between the two configurations. This comparative approach sheds light on the impact of the Jet Impingement type configuration on the cooling efficiency of the channels and its comparative performance against the Base Model.

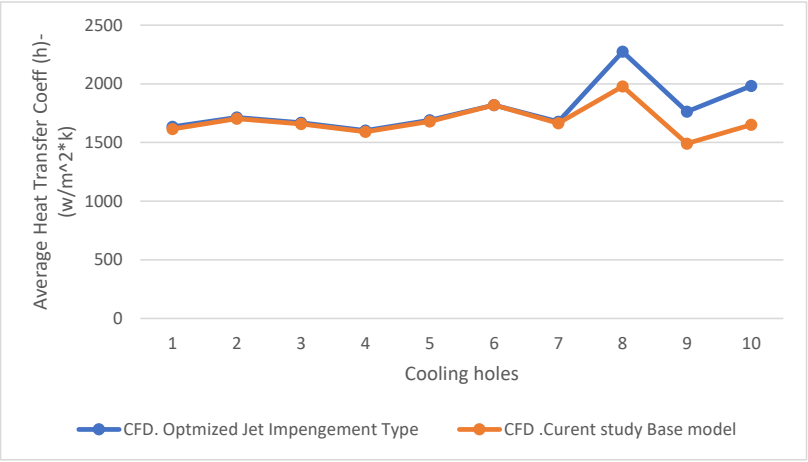

Fig. 4.19. Average heat transfer coefficient comparison between NASA base model, and jet impingement type.

Fig. 4.19 reveals a minimal variance in the average HTC for the cooling holes between the Base Model and Jet Impingement type configurations, with differences ranging from 0% to 5%. Despite expectations, channels 8/9/10, located in the jet impingement type cooling channels, did

not show significant differences. This outcome might be influenced by various factors, such as the cooling holes' geometry, the flow's Reynolds number, or the applied heat transfer model.

The comparative analysis assists in understanding how the Jet Impingement type configuration influences cooling performance. It helps identify which channels exhibit the most notable differences in heat transfer coefficient between the two configurations. Additionally, Fig. 4.20 compares the blade wall heat flux between the NASA Base Model and the optimized model, further contributing to the study's comprehensive analysis of cooling configurations.

.

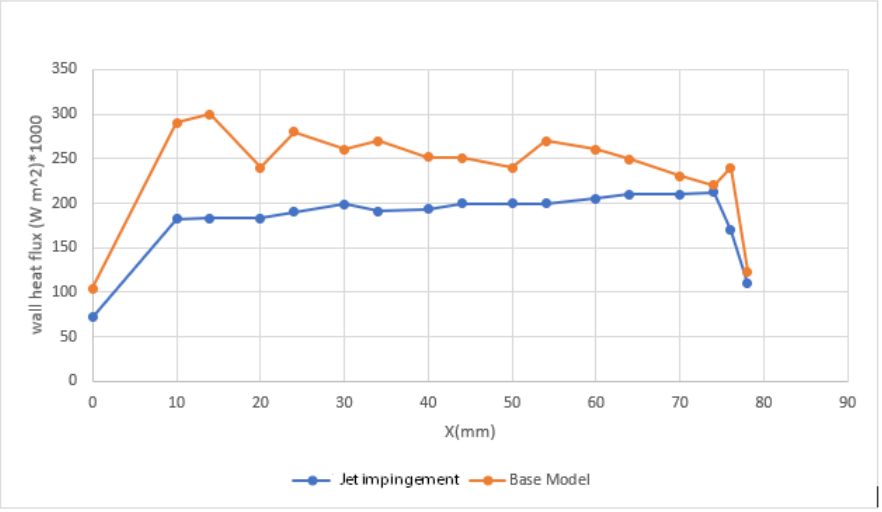

Fig. 4.20. Blade wall heat flux comparison between NASA base model, and optimized model.

4.12. Determination Of Cooling Effectiveness for the Optimized Model

Mathematical Eq (4.20) is used to calculate the cooling effectiveness (φ) of a forced convection heat transfer system, such as a turbine blade cooling channel [57]. The equation considers the temperature difference between the coolant and the wall, the Reynolds number, and the Prandtl number. The general equation is.

$$\varphi = \frac{T_{gas} - T_{metal}}{T_{gas} - T_{c,in}} \tag{4.20}$$

Where T_{gas} – is the temperature of the gas in the fluid domain, K;

T_{metal} – is the temperature of the solid which is the blade in our study, K

T_C, – is the temperature of the coolant which in our case is cold air, K.

By analyzing the cooling effectiveness of a turbine blade with a triple impingement system compared to a standard system, it becomes possible to assess the effectiveness of the optimized jet impingement system in enhancing blade cooling while minimizing losses to the overall turbine system. Cooling effectiveness values serves as a key metric to gauge improvements in cooling and aid in the optimization of the cooling system design for peak performance.

Engineers can use these cooling effectiveness values to identify the most effective design for the turbine blade cooling system. Ensuring the blade operates within safe temperature ranges is crucial for the turbine's longevity and reliability. For these calculations, the average coolant temperature is used as the inlet temperature for the cooling channels, while the metal temperature represents the solid blade temperature, and the gas temperature indicates the hot fluid's temperature. These parameters are standard inputs for calculating cooling effectiveness.

Upon evaluating the cooling effectiveness for the base model and the optimized jet impingement type, a value of 0.48 was found for the entire blade. This was compared to the cooling effectiveness of the optimized jet impingement model, which stood at 0.69. The comparison reveals that the optimized model significantly improves cooling effectiveness. Specifically, there is a 29% increase in cooling effectiveness for the entire blade and a 28 % increase for the trailing edge. These findings underscore the significance of implementing optimized cooling designs in turbine blades, crucial for maintaining their efficient and safe operation.

4.13. Summary Of Chapter 4

The study under discussion revealed a higher temperature profile, particularly near the edge areas of the blade, most notably on its suction side. This variation is attributed to the limitations of Computational Fluid Dynamics (CFD) simulations. In the blade's center, temperatures were found to be elevated, ranging between 10 and 35K higher. Despite these differences, the temperature contours in both the current study and the referenced NASA model displayed similar characteristics, with the vane's trailing edge showing the highest temperature, around 670+K. This comparative analysis between the CFD results of the current study and NASA's model data allows for an evaluation of the correlation and accuracy of the current CFD model. The minor

discrepancies observed between the two data sets could be due to the assumptions and simplifications in the CFD model of this study, as well as potential experimental errors in NASA's data.

In this study, ANSYS FLUENT code was utilized for CFD solving, and ANSYS ICEM-CFD was employed for mesh generation. ANSYS FLUENT is a widely recognized commercial CFD software, capable of handling various fluid flow and heat transfer problems, while ANSYS ICEM-CFD is adept at generating high-quality meshes for CFD simulations. These tools were used to conduct detailed CFD simulations of gas turbine blade cooling configurations.

Focusing on the trailing edge of the vane, as illustrated in Fig. 4.13 using a third of the standardized span data, temperatures ranged from 540K to 617K, starting from the last three segments and sub-holes. This is significantly cooler than the basic case, which ranged from 633K to 685K, underscoring the effectiveness of jet impingement cooling configurations in heat dissipation at the blade's trailing edge.

The study also provided insights into the cooling channels, noting a considerable reduction in their hydraulic diameter (between 49.70%-69.55%) near the vane's trailing edge, impacting heat transfer coefficients and cooling system performance. Additionally, it noted differences ranging from 2.9-15% between the Hylton model, original C3X calculated data, and the current study's CFD baseline case. Furthermore, the study's CFD baseline case varied from Wang's computed data by 2.4-26% in terms of cooling channel heat transfer coefficients.

The study observed that the pressure side of the blade aligns with the Hylton model, while the current study anticipates a higher heat transfer coefficient around the blade head and most of the suction side. The average heat transfer coefficient differed by 23 % between the two models.

For the optimized jet impingement type, a cooling effectiveness of 0.4892 was recorded for the entire blade, compared to 0.6936 for the optimized jet impingement model. This suggests that the optimized model significantly enhances cooling effectiveness, by 29% for the whole blade and 28 % for the trailing edge, indicating that optimized jet impingement designs offer superior cooling performance. These findings emphasize the necessity of optimized cooling designs in turbine blades for efficient and safe operations.

Even though the Jet impingement cooling channels provide excellent means of heat transfer and blade cooling, however, there may be structural and manufacturing challenges to physically implement in the turbine blade. This limitation indeed does not affect the significance of the results

achieved in this thesis, however, in the future, this research can be continued for experimental analysis and to overcome the manufacturing constraints by implementation of modern 3D printing based additive manufacturing techniques.

GENERAL CONCLUSIONS

This doctoral thesis represents a substantial achievement in the field of aeronautical engineering, particularly in the design and analysis of cooling systems in gas turbine blades for civil aviation aircraft engines. The study covered several aspects for improved turbine blade cooling, such as: improved cooling channel designs, numerical evaluation of heat and temperature variations in turbine blade, integration of MATLAB coding in assessing the heat transfer using Computational Fluid Dynamics and optimized geometric configuration of Jet Impingement type cooling channel for the enhanced cooling of the blade flow.

Key achievements of the thesis include:

1. The evaluation of engine failures, particularly in the High-Pressure Turbine (HPT) section of CF6 engines installed on B747 aircraft, was conducted using EGT margins and BI data. This analysis provided the critical factors which contribute to engine degradation and the impact on its operational lifespan and maintenance costs.
2. In the CF6 engine study, a thorough examination of EGT margins provided valuable insights into engine performance deterioration. By analyzing a wide array of engine parameters, the study offered a view of the factors affecting engine health. This provided the basis for the cooling channel research.
3. From CFD analysis by utilizing ANSYS FLUENT and ANSYS ICEM, the research provided a detailed examination of various cooling channel configurations. This rigorous analysis has led to the identification of optimal designs of cooling channels with enhanced thermal performance and reduced drag, contributing significantly to overall turbine blade cooling.
4. MATLAB codes which were developed specifically for the cooling channel thermal performance analysis, provided significant way of comparing the simulated results (of the author) with the experimental data in the literature.
5. Jet impingement type cooling channels were specifically designed for this doctoral thesis. The findings based on the Nusselt number ratio, Reynolds Number effects, and thermal performance provide enhanced heat transfer effects within the blade channel.
6. This computational study compared the results of the designed cooling channels with the experimental results available in the literature for the NASA C3X turbine

blade. This comparative analysis not only validates the results of the previous studies but also provides the new design methodologies for the cooling channels leading to improved temperature profiles and profiles and heat transfer coefficients in turbine blades.

7. Even though the Jet impingement cooling channels provide excellent mean of heat transfer and blade cooling, however, there may be structural and manufacturing challenges to physically implement in the turbine blade. This limitation indeed does not affect the significance of the results achieved in this thesis, however, in the future, this research can be continued for experimental analysis and to overcome the manufacturing constraints by implementation of modern 3D metal printing based additive manufacturing techniques.

REFERENCES

[1] W. L. Shirk, 'The Robert Barber, Jr. House: A Relic of Quaker Hegemony'.

[2] Tony Giampaolo, *Gas Turbine Handbook*, 3rd Edition. The Fairmont Press, Inc., 2006.

[3] A. F. El-Sayed, *Aircraft Propulsion and Gas Turbine Engines, Second Edition*. CRC Press, 2017. doi: 10.1201/9781315156743.

[4] P. Sturesson, 'Sense, Actuate and Survive - Ceramic Microsystems for High-Temperature Aerospace Applications', 2018.

[5] J. C. Williams and E. A. Starke, 'Progress in structural materials for aerospace systems11The Golden Jubilee Issue—Selected topics in Materials Science and Engineering: Past, Present and Future, edited by S. Suresh.', *Acta Mater*, vol. 51, no. 19, pp. 5775–5799, Nov. 2003, doi: 10.1016/j.actamat.2003.08.023.

[6] M. Morsy El-Gohary, 'Overview of past, present and future marine power plants', *Journal of Marine Science and Application*, vol. 12, no. 2, pp. 219–227, Jun. 2013, doi: 10.1007/s11804-013-1188-8.

[7] P. Mir-Artigues, P. del Río, and N. Caldés, *The Economics and Policy of Concentrating Solar Power Generation*. Cham: Springer International Publishing, 2019. doi: 10.1007/978-3-030-11938-6.

[8] 'NASA/Glenn Research Center', May 2015.

[9] L. Gallar, C. Calcagni, V. Pachidis, and P. Pilidis, 'Development of a One-Dimensional Dynamic Gas Turbine Secondary Air System Model—Part I: Tool Components Development and Validation', in *Volume 4: Cycle Innovations; Industrial and Cogeneration; Manufacturing Materials and Metallurgy; Marine*, ASMEDC, Jan. 2009, pp. 457–465. doi: 10.1115/GT2009-60058.

[10] H. Dai, J. Zhang, Y. Ren, N. Liu, and J. Lin, 'Effect of cooling hole configurations on combustion and heat transfer in an aero-engine combustor', *Appl Therm Eng*, vol. 182, p. 115664, Jan. 2021, doi: 10.1016/j.applthermaleng.2020.115664.

[11] R. S. Bunker, 'Evolution of Turbine Cooling', in *Volume 1: Aircraft Engine; Fans and Blowers; Marine; Honors and Awards*, American Society of Mechanical Engineers, Jun. 2017. doi: 10.1115/GT2017-63205.

[12] P. H. Snyder and R.-R. North, 'Seal Technology Development for Advanced Component for Airbreathing Engines', 2008. [Online]. Available: http://www.sti.nasa.gov

[13] J. Ji, D. Huang, B. Sun, S. Peng, and C. Pan, 'Research on Active Control Strategy of Gas Turbine Secondary Air System in Different Ambient Temperature Conditions', in *Volume 5B: Heat Transfer*, American Society of Mechanical Engineers, Jun. 2017. doi: 10.1115/GT2017-63001.

[14] S. C. Pang, M. A. Kalam, H. H. Masjuki, and M. A. Hazrat, 'A review on air flow and coolant flow circuit in vehicles' cooling system', *Int J Heat Mass Transf*, vol. 55, no. 23–24, pp. 6295–6306, Nov. 2012, doi: 10.1016/j.ijheatmasstransfer.2012.07.002.

[15] plc. Rolls-Royce, 'The Jet Engine', 1996.

[16] T. S. Chowdhury, F. T. Mohsin, M. M. Tonni, M. N. H. Mita, and M. M. Ehsan, 'A critical review on gas turbine cooling performance and failure analysis of turbine blades', *International Journal of Thermofluids*, vol. 18, p. 100329, May 2023, doi: 10.1016/j.ijft.2023.100329.

[17] Waseem. Siddique, *Design of internal cooling passages investigation of thermal performance of serpentine passages*. Industrial Engineering and Management, Royal Institute of Technology, 2011.

[18] 'Gas Turbine Engineering Handbook Third Edition'.

[19] Logan E., *Handbook of Turbo Machinery*, 2nd ed. New York: CRC Press, 2003.

[20] Han JC, FrancisDutta S, and Ekkad S, *Gas turbine heat transfer and cooling technology, 1st edn.*, 1st ed. New yourk: Taylor & Francis, 2001.

[21] F. G. Rubensdörffer, 'Numerical and Experimental Investigations of Design Parameters Defining Gas Turbine Nozzle Guide Vane Endwall Heat Transfer', 2006.

[22] H. Cohen and F. J. Bayley, 'Heat-Transfer Problems of Liquid-cooled Gas-turbine Blades', *Proceedings of the Institution of Mechanical Engineers*, vol. 169, no. 1, pp. 1063–1080, Jun. 1955, doi: 10.1243/PIME_PROC_1955_169_106_02.

[23] D. G. Stratton, R. E. Stringer, and S. R. G. Taylor, 'Engine Cooling System Design and Development', *Proceedings of the Institution of Mechanical Engineers: Automobile Division*, vol. 180, no. 1, pp. 221–235, Jan. 1965, doi: 10.1243/PIME_AUTO_1965_180_023_02.

[24] M. G. Dunn, 'Convective Heat Transfer and Aerodynamics in Axial Flow Turbines', in *Volume 4: Manufacturing Materials and Metallurgy; Ceramics; Structures and Dynamics; Controls, Diagnostics and Instrumentation; Education; IGTI Scholar Award*, American Society of Mechanical Engineers, Jun. 2001. doi: 10.1115/2001-GT-0506.

[25] M. Huh and J.-C. Han, 'RECENT STUDIES IN TURBINE BLADE INTERNAL COOLING', in *Proceedings of International Symposium on Heat Transfer in Gas Turbine Systems*, New York: Begellhouse, 2009, pp. 1–20. doi: 10.1615/ICHMT.2009.HeatTransfGasTurbSyst.460.

[26] J. Kru¨ckels, T. Arzel, T. R. Kingston, and M. Schnieder, 'Turbine Blade Thermal Design Process Enhancements for Increased Firing Temperatures and Reduced Coolant Flow', in *Volume 4: Turbo Expo 2007, Parts A and B*, ASMEDC, Jan. 2007, pp. 445–455. doi: 10.1115/GT2007-27457.

[27] P. Ireland and G. Dailey, 'Aerothermal performance of internal cooling systems in turbomachines.', *In Internal Cooling In Turbomachinery (von Karman Institute, Belgium, May 2010)*, vol. 2010–05, no. 2010, pp. 8–12, May 2010.

[28] J.-C. Han and A. P. Rallabandi, 'TURBINE BLADE FILM COOLING USING PSP TECHNIQUE', *Frontiers in Heat and Mass Transfer*, vol. 1, 2010.

[29] B. Sunden and G. Xie, 'Gas Turbine Blade Tip Heat Transfer and Cooling: A Literature Survey', *Heat Transfer Engineering*, vol. 31, no. 7, pp. 527–554, Jun. 2010, doi: 10.1080/01457630903425320.

[30] C. Sharma *et al.*, 'Comprehensive Review on Leading Edge Turbine Blade Cooling Technologies', *International Journal of Heat and Technology*, vol. 39, no. 2, pp. 403–416, Apr. 2021, doi: 10.18280/ijht.390209.

[31] T. J. Martin and G. S. Dulikravich, 'Analysis and Multidisciplinary Optimization of Internal Coolant Networks in Turbine Blades', *J Propuls Power*, vol. 18, no. 4, pp. 896–906, Jul. 2002, doi: 10.2514/2.6015.

[32] L. M., S. M. Shaahid, and A. A., ‘Jet Impingement Cooling in Gas Turbines for Improving Thermal Efficiency and Power Density’, in *Advances in Gas Turbine Technology*, InTech, 2011. doi: 10.5772/22020.

[33] R. S. Bunker, ‘GAS TURBINE COOLING: MOVING FROM MACRO TO MICRO COOLING’, 2013. [Online]. Available: https://proceedings.asmedigitalcollection.asme.org

[34] M. K. Chyu Leighton Orr Chair Professor, ‘Recent Advances in Turbine Heat Transfer: With a View of Transition to Coal-Gas Based Systems’, 2010. [Online]. Available: http://proceedings.asmedigitalcollection.asme.org/pdfaccess.ashx?url=/data/conferences/ihtc14/72334/

[35] S. G. Kandlikar *et al.*, ‘Heat Transfer in Microchannels—2012 Status and Research Needs’, *J Heat Transfer*, vol. 135, no. 9, Sep. 2013, doi: 10.1115/1.4024354.

[36] J. C. Williams and E. A. Starke, ‘Progress in structural materials for aerospace systems11The Golden Jubilee Issue—Selected topics in Materials Science and Engineering: Past, Present and Future, edited by S. Suresh.’, *Acta Mater*, vol. 51, no. 19, pp. 5775–5799, Nov. 2003, doi: 10.1016/j.actamat.2003.08.023.

[37] T. Verstraete, S. Amaral, R. van den Braembussche, and T. Arts, ‘Design and Optimization of the Internal Cooling Channels of a High Pressure Turbine Blade—Part II: Optimization’, *J Turbomach*, vol. 132, no. 2, Apr. 2010, doi: 10.1115/1.3104615.

[38] D. Bohn, J. Ren, and K. Kusterer, ‘Conjugate Heat Transfer Analysis for Film Cooling Configurations With Different Hole Geometries’, in *Volume 5: Turbo Expo 2003, Parts A and B*, ASMEDC, Jan. 2003, pp. 247–256. doi: 10.1115/GT2003-38369.

[39] M. K. Sung and I. Mudawar, ‘Experimental and numerical investigation of single-phase heat transfer using a hybrid jet-impingement/micro-channel cooling scheme’, *Int J Heat Mass Transf*, vol. 49, no. 3–4, pp. 682–694, Feb. 2006, doi: 10.1016/j.ijheatmasstransfer.2005.08.021.

[40] G. Nowak and I. Nowak, ‘Shape design of internal cooling passages within a turbine blade’, *Engineering Optimization*, vol. 44, no. 4, pp. 449–466, Apr. 2012, doi: 10.1080/0305215X.2011.580742.

[41] G. Nowak and W. Wróblewski, ‘Optimization of blade cooling system with use of conjugate heat transfer approach’, *International Journal of Thermal Sciences*, vol. 50, no. 9, pp. 1770–1781, Sep. 2011, doi: 10.1016/j.ijthermalsci.2011.04.001.

[42] G. Nowak, W. Wróblewski, and I. Nowak, ‘Convective cooling optimization of a blade for a supercritical steam turbine’, *Int J Heat Mass Transf*, vol. 55, no. 17–18, pp. 4511–4520, Aug. 2012, doi: 10.1016/j.ijheatmasstransfer.2012.03.072.

[43] G. Nowak and W. Wro´blewski, ‘Thermo Mechanical Optimization of Cooled Turbine Vane’, in *Volume 4: Turbo Expo 2007, Parts A and B*, ASMEDC, Jan. 2007, pp. 931–938. doi: 10.1115/GT2007-28196.

[44] S. D. Mueller and J. H. Walther, ‘Evolution strategies for film cooling optimization’, *AIAA Journal*, vol. 39, pp. 537–539, Jan. 2001, doi: 10.2514/3.14766.

[45] B. H. Dennis, I. N. Egorov, G. S. Dulikravich, and S. Yoshimura, 'Optimization of a Large Number of Coolant Passages Located Close to the Surface of a Turbine Blade', in *Volume 5: Turbo Expo 2003, Parts A and B*, ASMEDC, Jan. 2003, pp. 13–19. doi: 10.1115/GT2003-38051.

[46] R. S. Bunker, 'Gas Turbine Heat Transfer: Ten Remaining Hot Gas Path Challenges', *J Turbomach*, vol. 129, no. 2, pp. 193–201, Apr. 2007, doi: 10.1115/1.2464142.

[47] J. Wang, B. Sundén, M. Zeng, and Q. Wang, 'Film cooling effects on the tip flow characteristics of a gas turbine blade', *Propulsion and Power Research*, vol. 4, no. 1, pp. 9–22, Mar. 2015, doi: 10.1016/j.jppr.2015.02.003.

[48] L. Wang, S. Wang, F. Wen, X. Zhou, and Z. Wang, 'Heat transfer and flow characteristics of U-shaped cooling channels with novel wavy ribs under stationary and rotating conditions', *Int J Heat Mass Transf*, vol. 126, pp. 312–333, Nov. 2018, doi: 10.1016/j.ijheatmasstransfer.2018.05.123.

[49] H. Ma, S. Shen, M. Yu, Z. Yang, M. Fei, and H. Zhou, 'Multi-population techniques in nature inspired optimization algorithms: A comprehensive survey', *Swarm Evol Comput*, vol. 44, pp. 365–387, Feb. 2019, doi: 10.1016/j.swevo.2018.04.011.

[50] M. Kadivar, D. Tormey, and G. McGranaghan, 'A comparison of RANS models used for CFD prediction of turbulent flow and heat transfer in rough and smooth channels', *International Journal of Thermofluids*, vol. 20, p. 100399, Nov. 2023, doi: 10.1016/j.ijft.2023.100399.

[51] _ L D Hylton and R. E. York, 'Analytical andExperimental Evaluation oftheHeat Transfer Distribution Over theSurfaces ofTurbine Vanes', 1983. Accessed: May 01, 1983. [Online]. Available: Analytical andExperimental Evaluation oftheHeat Transfer Distribution Over theSurfaces ofTurbine Vanes Hylton _, York R

[52] K. K. Tseng and L. Wang, 'Structural damage identification for thin plates using smart piezoelectric transducers', *Comput Methods Appl Mech Eng*, vol. 194, no. 27–29, 2005, doi: 10.1016/j.cma.2004.08.007.

[53] V. S. Sharma, M. Dogra, and N. M. Suri, 'Cooling techniques for improved productivity in turning', *Int J Mach Tools Manuf*, vol. 49, no. 6, pp. 435–453, May 2009, doi: 10.1016/j.ijmachtools.2008.12.010.

[54] P. Singh, A. Sarja, and S. V. Ekkad, 'Experimental and Numerical Study of Chord-Wise Eight-Passage Serpentine Cooling Design for Eliminating the Coriolis Force Adverse Effect on Heat Transfer', *J Therm Sci Eng Appl*, vol. 13, no. 1, Feb. 2021, doi: 10.1115/1.4047655.

[55] M. Obata, J. Yamaga, and H. Taniguchi, 'Heat transfer characteristics of a return-flow steam-cooled gas turbine blade', *Exp Therm Fluid Sci*, vol. 2, no. 3, pp. 323–332, Jul. 1989, doi: 10.1016/0894-1777(89)90021-6.

[56] E. E. Halila, D. T. Lenahan, and T. T. Thomas, 'High pressure turbine test hardware detailed design report ', Cleveland, Ohio, 1982.

[57] U. Uysal, P.-W. Li, M. K. Chyu, and F. J. Cunha, 'Heat Transfer on Internal Surfaces of a Duct Subjected to Impingement of a Jet Array with Varying Jet Hole-Size and Spacing', *J Turbomach*, vol. 128, no. 1, pp. 158–165, Jan. 2006, doi: 10.1115/1.2101859.

[58] D. E. Metzger, L. W. Florschuetz, D. I. Takeuchi, R. D. Behee, and R. A. Berry, 'Heat Transfer Characteristics for Inline and Staggered Arrays of Circular Jets with Crossflow of Spent Air', *J Heat Transfer*, vol. 101, no. 3, pp. 526–531, Aug. 1979, doi: 10.1115/1.3451022.

[59] D. M. Kercher and W. Tabakoff, 'Heat Transfer by a Square Array of Round Air Jets Impinging Perpendicular to a Flat Surface Including the Effect of Spent Air', *Journal of Engineering for Power*, vol. 92, no. 1, pp. 73–82, Jan. 1970, doi: 10.1115/1.3445306.

[60] L. W. Florschuetz and C. C. Su, 'Effects of Crossflow Temperature on Heat Transfer Within an Array of Impinging Jets', *J Heat Transfer*, vol. 109, no. 1, pp. 74–82, Feb. 1987, doi: 10.1115/1.3248072.

[61] L. W. Florschuetz, R. A. Berry, and D. E. Metzger, 'Periodic Streamwise Variations of Heat Transfer Coefficients for Inline and Staggered Arrays of Circular Jets with Crossflow of Spent Air', *J Heat Transfer*, vol. 102, no. 1, pp. 132–137, Feb. 1980, doi: 10.1115/1.3244224.

[62] W. W. Choi and S. M. Kim, 'Effect of effusion hole arrangement on jet array impingement heat transfer', *Int J Heat Mass Transf*, vol. 192, Aug. 2022, doi: 10.1016/j.ijheatmasstransfer.2022.122900.

[63] A. Amerini, S. Paccati, and A. Andreini, 'Computational Optimization of a Loosely-Coupled Strategy for Scale-Resolving CHT CFD Simulation of Gas Turbine Combustors', *Energies (Basel)*, vol. 16, no. 4, p. 1664, Feb. 2023, doi: 10.3390/en16041664.

[64] J. Y. Murthy and S. R. Mathur, 'Computational Heat Transfer in Complex Systems: A Review of Needs and Opportunities', *J Heat Transfer*, vol. 134, no. 3, Mar. 2012, doi: 10.1115/1.4005153.

[65] K. Wang, H. Li, and J. Zhu, 'Experimental study of heat transfer characteristic on jet impingement cooling with film extraction flow', *Appl Therm Eng*, vol. 70, no. 1, pp. 620–629, Sep. 2014, doi: 10.1016/j.applthermaleng.2014.05.077.

[66] C. R. Kini, S. S. Yalamarty, R. M. Mendonca, N. Yagnesh Sharma, and B. Satish Shenoy, 'CHT Analysis of Trailing Edge Region Cooling In HP Stage Turbine Blade', *Indian J Sci Technol*, vol. 9, no. 6, Feb. 2016, doi: 10.17485/ijst/2016/v9i6/76607.

[67] B. Facchini, L. Innocenti, and L. Tarchi, 'Pedestal and Endwall Contribution in Heat Transfer in Thin Wedge Shaped Trailing Edge', in *Volume 3: Turbo Expo 2004*, ASMEDC, Jan. 2004, pp. 101–111. doi: 10.1115/GT2004-53152.

[68] J. Luo and E. H. Razinsky, 'Conjugate Heat Transfer Analysis of a Cooled Turbine Vane Using the V2F Turbulence Model', *J Turbomach*, vol. 129, no. 4, pp. 773–781, Oct. 2007, doi: 10.1115/1.2720483.

[69] W. D. York and J. H. Leylek, 'Three-Dimensional Conjugate Heat Transfer Simulation of an Internally-Cooled Gas Turbine Vane', in *Volume 5: Turbo Expo 2003, Parts A and B*, ASMEDC, Jan. 2003, pp. 351–360. doi: 10.1115/GT2003-38551.

[70] V. Nirmalan and L. D. Hylton, 'An Experimental Study of Turbine Vane Heat Transfer With Leading Edge and Downstream Film Cooling', in *Volume 4: Heat Transfer; Electric Power; Industrial and Cogeneration*, American Society of Mechanical Engineers, Jun. 1989. doi: 10.1115/89-GT-69.

[71] F. Coletti, M. Scialanga, and T. Arts, ‘Experimental Investigation of Conjugate Heat Transfer in a Rib-Roughened Trailing Edge Channel With Crossing Jets’, *J Turbomach*, vol. 134, no. 4, Jul. 2012, doi: 10.1115/1.4003727.

[72] F. Coletti, M. Scialanga, and T. Arts, ‘Experimental Investigation of Conjugate Heat Transfer in a Rib-Roughened Trailing Edge Channel With Crossing Jets’, *J Turbomach*, vol. 134, no. 4, Jul. 2012, doi: 10.1115/1.4003727.

[73] T. Takahashi, K. Watanabe, and T. Takahashi, ‘Thermal Conjugate Analysis of a First Stage Blade in a Gas Turbine’, in *Volume 3: Heat Transfer; Electric Power; Industrial and Cogeneration*, American Society of Mechanical Engineers, May 2000. doi: 10.1115/2000-GT-0251.

[74] T. Takahashi, K. Watanabe, and T. Sakai, ‘Conjugate Heat Transfer Analysis of a Rotor Blade With Rib-Roughened Internal Cooling Passages’, in *Volume 3: Turbo Expo 2005, Parts A and B*, ASMEDC, Jan. 2005, pp. 275–284. doi: 10.1115/GT2005-68227.

[75] A. A. A. E. Elmenshawy and I. Alomar, ‘Statistics and Investigation of CF6 Jet Engines Hot Section Failures’, 2022, pp. 88–98. doi: 10.1007/978-3-030-96196-1_9.

[76] E. Turgut, T. H. Karakoc, A. Hepbasli, and E. T. Turgut, ‘Exergy Analysis of a Turbofan Engine: CF6-80’, 2007. [Online]. Available: https://www.researchgate.net/publication/228422319

[77] W. J. G. Bräunling, *Flugzeugtriebwerke*. Berlin, Heidelberg: Springer Berlin Heidelberg, 2004. doi: 10.1007/978-3-662-07268-4.

[78] M. G. Dunn, C. Padova, J. E. Moller, and R. M. Adams, ‘Performance Deterioration of a Turbofan and a Turbojet Engine Upon Exposure to a Dust Environment’, *J Eng Gas Turbine Power*, vol. 109, no. 3, pp. 336–343, Jul. 1987, doi: 10.1115/1.3240045.

[79] S. Ackert, ‘Engine Maintenance Concepts for Financiers Elements of Turbofan Shop Maintenance Costs’, 2011. Accessed: Sep. 01, 2011. [Online]. Available: http://www.aircraftmonitor.com/uploads/1/5/9/9/15993320/engine_mx_concepts_for_financiers__v2.pdf

[80] ‘GE, 2021. CF6-80C2 Boeing Engine Manual. GEK92451-Rev 92 as of 15.05.2021.’.

[81] E. V Zaretsky, J. S. Litt, R. C. Hendricks, and S. M. Soditus, ‘Determination of Turbine Blade Life from Engine Field Data’. [Online]. Available: https://ntrs.nasa.gov/search.jsp?R=20120007098

[82] L. Andrei, A. Andreini, L. Bonanni, and B. Facchini, ‘Heat transfer in internal channel of a blade: Effects of rotation in a trailing edge cooling system’, *Journal of Thermal Science*, vol. 21, no. 3, pp. 236–249, Jun. 2012, doi: 10.1007/s11630-012-0541-6.

[83] Y. A. Nozhnitsky, ‘The Problem of Ensuring Reliability of Gas Turbine Engines’, *IOP Conf Ser Mater Sci Eng*, vol. 302, p. 012082, Jan. 2018, doi: 10.1088/1757-899X/302/1/012082.

[84] ‘Boeing. B747-400 Aircraft Maintenance Manual, Rev 101 as of 15 of March 2021. Doc. N# D633U101-66’.

[85] A. Strawbridge, H. E. Evans, and C. B. Ponton, ‘Spallation of oxide scales from NiCrAlY overlay coatings’, *Materials Science Forum*, vol. 251–254, no. pt1, pp. 365–372, 1997, [Online]. Available: http://inis.iaea.org/search/search.aspx?orig_q=RN:29024901

[86] A. A. A. E. Elmenshawy, I. Alomar, A. Arshad, and A. Medvedevs, ‘Computational Fluid Dynamics Analysis of Flow Characteristics and Heat Transfer Variabilities in Multiple Turbine Blade Cooling Channels’, *Transport and Telecommunication Journal*, vol. 25, no. 1, pp. 77–96, Feb. 2024, doi: 10.2478/ttj-2024-0008.

[87] T. Xu, D. Shi, D. Zhang, and Y. Xie, ‘Flow and Heat Transfer Characteristics of the Turbine Blade Variable Cross-Section Internal Cooling Channel with Turning Vane’, *Applied Sciences*, vol. 13, no. 3, p. 1446, Jan. 2023, doi: 10.3390/app13031446.

[88] V. N. Afanasyev, Ya. P. Chudnovsky, A. I. Leontiev, and P. S. Roganov, ‘Turbulent flow friction and heat transfer characteristics for spherical cavities on a flat plate’, *Exp Therm Fluid Sci*, vol. 7, no. 1, pp. 1–8, Jul. 1993, doi: 10.1016/0894-1777(93)90075-T.

[89] Minking Chyu, ‘O. Concavity enhanced heat transfer in an internal cooling passage’, in *In Proceedings of the ASME 1997 International Gas Turbine and Aeroengine Congress and Exhibition*, Jun. 1997. Accessed: Jun. 01, 1997. [Online]. Available: https://www.academia.edu/77268876/Concavity_Enhanced_Heat_Transfer_in_an_Internal_Cooling_Passage

[90] H. K. Moon, T. O’Connell, and B. Glezer, ‘Channel Height Effect on Heat Transfer and Friction in a Dimpled Passage’, *J Eng Gas Turbine Power*, vol. 122, no. 2, pp. 307–313, Apr. 2000, doi: 10.1115/1.483208.

[91] N. K. Burgess, M. M. Oliveira, and P. M. Ligrani, ‘Nusselt Number Behavior on Deep Dimpled Surfaces Within a Channel’, *J Heat Transfer*, vol. 125, no. 1, pp. 11–18, Feb. 2003, doi: 10.1115/1.1527904.

[92] Z. Shen, H. Qu, D. Zhang, and Y. Xie, ‘Effect of bleed hole on flow and heat transfer performance of U-shaped channel with dimple structure’, *Int J Heat Mass Transf*, vol. 66, pp. 10–22, Nov. 2013, doi: 10.1016/j.ijheatmasstransfer.2013.07.008.

[93] Y. Yamane, Y. Ichikawa, M. Yamamoto, and S. Honami, ‘Effect of Injection Parameters on Jet Array Impingement Heat Transfer’, *International Journal of Gas Turbine, Propulsion and Power Systems*, vol. 4, no. 1, pp. 27–34, 2012, doi: 10.38036/jgpp.4.1_27.

[94] A. Ramadhan Al-Obaidi and I. Chaer, ‘Study of the flow characteristics, pressure drop and augmentation of heat performance in a horizontal pipe with and without twisted tape inserts’, *Case Studies in Thermal Engineering*, vol. 25, Jun. 2021, doi: 10.1016/j.csite.2021.100964.

[95] C. Glynn, T. O’Donovan, and D. Murray, ‘Jet Impingement Cooling’, *Proceedings of the 9th UK National Heat Transfer Conference*, Jan. 2005.

[96] N. Mashoofi, S. Pourahmad, and S. M. Pesteei, ‘Study the effect of axially perforated twisted tapes on the thermal performance enhancement factor of a double tube heat exchanger’, *Case Studies in Thermal Engineering*, vol. 10, pp. 161–168, Sep. 2017, doi: 10.1016/j.csite.2017.06.001.

[97] Z. Guo, Y. Rao, Y. Li, and W. Wang, ‘Experimental and numerical investigation of turbulent flow heat transfer in a serpentine channel with multiple short ribbed passes and turning vanes’, *International Journal of Thermal Sciences*, vol. 165, p. 106931, Jul. 2021, doi: 10.1016/j.ijthermalsci.2021.106931.

[98] G. O. Brown, ‘The History of the Darcy-Weisbach Equation for Pipe Flow Resistance’, in *Environmental and Water Resources History*, Reston, VA: American Society of Civil Engineers, Oct. 2002, pp. 34–43. doi: 10.1061/40650(2003)4.

[99] S.-F. Yang, H.-W. Wu, J.-C. Han, L. Zhang, and H.-K. Moon, ‘Heat transfer in a smooth rotating multi-passage channel with hub turning vane and trailing-edge slot ejection’, *Int J Heat Mass Transf*, vol. 109, pp. 1–15, Jun. 2017, doi: 10.1016/j.ijheatmasstransfer.2017.01.059.

[100] A. A. A. E. Elmenshawy, I. Alomar, and A. Arshad, ‘Optimization Turbine Blade Cooling by Applying Jet Impingement Cooling Channels’, *Transport and Telecommunication Journal*, vol. 24, no. 3, pp. 320–337, Jun. 2023, doi: 10.2478/ttj-2023-0026.

[101] M. SAJBEN, J. KROUTIL, and C. CHEN, ‘A high-speed schlieren investigation of diffuser flows with dynamic distortion’, in *13th Propulsion Conference*, Reston, Virigina: American Institute of Aeronautics and Astronautics, Jul. 1977. doi: 10.2514/6.1977-875.

[102] N. Mashoofi, S. Pourahmad, and S. M. Pesteei, ‘Study the effect of axially perforated twisted tapes on the thermal performance enhancement factor of a double tube heat exchanger’, *Case Studies in Thermal Engineering*, vol. 10, pp. 161–168, Sep. 2017, doi: 10.1016/j.csite.2017.06.001.

[103] F. R. Menter, ‘Two-equation eddy-viscosity turbulence models for engineering applications’, *AIAA Journal*, vol. 32, no. 8, pp. 1598–1605, Aug. 1994, doi: 10.2514/3.12149.

[104] F. Menter, ‘Zonal Two Equation k-w Turbulence Models For Aerodynamic Flows’, in *23rd Fluid Dynamics, Plasmadynamics, and Lasers Conference*, Reston, Virigina: American Institute of Aeronautics and Astronautics, Jul. 1993. doi: 10.2514/6.1993-2906.

[105] A. J. Organ, ‘Counter-flow spiral heat exchanger – Spirex’, in *The Air Engine*, Elsevier, 2007, pp. 29–38. doi: 10.1533/9781845693602.1.29.

[106] C. D. Rossman, ‘Analysis of a Coupled Micro-and Triple-Impingement Cooling Analysis of a Coupled Micro-and Triple-Impingement Cooling Configuration in the C3X Vane Configuration in the C3X Vane’. [Online]. Available: https://commons.erau.edu/edt

Appendix 1

Nusselt number with Renolds number calculation MATLAB code:

Matlab code

```
% Define the specific Reynolds numbers
Re = [10000, 20000, 30000, 40000, 50000, 60000];

% Prandtl number (fixed)
Pr = 0.71;

% Constants
Dc = 0.0063; % Convert 6.3 mm to meters
lambda = 0.026;

% Define a vector of Tw values
Tw_values = [573, 625, 550];

% Tf (fixed)
Tf = 298;

% Initialize an empty matrix to store (Nua/Nu0) values for each Tw
Nua_over_Nu0_matrix = zeros(length(Tw_values), length(Re));

% Loop through each Tw value
for i = 1:length(Tw_values)
    Tw = Tw_values(i);

    % Set a fixed value for q
    q = 5000;

    % Calculate Nua for each Reynolds number
    Nua = 0.023 * (Pr^0.5) * (Re.^0.8);

    % Calculate Nu for each Reynolds number
    Nu = (q * Dc) ./ ((Tw - Tf) * lambda);
```

```
    % Calculate (Nua/Nu0) for each Reynolds number
    Nua_over_Nu0 = Nua ./ Nu;

    % Store the results in the matrix
    Nua_over_Nu0_matrix(i, :) = Nua_over_Nu0;
end

% Plot the graph for each Tw value
figure;
hold on;
for i = 1:length(Tw_values)
    plot(Re, Nua_over_Nu0_matrix(i, :), '-o', 'LineWidth', 2);
end

xlabel('Reynolds Number (Re)');
ylabel('Nua/Nu0');
title('Nua/Nu0 vs. Reynolds Number');
legend('Tw = 573', 'Tw = 625', 'Tw = 550');
grid on;

% Customize the plot further as needed
```

Appendix 2

Fraction factor with Renolds number calculation MATLAB code:

```
% Define the given parameters
Dc = 0.0063; % Convert 6.3 mm to meters
Delta_p_cases = [1733, 1650, 1467; 2000, 1800, 1600; 2200, 1950, 1800]; % Pa (Three
cases)
L_cases = [0.09222, 0.0762, 0.0762; 0.082, 0.072, 0.062; 0.088, 0.078, 0.068]; %
Length in meters (Three cases)
rho = 1.225; % kg/m^3
mu = 1.849e-5; % Pa·s
Re = [10000, 20000, 30000, 40000, 50000, 60000];
```

```
% Initialize an empty matrix to store (f/f0) values for each case
f_over_f0_matrix = zeros(size(Delta_p_cases, 1), length(Re));

% Calculate f0 based on the first Reynolds number in the list (Re = 10000)
Re_0 = Re(1);
f0 = 0.507 * Re_0^(-0.3);

% Create a cell array to store line styles or colors for each case
line_styles = {'-o', '--s', '-^'};

% Create a figure for the combined plot
figure;

% Loop through each case of Delta_p and L
for case_index = 1:size(Delta_p_cases, 1)
    Delta_p = Delta_p_cases(case_index, :);
    L = L_cases(case_index, :);

    % Initialize an empty vector to store (f/f0) values for this case
    f_over_f0 = zeros(1, length(Re));

    % Loop through each Reynolds number
    for i = 1:min(length(Re), length(L))
        % Calculate Uin based on the Reynolds number
        Uin = (Re(i) * mu) / (rho * Dc);

        % Calculate f using the given formula
        f = (Delta_p(i) * Dc) / (2 * rho * L(i) * Uin^2);

        % Calculate (f/f0) for each Reynolds number
        f_over_f0(i) = f / f0;
    end

    % Store the results for this case in the matrix
    f_over_f0_matrix(case_index, :) = f_over_f0;
```

```
    % Plot (f/f0) against Reynolds number (Re) for this case with a specific line
style/color
    plot(Re, f_over_f0, line_styles{case_index}, 'LineWidth', 2, 'DisplayName',
['Case ', num2str(case_index)]);
    hold on;
end

xlabel('Reynolds Number (Re)');
ylabel('f/f0');
title('f/f0 vs. Reynolds Number (Multiple Cases)');
grid on;
legend('Location', 'Best'); % Display a legend


% Given parameters
Delta_p = [3874, 3656, 4025]; % in Pa
Dh = 0.52 / 100; % convert cm to m
L = 0.98 / 100; % convert cm to m
rho = 1.25; % in kg/m^3
mu = 0.0000173; % in kg/(m s)
Re_values = [10000, 20000, 30000, 40000, 50000];

% Initialize f_values matrix to store f for each Delta_p and Re combination
f_values = zeros(length(Delta_p), length(Re_values));

% Loop through each Delta_p
for j = 1:length(Delta_p)
    % Loop through Re_values to calculate f for each case
    for i = 1:length(Re_values)
        % Calculate U using Re
        U = (Re_values(i) * mu) / (rho * Dh);

        % Calculate f
        f_values(j, i) = Delta_p(j) * Dh / (2 * rho * L * U^2);
    end
end
```

```
% Create the plot
figure;
hold on;
for j = 1:length(Delta_p)
    plot(Re_values, f_values(j, :), '-o', 'DisplayName', ['\Delta p = ',
num2str(Delta_p(j)), ' Pa']);
end
xlabel('Re');
ylabel('f');
title('Graph between f and Re for Different \Delta p');
legend('show');
grid on;
hold off;



% Given data (all units are in SI)
delta_p = [1120, 1220, 1325, 1680, 1612, 560, 1325, 1696, 2239, 2798.3, 2795, 2967,
3136, 3136, 2239];
L_values = 15.34 * ones(1, 10); % 10 values of 15.34 mm in an array
L_values = [L_values, 15.54 * ones(1, 5)]; % Append 5 values of 15.54 mm to the array
L_values = L_values / 1000; % Convert mm to m for SI unit
Dh = 0.19 / 100; % Convert cm to m
rho = 1.25; % kg/m^3
mu = 0.0000173; % kg/(m s)

% Reynolds numbers
Re_values = 10000:1000:50000; % Starts at 10000, ends at 50000

% Initialize results
results = [];

% Perform calculations
for dp = delta_p
    for L = L_values
        for Re = Re_values
            U_in = (Re * mu) / (rho * Dh); % Calculate inlet velocity
```

```
            f = (dp * Dh) / (2 * rho * L * U_in^2); % Calculate friction factor
            results = [results; [Re, f, dp, L]]; % Store the results
        end
    end
end

% Convert to table for better readability
T = array2table(results, 'VariableNames', {'Re', 'f', 'delta_p', 'L'});

% Plotting
figure;
hold on;
unique_dp = unique(delta_p);
for i = 1:length(unique_dp)
    dp = unique_dp(i);
    subset = results(results(:, 3) == dp, :);
    plot(subset(:, 1), subset(:, 2), 'DisplayName', ['\Delta p = ', num2str(dp), '
Pa']);
end

xlabel('Reynolds Number');
ylabel('Friction Factor');
title('Friction Factor vs Reynolds Number');
legend('Location', 'best');
grid on;
hold off;
% Plotting the results
figure;
hold on;

colors = {'r','g','b','m','c'};

for i = 1:length(delta_p)
    dp = delta_p(i);
    subset = results(results(:, 3) == dp, :);
    scatter(subset(:, 1), subset(:, 2), 'DisplayName', ['\Delta p = ', num2str(dp), '
Pa']);
```

```
end

xlabel('Reynolds Number (Re)');
ylabel('Friction Factor (f)');
title('Friction Factor vs. Reynolds Number for Various \Delta p');
legend('Location','best');
grid on;
hold off;

% For line plots
figure;
hold on;

for i = 1:length(delta_p)
    dp = delta_p(i);
    subset = results(results(:, 3) == dp, :);
    plot(subset(:, 1), subset(:, 2), 'DisplayName', ['\Delta p = ', num2str(dp), '
Pa']);
end

xlabel('Reynolds Number (Re)');
ylabel('Friction Factor (f)');
title('Friction Factor vs. Reynolds Number for Various \Delta p');
legend('Location','best');
grid on;
hold off;

% Given constants
delta_p_values = [4940, 3850, 2765, 1256]; % in Pa
L = 28e-3; % in m (converted from mm)
rho = 1.255; % in kg/m^3
mu = 0.0000173; % in kg/(m s)
Dh = 6.3e-3; % in m (converted from mm)

% Calculate the area A
A = Dh * 8e-3; % Convert 8mm to meters
```

```
% Pre-defined Re values
Re_values = [10000, 20000, 30000, 40000, 50000];

% Initialize empty array to store F_d (drag force) values for each delta_p
F_d_values_cases = zeros(length(delta_p_values), length(Re_values));

% Calculate F_d values for each delta_p and Re combination
for i = 1:length(delta_p_values)
    delta_p = delta_p_values(i);

    % Calculate drag force for each delta_p
    F_d_values = delta_p * A;

    % Store the calculated F_d values
    F_d_values_cases(i, :) = F_d_values;
end

% Plotting the graph
figure;
hold on;
for i = 1:length(delta_p_values)
    plot(Re_values, F_d_values_cases(i, :), 'o-', 'DisplayName', ['\Delta p = ',
num2str(delta_p_values(i)), ' Pa']);
end
xlabel('Re');
ylabel('F_d (Drag Force) [N]');
title('Graph between Drag Force and Re for different \Delta p');
legend('show');
grid on;
hold off;
```

……

```
% Given values
delta_p = [3874, 3656, 4025]; % in Pa
Dh = 0.0052; % in m
L = 0.0098; % in m
```

```
rho = 1.25; % in kg/m^3
mu = 0.0000173; % in kg/(m s)
Re_values = [10000, 20000, 30000, 40000, 50000];
A = 0.00005096; % Area in m^2

% Initialize vectors to store drag force
Fd_values = zeros(length(Re_values), length(delta_p));

% Loop through all cases
for i = 1:length(delta_p)
    for j = 1:length(Re_values)
        U = (Re_values(j) * mu) / (rho * Dh); % Calculate velocity
        f = (delta_p(i) * Dh) / (2 * rho * L * U^2); % Calculate friction factor
        Fd_values(j, i) = f * (rho * U^2 / 2) * A; % Calculate drag force
    end
end

% Plot
figure;
hold on;
for i = 1:length(delta_p)
    plot(Re_values, Fd_values(:, i), 'DisplayName', ['\Delta p = ',
num2str(delta_p(i)), ' Pa']);
end
xlabel('Reynolds Number');
ylabel('Drag Force (N)');
legend;
hold off;

……….

% Given data
delta_p =
[1120,1220,1325,1680,1612,560,1325,1696,2239,2798.3,2795,2967,3136,3136,2239];
L =
[15.34,15.34,15.34,15.34,15.34,15.54,15.54,15.54,15.54,15.54,15.34,15.34,15.34,15.34,
15.34]; % in mm
```

```
Dh = 0.19 / 100; % in m
rho = 1.255; % in kg/m^3
mu = 0.0000173; % in kg/(m s)
Re_values = 10000:10000:50000; % Dimensionless
A = (L / 1000) .* Dh; % converting both L and Dh to m for area in m^2

% Initialize the Fd matrix
Fd = zeros(length(delta_p), length(Re_values));

% Calculating the friction factor and drag force
for i = 1:length(delta_p)
    for j = 1:length(Re_values)
        f = (delta_p(i) * Dh) / (2 * rho * (L(i) / 1000) * Re_values(j)^2); %
converting L from mm to m for the formula
        Fd(i, j) = f * (delta_p(i) * A(i) / 2);
    end
end

% Plotting the graph
figure;
hold on;

for i = 1:length(delta_p)
    plot(Re_values, Fd(i, :), 'DisplayName', ['\Delta p = ', num2str(delta_p(i)), '
Pa']);
end

xlabel('Reynolds Number (Re)');
ylabel('Drag Force (F_d) [N]'); % Added unit
title('Drag Force vs. Reynolds Number for Various \Delta p');
legend('Location','best');
grid on;
hold off;
```

```
% Define the given parameters
Dc = 0.0063; % Convert 6.3 mm to meters
Delta_p_cases = [3733, 3650, 3867; 3000, 3800, 3600; 2900, 2950, 3800]; % Pa (Three
cases)
L_cases = [0.09222, 0.0762, 0.0762; 0.082, 0.072, 0.062; 0.088, 0.078, 0.068]; %
Length in meters (Three cases)
rho = 1.225; % kg/m^3
mu = 1.849e-5; % Pa·s
Re = [10000, 20000, 30000];

% Initialize an empty matrix to store (f/f0) values for each case
f_over_f0_matrix = zeros(size(Delta_p_cases, 1), length(Re));

% Calculate f0 based on the first Reynolds number in the list (Re = 10000)
f = 0.507 * Re(i)^(-0.3);

% Create a cell array to store line styles or colors for each case
line_styles = {'-o', '--s', '-^'};

% Create a figure for the combined plot
figure;

% Loop through each case of Delta_p and L
for case_index = 1:size(Delta_p_cases, 1)
    Delta_p = Delta_p_cases(case_index, :);
    L = L_cases(case_index, :);

    % Initialize an empty vector to store (f/f0) values for this case
    f_over_f0 = zeros(1, length(Re));

    % Loop through each Reynolds number
    for i = 1:min(length(Re), length(L))
        % Calculate Uin based on the Reynolds number
        Uin = (Re(i) * mu) / (rho * Dc);

        % Calculate f using the given formula
        f0 = (Delta_p(i) * Dc) / (2 * rho * L(i) * Uin^2);
```

```
        % Calculate (f/f0) for each Reynolds number
        f_over_f0(i) = f / f0;
    end

    % Store the results for this case in the matrix
    f_over_f0_matrix(case_index, :) = f_over_f0;

    % Plot (f/f0) against Reynolds number (Re) for this case with a specific line
style/color
    plot(Re, f_over_f0, line_styles{case_index}, 'LineWidth', 2, 'DisplayName',
['Case ', num2str(case_index)]);
    hold on;
end

xlabel('Reynolds Number (Re)');
ylabel('f/f0');
title('f/f0 vs. Reynolds Number (Multiple Cases)');
grid on;
legend('Location', 'Best'); % Display a legend

% Define the given parameters
Dc = 0.0063; % Convert 6.3 mm to meters
Delta_p_cases = [1733, 1650, 1467; 2000, 1800, 1600; 2200, 1950, 1800]; % Pa (Three
cases)
L_cases = [0.09222, 0.0762, 0.0762; 0.082, 0.072, 0.062; 0.088, 0.078, 0.068]; %
Length in meters (Three cases)
rho = 1.225; % kg/m^3
mu = 1.849e-5; % Pa·s
Re = [10000, 20000, 30000, 40000, 50000, 60000];

% Initialize empty matrices to store (f/f0) and (Nua/Nu0) values for each case
f_over_f0_matrix = zeros(size(Delta_p_cases, 1), length(Re));
Nua_over_Nu0_matrix = zeros(size(Delta_p_cases, 1), length(Re));

% Calculate f0 based on the first Reynolds number in the list (Re = 10000)
Re_0 = Re(1);
```

```
f0 = 0.507 * Re_0^(-0.3);

% Create a cell array to store line styles or colors for each case
line_styles = {'-o', '--s', '-^'};

% Create a figure for the combined plot
figure;

% Loop through each case of Delta_p and L
for case_index = 1:size(Delta_p_cases, 1)
    Delta_p = Delta_p_cases(case_index, :);
    L = L_cases(case_index, :);

    % Initialize empty vectors to store (f/f0) and (Nua/Nu0) values for this case
    f_over_f0 = zeros(1, length(Re));
    Nua_over_Nu0 = zeros(1, length(Re));

    % Loop through each Reynolds number
    for i = 1:min(length(Re), length(L))
        % Calculate Uin based on the Reynolds number
        Uin = (Re(i) * mu) / (rho * Dc);

        % Calculate f using the given formula
        f = (Delta_p(i) * Dc) / (2 * rho * L(i) * Uin^2);

        % Calculate (f/f0) for each Reynolds number
        f_over_f0(i) = f / f0;

        % Calculate Nua for each Reynolds number
        Nu0 = 0.023 * (Re(i)^0.8);

        % Calculate Nu for each Reynolds number
        Nua = (Uin * Dc) / (f * (1 / rho) * (1 / L(i)));

        % Calculate (Nua/Nu0) for each Reynolds number
        Nua_over_Nu0(i) = Nua / Nu0;
    end
```

```
    % Store the results for this case in the matrices
    f_over_f0_matrix(case_index, :) = f_over_f0;
    Nua_over_Nu0_matrix(case_index, :) = Nua_over_Nu0;

    % Calculate Tp for this case using the formula T_P=(N_(u_a )/N_0 )×(f/f_0 )^(-
1/3)
    Tp = Nua_over_Nu0 .* (f_over_f0.^(-1/3))/100;

    % Plot Tp against Reynolds number (Re) for this case with a specific line
style/color
    plot(Re, Tp, line_styles{case_index}, 'LineWidth', 2, 'DisplayName', ['Case ',
num2str(case_index)]);
    hold on;
end

xlabel('Reynolds Number (Re)');
ylabel('Tp');
title('Tp vs. Reynolds Number (Multiple Cases)');
grid on;
legend('Location', 'Best'); % Display a legend

……….

% Define the given parameters
Dc = 0.0063; % Convert 6.3 mm to meters
Delta_p_cases = [1733, 1650, 2467; 2000, 1800, 1600; 2200, 1950, 1800]; % Pa (Three
cases)
L_cases = [0.09222, 0.0762, 0.0762; 0.082, 0.072, 0.062; 0.088, 0.078, 0.068]; %
Length in meters (Three cases)
rho = 1.225; % kg/m^3
mu = 1.849e-5; % Pa·s
Re = [10000, 20000, 30000, 40000, 50000, 60000];
Tw_cases = [573, 625, 550]; % Wall temperatures in K (Three cases)
Tf = 298; % Inlet temperature in K
lambda = 0.02624; % Fluid thermal conductivity
q = 5000; % Heat transfer rate (constant for all cases)
```

```
% Initialize empty matrices to store (f/f0), (Nua/Nu0), and Tp values for each case
f_over_f0_matrix = zeros(size(Delta_p_cases, 1), length(Re));
Nua_over_Nu0_matrix = zeros(size(Delta_p_cases, 1), length(Re));
Tp_matrix = zeros(size(Delta_p_cases, 1), length(Re));

% Calculate f0 based on the first Reynolds number in the list (Re = 10000)
Re_0 = Re(1);
f0 = 0.507 * Re_0^(-0.3);

% Create a cell array to store line styles or colors for each case
line_styles = {'-o', '--s', '-^'};

% Create a figure for the combined plot
figure;

% Loop through each case of Delta_p and L
for case_index = 1:size(Delta_p_cases, 1)
    Delta_p = Delta_p_cases(case_index, :);
    L = L_cases(case_index, :);
    Tw = Tw_cases(case_index);

    % Initialize empty vectors to store (f/f0), (Nua/Nu0), and Tp values for this
case
    f_over_f0 = zeros(1, length(Re));
    Nua_over_Nu0 = zeros(1, length(Re));
    Tp = zeros(1, length(Re));

    % Loop through each Reynolds number
    for i = 1:min(length(Re), length(L))
        % Calculate Uin based on the Reynolds number
        Uin = (Re(i) * mu) / (rho * Dc);

        % Calculate f using the given formula
        f = (Delta_p(i) * Dc) / (2 * rho * L(i) * Uin^2);

        % Calculate (f/f0) for each Reynolds number
```

```
        f_over_f0(i) = f / f0;

        % Calculate Nua for each Reynolds number
        Nua = 0.023 * (Re(i)^0.8);

        % Calculate Nu using the given equation
        Nu = (q * Dc) / ((Tw - Tf) * lambda);

        % Calculate (Nua/Nu0) for each Reynolds number
        Nua_over_Nu0(i) = Nua / Nu;

        % Calculate Tp for this case using the formula T_P=(N_(u_a )/N_0 )×(f/f_0
)^(-1/3)
        Tp(i) = Nua_over_Nu0(i) * (f_over_f0(i)^(-1/3));
    end

    % Store the results for this case in the matrices
    f_over_f0_matrix(case_index, :) = f_over_f0;
    Nua_over_Nu0_matrix(case_index, :) = Nua_over_Nu0;
    Tp_matrix(case_index, :) = Tp;

    % Plot Tp against Reynolds number (Re) for this case with a specific line
style/color
    plot(Re, Tp, line_styles{case_index}, 'LineWidth', 2, 'DisplayName', ['Case ',
num2str(case_index)]);
    hold on;
end

xlabel('Reynolds Number (Re)');
ylabel('Tp');
title('Tp vs. Reynolds Number (Multiple Cases)');
grid on;
legend('Location', 'Best'); % Display a legend

……

% Define the given parameters
```

```
Dc = 0.0063; % Convert 6.3 mm to meters
Delta_p_cases = [3733, 3650, 3867; 3000, 3800, 3600; 2900, 2950, 3800]; % Pa (Three
cases)
L_cases = [0.09222, 0.0762, 0.0762; 0.082, 0.072, 0.062; 0.088, 0.078, 0.068]; %
Length in meters (Three cases)
rho = 1.225; % kg/m^3
mu = 1.849e-5; % Pa·s
Re = [10000, 20000, 30000, 40000, 50000, 60000];
Tw = 573; % Wall temperature in K
Tf = 298; % Inlet temperature in K
lambda = 0.02624; % Fluid thermal conductivity

% Initialize empty matrices to store (f/f0), (Nua/Nu0), and Tp values for each case
f_over_f0_matrix = zeros(size(Delta_p_cases, 1), length(Re));
Nua_over_Nu0_matrix = zeros(size(Delta_p_cases, 1), length(Re));
Tp_matrix = zeros(size(Delta_p_cases, 1), length(Re));

% Calculate f0 based on the first Reynolds number in the list (Re = 10000)
Re_0 = Re(1);
f0 = 0.507 * Re_0^(-0.3);

% Create a cell array to store line styles or colors for each case
line_styles = {'-o', '--s', '-^'};

% Create a figure for the combined plot
figure;

% Loop through each case of Delta_p and L
for case_index = 1:size(Delta_p_cases, 1)
    Delta_p = Delta_p_cases(case_index, :);
    L = L_cases(case_index, :);

    % Initialize empty vectors to store (f/f0), (Nua/Nu0), and Tp values for this
case
    f_over_f0 = zeros(1, length(Re));
    Nua_over_Nu0 = zeros(1, length(Re));
    Tp = zeros(1, length(Re));
```

```
    % Loop through each Reynolds number
    for i = 1:min(length(Re), length(L))
        % Calculate Uin based on the Reynolds number
        Uin = (Re(i) * mu) / (rho * Dc);

        % Calculate f using the given formula
        f = (Delta_p(i) * Dc) / (2 * rho * L(i) * Uin^2);

        % Calculate (f/f0) for each Reynolds number
        f_over_f0(i) = f / f0;

        % Calculate Nua for each Reynolds number
        Nu0 = 0.023 * (Re(i)^0.8);

        % Calculate Nu using the given equation
        Nua = (q * Dc) / ((Tw - Tf) * lambda);

        % Calculate (Nua/Nu0) for each Reynolds number
        Nua_over_Nu0(i) = Nua / Nu;

        % Calculate Tp for this case using the formula T_P=(N_(u_a )/N_0 )×(f/f_0
)^(-1/3)
        Tp(i) = Nua_over_Nu0(i) * (f_over_f0(i)^(-1/3));
    end

    % Store the results for this case in the matrices
    f_over_f0_matrix(case_index, :) = f_over_f0;
    Nua_over_Nu0_matrix(case_index, :) = Nua_over_Nu0;
    Tp_matrix(case_index, :) = Tp;

    % Plot Tp against Reynolds number (Re) for this case with a specific line
style/color
    plot(Re, Tp, line_styles{case_index}, 'LineWidth', 2, 'DisplayName', ['Case ',
num2str(case_index)]);
    hold on;
end
```

```
xlabel('Reynolds Number (Re)');
ylabel('Tp');
title('Tp vs. Reynolds Number (Multiple Cases)');
grid on;
legend('Location', 'Best'); % Display a legend

% Define the specific Reynolds numbers
Re = [10000, 20000, 30000, 40000, 50000, 60000];

% Prandtl number (fixed)
Pr = 0.71;

% Constants
Dc = 0.0063; % Convert 6.3 mm to meters
lambda = 0.026;

% Define a vector of Tw values
Tw_values = [573, 625, 550];

% Tf (fixed)
Tf = 298;

% Initialize an empty matrix to store (Nua/Nu0) values for each Tw
Nua_over_Nu0_matrix = zeros(length(Tw_values), length(Re));

% Loop through each Tw value
for i = 1:length(Tw_values)
    Tw = Tw_values(i);

    % Set a fixed value for q
    q = 5000;

    % Calculate Nua for each Reynolds number
    Nua = 0.023 * (Pr^0.5) * (Re.^0.8);

    % Calculate Nu for each Reynolds number
```

```
    Nu = (q * Dc) ./ ((Tw - Tf) * lambda);

    % Calculate (Nua/Nu0) for each Reynolds number
    Nua_over_Nu0 = Nua ./ Nu;

    % Store the results in the matrix
    Nua_over_Nu0_matrix(i, :) = Nua_over_Nu0;
end

% Plot the graph for each Tw value
figure;
hold on;
for i = 1:length(Tw_values)
    plot(Re, Nua_over_Nu0_matrix(i, :), '-o', 'LineWidth', 2);
end

xlabel('Reynolds Number (Re)');
ylabel('Nua/Nu0');
title('Nua/Nu0 vs. Reynolds Number');
legend('Tw = 573', 'Tw = 625', 'Tw = 550');
grid on;

% Customize the plot further as needed
```

……

Adham Ahmed Awad Elsayed Elmenshawy was born in 1986 in Belqas, Dakahlia, Egypt. He obtained his Bachelor's degree in Aviation Engineering from the Institute of Aviation Engineering and Technology, Egypt, in 2008 and a Master's degree in Aviation Transport from Riga Technical University in 2017. Since 2018, he has been a research assistant at Riga Technical University. He is currently a guest lecturer at the Transport and Telecommunication Institute, as well as an instructor at the APAC EASA Training Centre. He participated in exchange staff teaching within the Erasmus+ framework at Kaunas University of Applied Engineering Sciences (Lithuania) and has been involved in two European projects. He is a certified EASA Part 66/147 instructor. His research interests include fluid dynamics, aircraft engines, aircraft structures, robotics, material engineering, and UAVs.